Technische Universität München
TUM Campus Straubing für Biotechnologie und Nachhaltigkeit

Dehydration Processes in the Production of Poly(oxymethylene) Dimethyl Ethers and Their Integration in a Continuous Mini-Plant

Alvaro Luis Ferre

Vollständiger Abdruck der vom TUM Campus Straubing für Biotechnologie und Nachhaltigkeit der Technischen Universität München zur Erlangung eines

Doktors der Ingenieurwissenschaften (Dr.-Ing.)

genehmigten Dissertation.

Vorsitz: Prof. Dr. Bastian Blombach

Prüfende der Dissertation:

1. Prof. Dr.-Ing. Jakob Burger
2. Prof. Dr.-Ing. Hans Hasse
3. Prof. Dr.-Ing. Matthias Gaderer

Die Dissertation wurde am 17.05.2024 bei der Technischen Universität München eingereicht und durch den TUM Campus Straubing für Biotechnologie und Nachhaltigkeit am 26.07.2024 angenommen.

Danksagung

Die vorliegende Arbeit entstand während meiner Tätigkeit als wissenschaftlicher Mitarbeiter der Professur für Chemische und Thermische Verfahenstechnik am Campus Straubing für Biotechnologie und Nachhaltigkeit der Technischen Universität München.

An dieser Stelle möchte ich allen meinen herzlichen Dank aussprechen, die mich auf dem Weg zu dieser Dissertation unterstützt und begleitet haben.

Mein besonderer Dank gilt meinem Doktorvater, Prof. Dr.-Ing. Jakob Burger, für seine fachliche Betreuung, seine wertvollen Anregungen, seine persönliche Unterstützung, und sein stetiges Vertrauen in mich.

Ebenso möchte ich mich bei Prof. Dr.-Ing. Hans Hasse und Prof. Dr.-Ing. Matthias Gaderer für die Begutachtung meiner Arbeit bedanken. Mein Dank gilt auch Prof. Dr. Bastian Blombach für die Übernahme des Prüfungsvorsitzes.

Ein großer Dank geht auch an meine Kolleginnen und Kollegen, die mich in vielerlei Hinsicht unterstützt haben. Bei Birgit Aich-Bauer bedanke ich mich für die Hilfe bei organisatorischen Themen und die netten Gespräche. Bei Stefan Hartl bedanke ich mich für die tatkräftige Unterstützung im Technikum bei der OME-Anlage. Bei Christina Wolf bedanke ich mich für die unersetzliche Hilfe in Laborangelegenheiten. Bei Quirin Göttl bedanke ich mich für die stets angenehme Atmosphäre im Büro. Bei Johannes Voggenreiter bedanke ich mich für die fruchtbare Zusammenarbeit und die viele Diskussionen rund um die OME-Themen. Bei Natalie Rosen bedanke ich mich für die unzähligen Pan-Queso-Spiele und ihre wertvolle Unterstützung in den letzten Monaten. Allen anderen Kolleginnen und Kollegen danke ich für die durchweg positive Stimmung und die angenehme Zeit.

Mein Dank gilt auch den von mir betreuten Studierenden, deren engagierte Mitarbeit zum Erfolg dieser Arbeit beigetragen hat: Ulf Stegemeyer, Kevin Setiadarma, David Hristov, David Jocher, Mazin Chalb Cham, Thomas Blaim, Christian Mertins und Nina Zistler.

Nicht zuletzt gilt mein tiefster Dank meiner Familie, insbesondere meinen Eltern. Sie haben mich in all den Jahren unerschütterlich unterstützt, sei es durch ihre Ermutigung

aus der Ferne oder ihre ständige Bereitschaft, für mich da zu sein - auch über viele Kilometer hinweg. Muchas gracias por todo, los amo.

Zu guter Letzt möchte ich mich bei meinem Partner Thomas bedanken, der mir mit unendlicher Geduld, Verständnis und Liebe zur Seite stand. Du warst meine wichtigste Kraftquelle auf diesem Weg.

Rohr in Niederbayern, im September 2024
Alvaro Ferre

Abstract

Poly(oxymethylene) dimethyl ethers of chain lengths $n = 3$ to 5 ($OME_{3–5}$) are promising clean-burning synthetic diesel fuels. While conventional water-free production methods are well established, water-tolerant $OME_{3–5}$ production processes offer a compelling alternative yet to be realized at an industrial scale. These processes present the advantage of utilizing cheaper starting materials at the cost of a more complex downstreaming, particularly involving a challenging water separation step.

This work focuses on a recently developed water-tolerant $OME_{3–5}$ production process that consists of a reactor, a distillation sequence, and a water separation unit. In the first part of this work, two approaches for the water separation are investigated. First, the adsorption equilibrium from the (formaldehyde + methanol + water) system onto zeolite 3A is studied. Adsorption isotherms are presented, a physico-chemical model is developed, and adsorption enthalpies are estimated. The adsorption equilibrium model is extended to also consider systems containing OME_n. Experimental breakthrough curves obtained from a laboratory-scale packed column are presented. A column model is developed. The model exhibits good predictive accuracy for breakthrough curves, making it an essential tool for process scale-up. A feasible regeneration approach is presented. Next, a pervaporation-based approach for water separation utilizing SiO_2 membranes is investigated. Fourteen experiments conducted on a continuous setup demonstrate a reasonable selectivity of the membranes for water, with no observed flux or permeate quality deterioration across repeated experiments. These results underline the fundamental feasibility of using pervaporation with SiO_2 membranes for water separation in water-tolerant $OME_{3–5}$ production processes. Finally, the water separation is integrated with the other process units in a continuous mini-plant. Hereby, the water separation is done via pervaporation with SiO_2 membranes. The first distillation column is operated at several steady-state operating points to exclude solid precipitation and to examine trade-offs in the qualities of head and bottom products. Additionally, the column profiles are compared with simulation. The overall mass balance of the process is analysed. The scenario in which adsorption is used to carry out the water separation is analysed through a simulation study. The findings affirm the viability of the individual operation units, as well as the overall feasibility of the process.

Kurzfassung

Poly(oxymethylen) dimethylether mit Kettenlängen $n = 3$ bis 5 (OME_{3-5}) sind vielversprechende synthetische Dieselkraftstoffe, die eine saubere Verbrennung aufweisen. Während konventionelle wasserfreie Herstellungsprozesse gut etabliert sind, bieten wassertoleante $OME_3{}_{-5}$-Produktionsprozesse eine interessante Alternative, die bisher noch nicht im industriellen Maßstab realisiert wurde. Diese Prozesse haben den Vorteil, kostengünstigere Ausgangsmaterialien zu nutzen, allerdings auf Kosten eines komplexeren Downstreamings, insbesondere im Hinblick auf einen anspruchsvollen Wasserabtrennungsschritt.

Diese Arbeit beschäftigt sich mit einem kürzlich entwickelten wassertoleranten OME_{3-5}-Produktionsprozess, der aus einem Reaktor, einer Destillationssequenz und einer Wasserabtrennungseinheit besteht. Im ersten Teil dieser Arbeit werden zwei Ansätze für die Wasserabtrennung untersucht. Zunächst wird das Adsorptionsgleichgewicht des Systems (Formaldehyd + Methanol + Wasser) auf Zeolith 3A untersucht. Adsorptionsisothermen werden dargestellt, ein physikochemisches Modell wird entwickelt und Adsorptionsenthalpien werden abgeschätzt. Das Adsorptionsgleichgewichtsmodell wird auf Systeme erweitert, die OME_n enthalten. Es werden experimentelle Durchbruchskurven aus einer Festbettkolonne im Labormaßstab vorgestellt. Ein Modell für die Adsorptionskolonne wird entwickelt. Das Modell weist eine gute Vorhersagegenauigkeit für Durchbruchkurven auf und ist somit ein unverzichtbares Werkzeug für das Scale-Up des Prozesses. Ein Regenerationsansatz für das Adsorbent wird vorgestellt. Anschließend wird ein auf Pervaporation basierender Ansatz zur Wasseraufbereitung unter Verwendung von SiO_2-Membranen untersucht. Experimente in einer Pervaporationsanlage zeigen eine mäßige Selektivität der Membranen für Wasser, wobei bei wiederholten Experimenten keine Verschlechterung des Durchflusses oder der Permeatqualität beobachtet wurde. Diese Ergebnisse unterstreichen die gründsätzliche Machbarkeit des Einsatzes von Pervaporation mit SiO_2-Membranen zur Wasserabtrennung in wassertoleranten OME_{3-5}-Produktionsprozessen. Schließlich wird die Wasserabtrennung mit den anderen Prozesseinheiten in einer kontinuierlichen Miniplant integriert, wobei die Wasserabtrennung mittels Pervaporation mit SiO_2-Membranen erfolgt. Die erste Destillationskolonne wird an mehreren Betriebspunkten in einen stationären Zustand gebracht, um Feststoffaus-

fall auszuschließsen und Trade-Offs in den Qualitäten von Kopf- und Sumpfprodukten zu untersuchen. Zudem werden die Kolonnenprofile mit Simulation verglichen. Die Gesamtmassebilanz des Prozesses wird analysiert. Das Szenario, in dem Adsorption zur Wasserabtrennung verwendet wird, wird durch eine Simulationsstudie analysiert. Die Ergebnisse bestätigen die Machbarkeit der einzelnen Prozesseinheiten sowie des Gesamtprozesses.

Declaration

This dissertation contains material that has been published previously or that is included in submitted publications. In the following, these publications are listed together with a statement on the contributions of the author of the present dissertation.

Parts of the following article can be found in Chapter 2:

- A. Ferre, J. Burger: Coadsorption Equilibria on Molecular Sieves 3A and Densities of Liquid Mixtures Containing Formaldehyde, Methanol, and Water at 295.15 and 313.15 K, Industrial & Engineering Chemistry Research 60 (2021) 15256-15263.

  The author set up and carried out the experiments, and evaluated the results. The author developed the model and carried out the parametrization. The author performed the process simulation and evaluated the results. The author wrote the manuscript.

The following publication is referenced in both Chapter 2 and Chapter 4:

- A. Ferre, N. Zistler, J. Burger: Adsorptive Drying of Liquid Mixtures Containing Formaldehyde, Methanol, Water, and Poly(oxymethylene) Dimethyl Ethers on Zeolite 3A, Industrial & Engineering Chemistry Research 63 (2024) 5289-5298.

  The author set up and carried out the experiments together with Nina Zistler. The author developed the model and carried out the parametrization together with Nina Zistler. The author performed the process simulation and evaluated the results. The author wrote the manuscript.

The content of Chapter 3 is partially based on the following article:

- A. Ferre, D. Worch, J. Voggenreiter, U. Lubenau, J. Burger: Dewatering of Mixtures Containing Formaldehyde, Methanol, Water, and Poly(oxymethylene) Dimethyl Ethers by Pervaporation: Membrane Screening and Mini-Plant Operation, Journal of Membrane Science 690 (2024) 122206.

  The author set up and carried out the experiments together with Johannes Voggenreiter. The author developed the model and carried out the parametrization. The

author performed the simulation and evaluated the results. The author wrote the manuscript.

Finally, Chapter 4 is mainly based on the following articles:

- A. Ferre, J. Voggenreiter, C. F. Breitkreuz, D. Worch, U. Lubenau, H. Hasse, J. Burger: Experimental Demonstration of the Production of Poly(oxymethylene) Dimethyl Ethers from Methanolic Formaldehyde Solutions in a Continuous Mini-Plant, submitted to Chemical Engineering Research & Design (2024).

  The author set up and carried out the mini-plant experiments together with Johannes Voggenreiter. The author performed the simulation and evaluated the results. The author wrote the manuscript. The manuscript is currently in the revision process.

- A. Ferre, J. Voggenreiter, Y. Tönges, J. Burger: Demonstration Plant for the Synthesis of OME Fuels, MTZ Worldwide 82 (2021) 26-34.

  The author wrote the manuscript.

Contents

List of Symbols

Latin symbols

a, b	Correlation parameters
a_i	Activity of the component i in the bulk phase
A_j, B_j, C_j, D_j	Correlation parameters
A_{membrane}	Membrane area
d_{crit}	Critical diameter
D_{ax}	Dispersion coefficient
ΔH_i^{ads}	Adsorption enthalpy of component i
J	Total flux
$\tilde{J}_{\text{WA}}$	Overall flux of water
K_j^{ads}	Langmuir adsorption constant of component i
K_j^{chem}	Chemical equilibrium constant of reaction j based on mole fractions
k^{disp}	Proportionality constant for the dispersion coefficient
k_i^{LDF}	Overall mass transfer coefficient of component i
$\dot{m}$	Mass flow rate
$\dot{m}^{\text{feed}}$	Mass flow rate of feed
m_{ads}	Mass of adsorbent
m^{ads}	Total adsorbed mass
$\tilde{m}_i^{\text{ads}}$	Overall adsorbed mass of component i
m_{liq}	Mass of liquid
m_{feed}	Feed mass
$m_{\text{liq}}^{\text{rem}}$	Mass of liquid removed
$m_{\text{liq}}^{\text{feed}}$	Initial mass of liquid
m_{cat}	Mass of dry catalyst
m_{perm}	Mass of permeate
M_i	Molar mass of component i
MR_i	Mass recovery of component i in the distillate
n	Oligomer chain length
p	Pressure

P	Distillate-to-feed mass ratio
R	Ideal gas constant
t	Time
T	Temperature
q_i	Adsorbent loading of component i
$q_{\mathrm{e},i}$	Adsorbent equilibrium loading of component i
$\tilde{q}_i$	Overall adsorbent loading of component i
$\tilde{q}_{\mathrm{e},i}$	Overall equilibrium adsorbent loading of component i
$\tilde{q}_{i,\mathrm{col}}$	Average overall column loading of component i
$q_{\mathrm{m},i}$	Langmuir parameter of component i
V	Volume
V_{flask}	Volume of the measuring flask
V_{ads}	Volume of the measuring flask
V_{liq}	Volume of liquid
w_i	True mass fraction of component i
$\tilde{w}_i$	Overall mass fraction of component i
$\tilde{w}_i^{\mathrm{ads}}$	Overall mass fraction of component i in the adsorbed (heavy) phase
$\tilde{w}_i^{\mathrm{feed}}$	Overall mass fraction of component i in the feed
$\tilde{w}_i^{\mathrm{liq}}$	Overall mass fraction of component i in the liquid (light) phase
$\tilde{w}_i^{\mathrm{perm}}$	Overall mass fraction of component i in the permeate
x_i	True mole fraction of component i
$\tilde{x}_i$	Overall mole fraction of component i
$\tilde{x}_i^{\mathrm{ads}}$	Overall mole fraction of component i in the adsorbed (heavy) phase
$\tilde{x}_i^{\mathrm{feed}}$	Overall mole fraction of component i in the feed
$\tilde{x}_i^{\mathrm{liq}}$	Overall mole fraction of component i in the liquid (light) phase
z	Spacial coordinate

Greek symbols

$\alpha_{i,j}$	Separation factor between the components i and j
ϵ	Porosity of the packed bed
η_{ij}	Stoichiometric coefficient of component i in reaction j
γ_i	Activity coefficient of component i
ρ_{liq}	Density of the bulk phase
ρ_{ads}	Density of the adsorbent
τ	Pseudo residence time

Abbreviations

exp	Experimental
FA	Formaldehyde
HF_n	Poly(oxymethylene) hemiformal of chain length n
ME	Methanol
MG_n	Poly(oxymethylene) glycol of chain length n
min	Minimum
mod	Modelled
OME_n	Poly(oxymethylene) dimethyl ether of chain length n
WA	Water

1 Introduction

1.1 State of the Art

Our planet and its inhabitants face grave threats due to the relentless rise in atmospheric CO_2 concentrations and global average temperatures, driven by human activities. These threats include extreme weather events, rising sea levels, species extinction, and human health risks [1]. The transportation sector is a major culprit, with fossil fuel combustion being a significant source of CO_2 emissions. With global transportation and trade continuing to expand, the exploration of alternative solutions like renewable fuels is urgently needed. Recognizing this urgency, the European Union recently raised its 2030 renewable energy target from 32% to 42.5% [2]. However, this revised target presents significant challenges, particularly in the mobility sector's heavy reliance on fossil fuels. Although electric vehicles offer a mitigation pathway, transitioning sectors like trucking, aviation, and maritime to electric powertrains is significantly more complex. To address this challenge, diverse renewable fuels like Fischer-Tropsch fuels, methanol, and poly(oxymethylene) dimethyl ethers can be produced from various raw materials, including biomass and captured CO_2 obtained through carbon capture or direct air capture processes.

Poly(oxymethylene) dimethyl ethers (OME_n) represent a class of synthetic diesel fuels with the potential to significantly reduce soot emissions during combustion [3–8]. Furthermore, OME_n contribute to the reduction of unburned hydrocarbons and carbon monoxide emissions [5]. The diminished formation of soot enables diesel engines to overcome the traditional trade-off between soot and nitrogen oxides emissions [6] For diesel fuel applications, OME_n chains with a desired length of $n = 3$ to 5 (OME_{3-5}) have been identified [6, 8]. Numerous studies have highlighted the advantages of OME_n in combustion [3, 5, 6, 9]. OME_n can be used pure or as blends with conventional diesel fuels. For example, it has been shown that the addition of only 5% OME_2 to conventional diesel fuel can lead to a remarkable 30% reduction in soot emissions [9]. Also blends of OME_n with hydrogenated vegetable oils (HVO) have been recently discussed as an interesting option, as HVO are already produced on a large scale [10, 11]. Another

advantage of OME_n lies in the similarity of physico-chemical properties between OME_n and conventional diesel fuels, allowing for their integration into existing diesel engines and infrastructure [8, 12].

$OME_{3–5}$ are produced from methanol (ME) exclusively. The production process involves the partial conversion of methanol into formaldehyde (FA), the monomeric building block of the OME_n chains. The subsequent reaction of formaldehyde and methanol (or their derivatives) leads to the formation of OME_n. Various production pathways exist, differing in reactor types, separation methods, and intermediates. Water (WA) can be present in the system or not. This distinction leads to the classification of production processes as either water-free or water-tolerant [13].

In the slightly older water-free processes, a dry formaldehyde source such as trioxane, paraformaldehyde, or monomeric formaldehyde is reacted with either methylal [14–18] or dimethyl ether [17, 19–21]. These processes have the advantage of high product selectivity and low-side product formation. However, they require the production of intermediate reactants from formaldehyde and methanol in prior steps. Extensive research has been conducted on water-free processes, and to date, the only realized industrial production processes of OME_n belong to this class [19].

In contrast, water-tolerant processes enable the direct conversion of aqueous formaldehyde solutions and methanol into OME_n without the need to synthesize or isolate the aforementioned intermediates. Water-tolerant processes are characterized by lower selectivities towards $OME_{3–5}$ in a single reactor pass compared with water-free processes. Formaldehyde leaves the reactor also in the oligomers poly(oxymethylene) glycols and poly(oxymethylene) hemiformals, which are not present in water-free processes. These additional compounds make the downstream processing complex, leading to a variety of different process concepts. For example, Oestreich et al. [22] proposed an extraction procedure to isolate the desired OME_n using different hydrocarbons as extraction agents. Han et al. [23] described a simultaneous extractive and azeotropic distillation process using water as entrainer. However, these concepts have not been developed beyond the laboratory scale. Schmitz et al. [24] developed a process consisting of a reactive distillation and a pervaporation or adsorption module for water removal. Property data [25–27] to simulate the process are known and a conceptual design study [24] has been done. A more recent water-tolerant process proposal by Mantei et al. [28, 29] shares similarities with the concept of Schmitz et al. [24] but employs reactive distillation for water removal instead of a pervaporation or adsorption unit. The concept was experimentally demonstrated in continuous operation, however without closing recycles [29].

In the $OME_{3–5}$ process by Schmitz et al., the feed comprises a methanolic formaldehyde

solution containing approximately 0.05 g/g to 0.1 g/g of water. This feed is mixed with a liquid recycle streams before entering the reactor. In the heterogeneously acid-catalysed reactor, a stream containing formaldehyde, water, methanol, and OME_n of various chain lengths is obtained. The isolation of the desired product fraction $OME_{3–5}$ is carried out in a distillation column that separates $OME_{\geq 3}$ as bottom product from a stream containing mainly formaldehyde, methanol, water and $OME_{\geq 2}$. Schmitz et al. [24] also suggested to further purify the product with a second distillation column that narrows down the product $OME_{3–5}$. Before the distillate of the first distillation column is recycled to the reactor, water is removed from the stream. The water separation is essential for two reasons. Firstly, formaldehyde solutions typically contain water, and secondly, water is produced stoichiometrically as a by-product in the OME_n synthesis from methanol and formaldehyde. Given several azeotropes, it has been shown that distillation is not the preferred option to deal with this separation task [24].

The reactor has been experimentally studied in mini-plant scale as an isolated unit before by Voggenreiter et al. [30, 31].

Regarding the water separation, laboratory scale experiments performed by Schmitz et al. [32] support the feasibility of the pervaporative separation, but the long-term stability of the membranes remains an open question. Similarly, preliminary batch equilibrium experiments performed by Schmitz et al [32] suggest that the adsorptive separation of water from these mixtures using zeolite 3A is feasible. However, exclusive water adsorption was assumed. Due to size considerations, the adsorption of particularly formaldehyde and methanol cannot be excluded. Neither the regeneration of the zeolite 3A nor continuous operation including the determination of breakthrough curves in a continuous setup have been studied.

Concerning the distillation step, Schmitz et al. also performed laboratory scale experiments [27]. However, the conditions at which these experiments were performed differ notably from the designated process conditions. Evaluation in continuous operation as well as an integration of all process units including recycles and at designated process conditions is missing.

1.2 Goals of This Thesis

This work tackles these open gaps, delving deeper into the water-tolerant $OME_{3–5}$ process developed by Schmitz et al. [24] and bringing it an important step closer to industrial realization. Figure 1 presents the block flow diagram of the process and gives

an overview of the present work. Note that the second distillation column proposed by Schmitz et al. is omitted in this work, cf. Chapter 4 for more details.

The first two chapters deal with two different options for the water separation in the water-tolerant OME_n production processes. Chapter 2 investigates an adsorption-based approach using zeolite 3A. First, the adsorption equilibrium for the system (formaldehyde + methanol + water) in the liquid phase is experimentally determined and modelled. Subsequently, breakthrough curves obtained from a laboratory-scale packed column and a comprehensive column model are presented. Additionally, the regeneration potential of the zeolite 3A is discussed.

Chapter 3 focuses on a pervaporation-based alternative using a SiO_2 membrane. This membrane was chosen after initial screening, which involved testing three different membranes with pure water and process mixtures at varying temperatures between 40 °C and 70 °C on a laboratory scale setup [33]. Based on water flux and selectivity, the SiO_2 membrane was selected as the most promising. This work presents pervaporation experiments within the system (formaldehyde + methanol + water + OME_n) and a model to describe the water flux as a function of the water concentration in the feed are presented. The selectivity of the membrane towards water is discussed and alternatives for further increasing the water content of the permeate stream are explored.

Chapter 4 integrates the water separation together with the rest of the process units. Mini-plant experiments that closely approximate the operating conditions proposed by Schmitz et al. [24] are presented. The experiments are performed in a mini-plant located at the technology laboratory of the TUM Campus Straubing for Biotechnology and Sustainability and comprises a tubular reactor, a distillation column, and a pervaporation unit for the water separation. Experimental and modelled column profiles are compared, assessing the potential for solid precipitation. Trade-offs in product quality are explored, and overall mass balances of the process are presented. Furthermore, the process is simulated to explore the scenario where adsorption is employed as a water separation unit. A comparative analysis between pervaporation and adsorption for water separation in the $OME_{3–5}$ process by Schmitz et al. [24] is presented.

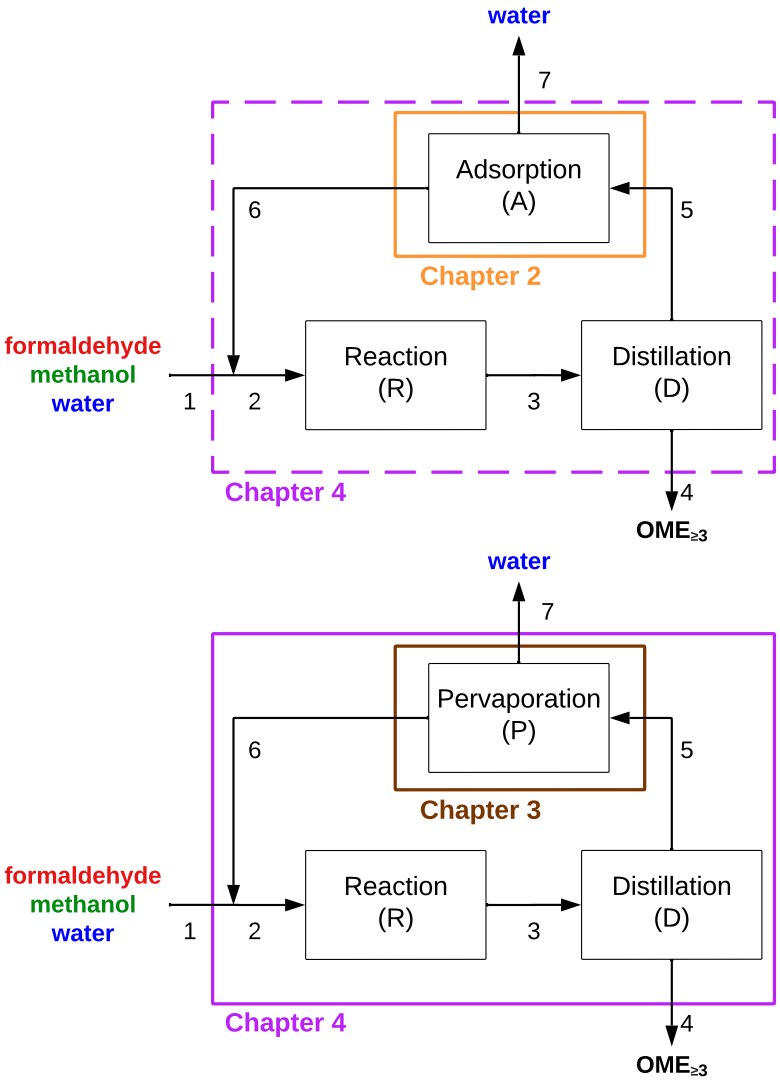

Figure 1: Process flow diagram of the OME_{3-5} process by Schmitz et al. [24] with the two alternatives for water separation: adsorption (Chapter 2), and pervaporation (Chapter 3). The overall process is studied in Chapter 4. Boxes with solid lines represent processes studied through simulation and experimentally while boxes with dashed lines represent processes studied only through simulation.

2 Water Separation via Adsorption

2.1 Introduction

Adsorption on zeolites, silica gels, or aluminas is a widely utilized technique for water removal. Some studies have focused on drying non-polar solvents such as toluene, benzene, or xylene using different adsorbents like zeolite 3A, zeolite 4A, and activated alumina [34, 35]. Others have delved into the drying of alcohols on several adsorbents including zeolite 3A and 4A: methanol [36–38], ethanol [37–40], 1-propanol [37, 38, 40, 41], 2-propanol [42, 43], 1-butanol [37, 38, 40], 1-pentanol [37, 38], and 1-hexanol [37, 38].

All these investigations have primarily examined the equilibrium or kinetics of water adsorption while mostly disregarding the adsorption of other components. Pahl et al. [38] pointed out that adsorption of methanol should be considered in systems containing water and methanol. Santos et al. [44] investigated the equilibrium and kinetics of the adsorptive drying of dimethyl carbonate on zeolite 3A under high-pressure conditions, revealing significant adsorption of dimethyl carbonate within the adsorbent pores.

Concerning systems containing formaldehyde, the potential for adsorbing water from such mixtures using zeolite 3A was initially suggested by Hasse [45]. The literature on adsorption for systems containing formaldehyde is sparse. Some research has focused on gas phase adsorption to mitigate hazardous formaldehyde emissions. For example, Carter et al. [46] provided single-component adsorption isotherms of formaldehyde on three different activated carbons, while Bellat et al. [47] reported adsorption equilibrium data of water and formaldehyde on NaX and NaY zeolites. Regarding the liquid phase, Schmitz et al. [24] presented spotty measurements of single-component adsorption isotherms of water from liquid mixtures containing (formaldehyde + methanol + water + OME_n) on zeolite 3A. Another recent study by Novikova et al. [48] focuses on formaldehyde adsorption from aqueous solutions using metakaolin-based adsorbents. In the field of OME_n, Schmitz et al. [24] conducted preliminary batch equilibrium experiments in the system (formaldehyde + methanol + water + OME_n) on zeolite 3A, assuming exclusive water adsorption.

Zeolite 3A has a window aperture of approximately 3 Å. The critical diameter d_{crit} and

the minimum kinetic diameter d_{kin} of formaldehyde, methanol and water are given in Table 1.

Table 1: Minimum kinetic diameter and critical diameter of formaldehyde [47], methanol [38, 49] and water [49].

	d_{kin} /Å	d_{crit} /Å
formaldehyde	2.4	-
methanol	3.8	3.0
water	3.0	-

Since none of the compounds is significantly larger than 3 Å, adsorption of formaldehyde and methanol besides water is expected and needs to be quantified. Also the role of OME_n in the adsorption equilibrium is up to now unclear. While their adsorption is not expected due to size and polarity considerations, experimental evidence confirming this fact is missing. Also, insights regarding the zeolite 3A regeneration as well as the determination of breakthrough curves in a continuous setup is lacking.

This chapter tackles all these gaps by meticulously studying the adsorption of the system (formaldehyde + methanol + water + OME_n) in the liquid phase on zeolite 3A. Firstly, the adsorption equilibrium of the ternary system (formaldehyde + methanol + water) is studied. Adsorption isotherms in the binary subsystems (formaldehyde + water), (methanol + water) and (formaldehyde + methanol) are determined. A physicochemical model is presented, which explicitly takes the chemical reactions occurring in the bulk phase into account. In order to fit the parameters of the model consistently, single-component water adsorption isotherms from 2-propanol are determined as well. Adsorption enthalpies are estimated based on the temperature dependence of the model parameters. Other key results of the present work are the novel density data of methanolic formaldehyde solutions and the respective correlations. The model is extrapolated to systems also containing OME_n. Furthermore, experimental data on breakthrough curves of formaldehyde, methanol, and water obtained from a laboratory-scale packed column is presented. The regeneration of the zeolite is discussed. A comprehensive column model that considers the chemical reactions in the liquid phase, the adsorption equilibrium, the mass balances, the adsorption kinetics, and the fluid dynamics is presented. The model exhibits good predictive accuracy for breakthrough curves, making it an essential tool for process scale-up.

2.2 Experimental Methodology

2.2.1 Chemicals and Adsorbent

Paraformaldehyde (> 0.95 g/g) was purchased from Sigma-Aldrich. Methanol (> 0.999 g/g) was purchased from Merck. Ultra-pure water was obtained from a PURELAB Classic water purification system from ELGA. 2-propanol (> 0.999 g/g) and acetone (> 0.998 g/g) were purchased from ChemSolute. Zeolite 3A in form of beads with a diameter of 1.6–2.5 mm were purchased from Carl Roth.

2.2.2 Preparation of Feed Solutions and Conditioning of the Adsorbent

Aqueous formaldehyde solutions for the experiments B9 - B11 and B21 - B24 were prepared by dissolving paraformaldehyde in ultra pure water at 70 °C and stirring for 3 days, following Hasse [45]. Neither sodium hydroxide nor any other chemical was added to the solutions to accelerate the depolymerization process since they could alter the adsorption equilibrium [50]. Methanolic formaldehyde solutions for the experiments B13 - B16 and B26 - B28 were obtained analogously but the temperature was set to 60 °C. The methanolic solutions contained up to 0.02 g/g water, since paraformaldehyde contains water. The water content was reduced to < 0.001 g/g by storing the methanolic solutions over zeolite 3A for at least 24 hours.

The feed solutions for the experiments B40 and B40a were obtained from the OME_{3-5} mini-plant (cf. Chapter 4). The composition of the feed was determined through chemical analysis prior to its usage (cf. Section 2.2.3).

For experiments involving fresh adsorbent, the zeolite was dried prior to usage for 24 hours at 298 °C and atmospheric pressure within a drying cabinet. This temperature was chosen as temperatures above 300 °C can lead to damage of the adsorbent and loss of its capacity [51]. Experiments with used adsorbent involved washing the zeolite 3A with ultrapure water and allowing it to air dry for 24 hours. Subsequently, the adsorbent was regenerated for 24 hours at 185 °C and 100 mbara within a vacuum drying cabinet.

2.2.3 Analytics of the Liquid Mixtures

The overall mass fraction of formaldehyde was determined by the sodium sulfite method [25] using hydrochloric acid as titrant. The overall mass fraction of water was determined

by Karl-Fischer titration [25]. Both methods have a relative error of 2% [25]. In the equilibrium experiments with binary and ternary mixtures (experiments B1 - B39), the overall mass fractions of methanol and 2-propanol were determined as complement to 1 g/g. In the equilibrium experiments including OME_n, (experiments B40 and B40a), as well as in the column experiments (experiments D1 - D2 and C1 - C3), the overall mass fractions of methanol, of 2-propanol, acetone, and OME_n were determined by gas chromatography with 1,4-dioxane as the internal standard, with a relative error of 5%. Details regarding the method can be found [52].

2.2.4 Experimental Plan

Four batch experiments (Z1 - Z4) were performed with four different non-adsorbing solvents to determine the density of the zeolite 3A (cf. Section 2.2.6). The employed solvents were ethanol, 1-propanol, 2-propanol, and acetone. Table 2 gives an overview of the feed compositions and temperatures of experiments Z1 - Z4.

Table 2: Overview of the batch experiments performed to determine the density of the zeolite 3A. For each experiment, the feed composition and the temperature are reported.

experiment	$\tilde{w}_i^{\text{feed}}$ / g/g				T / °C
	ethanol	1-propanol	2-propanol	acetone	
Z1	1.000	-	-	-	22
Z2	-	1.000	-	-	22
Z3	-	-	1.000	-	22
Z4	-	-	-	1.000	22

To develop the model for the adsorption equilibrium, a series of batch equilibrium experiments was conducted. Initially, seven experiments (B1 - B7) were executed using binary mixtures of 2-propanol and water. 2-propanol was selected as a non-adsorbing solvent due to size considerations. The calculated equilibrium loadings of 2-propanol consistently remained below 0.01 g/g, confirming that 2-propanol does not significantly adsorb. These experiments aimed to determine the parameters of the adsorption isotherm for water, cf. Section 2.3.5. Subsequently, twenty-five experiments (B8 - B32) were performed in the binary subsystems (formaldehyde + water), (methanol + water), and (formaldehyde + methanol). From these experiments, the parameters of the adsorption isotherms for methanol and formaldehyde were fitted. To validate the model, seven

experiments (B33 - B39) were conducted with ternary mixtures containing (formaldehyde + methanol + water). Approximately half of the experiments were carried out at 22 °C, while the remaining half occurred at 40 °C. To assess the validity of the model in the presence of OME_n and the impact of the adsorbent regeneration, two additional experiments (B40 and B40a) were undertaken. In these two experiments, the initial composition was inspired by the operating point of the $OME_{3–5}$ process described by Schmitz et al.[24] and was the same in both experiments. Experiment B40 utilized fresh zeolite 3A, whereas experiment B40a employed the same zeolite 3A after regeneration. Table 3 gives an overview of the feed compositions and temperatures of experiments B1 - B40a. Additionally, for a better visualization of the experimental plan, the feed compositions of the experiments within the system (formaldehyde + methanol + water), i.e., experiments B8 - B39, can be observed in Figure 2.

Table 3: Overview of the adsorption equilibrium experiments. For each experiment, the feed composition and the temperature are reported.

experiment	$\tilde{w}_i^{\text{feed}}$ / g/g					T / °C
	FA	WA	ME	OME_n	2-propanol	
B1	-	0.011	-	-	0.989	22
B2	-	0.031	-	-	0.969	22
B3	-	0.051	-	-	0.949	22
B4	-	0.070	-	-	0.930	22
B5	-	0.013	-	-	0.987	40
B6	-	0.064	-	-	0.936	40
B7	-	0.089	-	-	0.911	40
B8	-	1.000	-	-	-	22
B9	0.094	0.906	-	-	-	22
B10	0.200	0.800	-	-	-	22
B11	0.284	0.716	-	-	-	22
B12	-	-	1.000	-	-	22
B13	0.144	-	0.856	-	-	22
B14	0.244	-	0.756	-	-	22
B15	0.369	-	0.631	-	-	22
B16	0.530	-	0.470	-	-	22

Table 3 – continued from previous page

experiment	$\tilde{w}_i^{\text{feed}}$ / g/g					T / °C
	FA	WA	ME	OME_n	2-propanol	
B17	-	0.906	0.094	-	-	22
B18	-	0.694	0.306	-	-	22
B19	-	0.248	0.752	-	-	22
B20	-	0.097	0.903	-	-	22
B21	-	1.000	-	-	-	40
B22	0.101	0.899	-	-	-	40
B23	0.199	0.801	-	-	-	40
B24	0.283	0.717	-	-	-	40
B25	-	-	1.000	-	-	40
B26	0.197	-	0.803	-	-	40
B27	0.244	-	0.756		-	40
B28	0.385	-	0.616		-	40
B29	-	0.750	0.250	-	-	40
B30	-	0.494	0.506	-	-	40
B31	-	0.253	0.747	-	-	40
B32	-	0.051	0.949	-	-	40
B33	0.390	0.211	0.399	-	-	22
B34	0.213	0.207	0.580	-	-	22
B35	0.206	0.408	0.386	-	-	22
B36	0.205	0.610	0.185	-	-	22
B37	0.191	0.205	0.604	-	-	40
B38	0.191	0.410	0.399	-	-	40
B39	0.284	0.184	0.533	-	-	40
B40	0.144	0.122	0.045	0.689	-	22
B40a	0.144	0.122	0.045	0.689	-	22

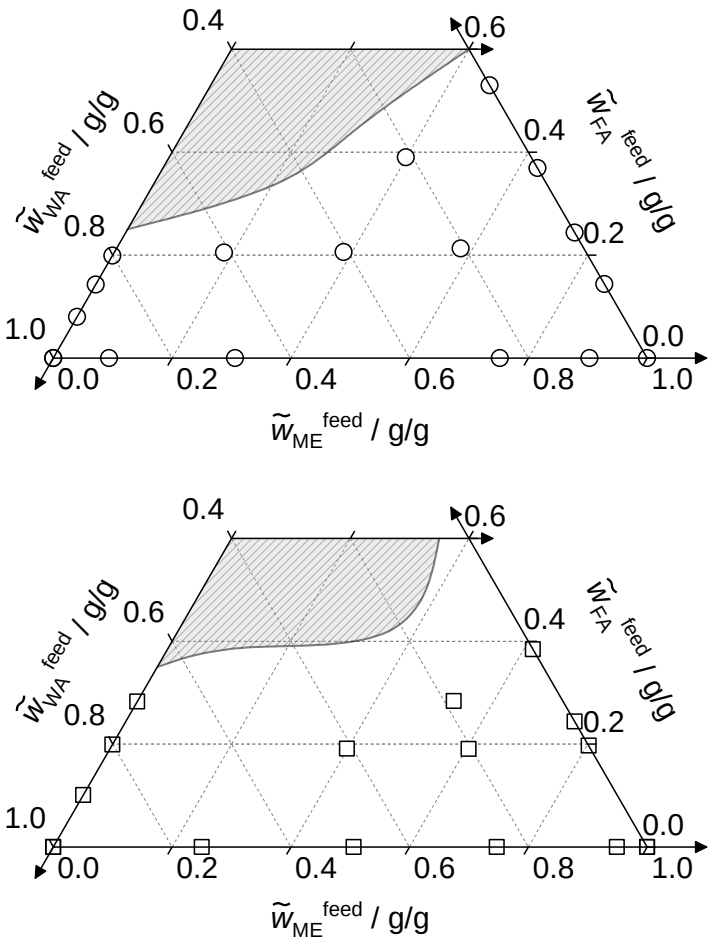

Figure 2: Feed compositions of the liquid solutions used in the experiments B8 - B20 at 22 °C (top,) and B21 - B32 at 40 °C (bottom). Gray-shaded area: Formaldehyde precipitation (qualitatively).

Moving on to the continuous fixed-bed experiments, two experiments with 2-propanol and acetone on fresh zeolite 3A (D1 and D2) were conducted to characterize the fluid dynamic behaviour of the column. Subsequently, a series of adsorption experiments were performed with process mixtures and varying feed flow rates. The feed composition was inspired by the operating point of the water-tolerant OME_{3-5} production process proposed by Schmitz et al. [24]. Experiments C1, C2, and C3 were carried out using fresh zeolite 3A. Experiments C2a, C2b, and C2c employed the zeolite 3A used in experiment C2 but subjected to one, two, and three regeneration cycles, respectively. Table 4 lists the feed compositions and temperatures of the continuous adsorption experiments performed.

Table 4: Overview of the continuous dispersion and adsorption experiments. For each experiment, the feed composition and the feed mass flow rate are reported. Experiments marked with a * were used for parameter fitting.

experiment	$\tilde{w}_i^{\text{feed}}$ g/g						$\dot{m}^{\text{feed}}$ / g/min
	FA	WA	ME	OME_n	Acetone	2-propanol	
D1	-	-	-		1.000→0.000	0.000→1.000	10.8
D2*	-	-	-		1.000→0.000	0.000→1.000	18.0
C1	0.194	0.047	0.140	0.619	-	-	13.2
C2	0.150	0.038	0.121	0.691	-	-	19.8
C2a	0.150	0.038	0.121	0.691	-	-	19.8
C2b	0.150	0.038	0.121	0.691	-	-	19.8
C2c	0.150	0.038	0.121	0.691	-	-	19.8
C3*	0.194	0.047	0.140	0.619	-	-	22.2

2.2.5 Measurement of the Adsorption Equilibrium

The density-bottle method developed by Yu et al. [53] was used to determine the equilibrium loadings of each component. Approximately 15 g of dry zeolite 3A were weighed into an empty glass measuring flask (V_{flask} = 50 mL). The feed solution was then added to the flask so that the level of the liquid was above the 50 mL mark on the flask. The flask was sealed and the solid-liquid mixtures were equilibrated for at least 72 hours, while gently shaken using an orbital shaker Rotamax 120. Preliminary experiments showed that 48 hours were enough for the mixtures to reach the equilibrium. This was proven by repeated sampling. Isothermal conditions were achieved by placing the entire setup into a thermostatic box. The temperature was measured directly in

the flask with a resistance thermometer. During adsorption, the liquid level in the flask decreased but remained above the 50 mL mark. Then, the shaker was turned off and the flask was weighed to check that the evaporation loss was insignificant (in the experiments it was always lower than 0.5% of the total mass). A 2 mL syringe was used to remove liquid from the flask until the liquid level reached the graduation marking.

During the procedure, the following quantities were measured: the masses of dry zeolite 3A (m_{ads}), initially added feed solution ($m_{\mathrm{liq}}^{\mathrm{feed}}$), and removed liquid ($m_{\mathrm{liq}}^{\mathrm{rem}}$). The overall mass fractions of formaldehyde, water and methanol in the initially added liquid ($\tilde{w}_i^{\mathrm{feed}}$) and the liquid bulk in equilibrium ($\tilde{w}_i$) were obtained through chemical analysis. The specific densities of the liquid bulk in equilibrium (ρ_{liq}) and the specific density of the dry zeolite (ρ_{ads}) were also determined (cf. Section 2.2.6). All experiments were at least duplicated (normally triplicated) to ensure the reproducibility of the results.

The basis of the method is the measurement of the density change in the solid-liquid mixture during the adsorption, assuming that the volume V_{ads} of the adsorbent is constant in this process.

Under this premise, the following equations apply: [53]

$$V_{\mathrm{flask}} = V_{\mathrm{ads}} + V_{\mathrm{liq}} \tag{1}$$

$$V_{\mathrm{ads}} = \frac{m_{\mathrm{ads}}}{\rho_{\mathrm{ads}}} \tag{2}$$

$$V_{\mathrm{liq}} = \frac{m_{\mathrm{liq}}}{\rho_{\mathrm{liq}}} \tag{3}$$

Therein, m_{liq} is the mass of the liquid bulk in equilibrium. Inserting Equations (2) and (3) into Equation (1) and solving for m_{liq} leads to:

$$m_{\mathrm{liq}} = V_{\mathrm{liq}} \cdot \rho_{\mathrm{liq}} = \left(V_{\mathrm{flask}} - \frac{m_{\mathrm{ads}}}{\rho_{\mathrm{ads}}}\right) \cdot \rho_{\mathrm{liq}} \tag{4}$$

Using the total mass balance

$$m^{\mathrm{ads}} = m_{\mathrm{liq}}^{\mathrm{feed}} - m_{\mathrm{liq}}^{\mathrm{rem}} - m_{\mathrm{liq}} \tag{5}$$

and the component mass balance

$$\tilde{m}_i^{\mathrm{ads}} = m_{\mathrm{liq}}^{\mathrm{feed}} \cdot \tilde{w}_i^{\mathrm{feed}} - m_{\mathrm{liq}}^{\mathrm{rem}} \cdot \tilde{w}_i - m_{\mathrm{liq}} \cdot \tilde{w}_i \tag{6}$$

the total adsorbed mass m^{ads} and the overall adsorbed mass $\tilde{m}_i^{\mathrm{ads}}$ of component i are determined. The specific overall adsorbed mass or equilibrium loading $\tilde{q}_{\mathrm{e},i}$ of component i follows:

$$\tilde{q}_{\mathrm{e},i} = \frac{\tilde{w}_i^{\mathrm{feed}} \cdot m_{\mathrm{liq}}^{\mathrm{feed}} - \tilde{w}_i \cdot \left[m_{\mathrm{liq}}^{\mathrm{rem}} + \left(V_{\mathrm{flask}} - \frac{m_{\mathrm{ads}}}{\rho_{\mathrm{ads}}} \right) \cdot \rho_{\mathrm{liq}} \right]}{m_{\mathrm{ads}}} \tag{7}$$

2.2.6 Density of the Adsorbent and the Liquid Solutions

The specific density of the zeolite 3A was determined as suggested by Yu et al. [53] by performing adsorption experiments with four different solvents with different critical diameters, all of them significantly larger than the window aperture of zeolite 3A: ethanol (d_{crit} = 4.50 Å)[54], 1-propanol (d_{crit} = 4.56 Å)[54], 2-propanol (d_{crit} = 4.90 Å)[54], and acetone (d_{crit} = 4.79 Å)[54]. The experiments were performed in the same way as described above. Since these solvents are expected to act like non-adsorbing (inasmuch as their critical diameters are larger than the window aperture of the adsorbent), the specific density ρ_{ads} of the adsorbent can be found from Equations (4) and (5) setting $m^{\mathrm{ads}} = 0$:

$$\rho_{\mathrm{ads}} = \frac{\rho_{\mathrm{liq}} \cdot m_{\mathrm{ads}}}{V_{\mathrm{flask}} \cdot \rho_{\mathrm{liq}} - m_{\mathrm{liq}}^{\mathrm{feed}} - m_{\mathrm{liq}}^{\mathrm{rem}}} \tag{8}$$

The densities ρ_{liq} of the mixtures (formaldehyde + WA) were calculated using a correlation presented by Winkelmann et al [55]. Similar correlations were developed by measuring the densities ρ_{liq} of selected mixtures (formaldehyde + methanol) and (methanol + water) at 22 °C and 40 °C using an Anton Paar DMA 4500 density meter. The densities of the multicomponent mixtures were always determined experimentally.

2.2.7 Column Setup

Figure 3 presents a process flow diagram of the experimental setup employed in this work. The setup consists of the glass Hempel column C1, featuring dimensions of 0.5 m in height and 0.03 m in diameter. At the base of the column, a layer of glass wool is thoughtfully positioned to prevent any downward movement of the zeolite 3A. All

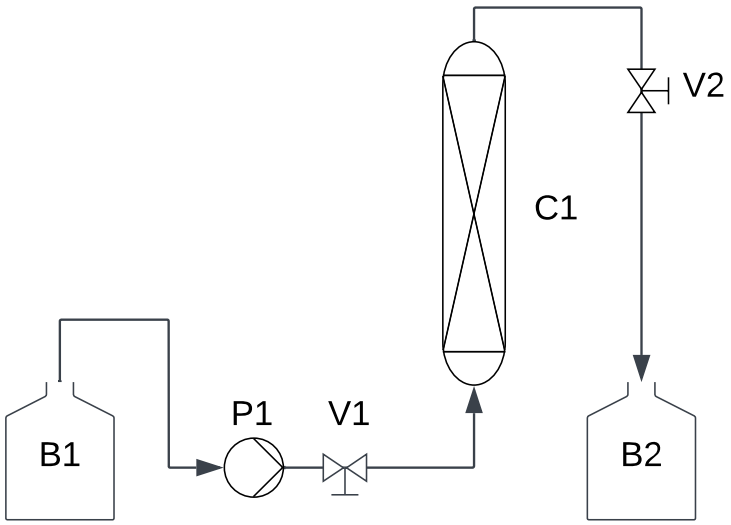

Figure 3: Process flow diagram of the adsorption column setup.

interconnections within the setup were established using flexible silicone hoses, chosen for their solvent resistance and adeptness at ensuring secure and snug fits.

The peristaltic pump P1 (iPump1Q, Landgraf Laborsysteme), equipped with the pump head JZ15B, establishes the fluid flow from the feed tank B1 throughout the column C1. This self-priming pump can operate bidirectionally and offers speed regulation ranging from 0.1 to 100 rpm. This speed range corresponds to a maximum volumetric flow rate of 120 mL/min, covering a wide range of residence times within the column. The pump P1 was calibrated for determining the flow rate based on pump speed before utilization. The outlet of the column C1 is collected into the tank B2. Samples for analysis can be extracted from the column outlet using the three-way stopcock V2. Additionally, the valve V1 can be utilized to drain any liquid from the column after the experiment.

The average column loading of component i at the time t, denoted as $\tilde{q}_{i,\mathrm{col}}(t)$, is determined by the following expression:

$$\tilde{q}_{i,\mathrm{col}}(t) = \frac{\dot{m}^{\mathrm{feed}} \cdot \tilde{w}_i^{\mathrm{feed}} \cdot t - \int_0^t (\dot{m} \cdot \tilde{w}_i)\,\mathrm{d}t}{m_{\mathrm{ads}}} \tag{9}$$

Here, $\dot{m}^{\mathrm{feed}}$ is the mass flow rate of the feed, $\tilde{w}_i^{\mathrm{feed}}$ is the overall mass fraction of compo-

nent i in the feed, $\dot{m}$ is the mass flow rate at the outlet of the column, m_{ads} is the mass of zeolite 3A, and $\tilde{w}_i$ is the overall mass fraction of species i at the outlet of the column. The integral is solved numerically using the trapezoidal rule. Note that when t is large enough, the average adsorbent loading $\tilde{q}_{i,\mathrm{col}}$ tends to the equilibrium adsorbent loading $\tilde{q}_{\mathrm{e},i}$ for a liquid phase composition of the feed.

In experiments D1 and D2, the column was initially filled with approximately 300 g of dry zeolite 3A. Subsequently, the column was loaded with acetone, and the desired feed flow rate was set. Once a continuous flow at the outlet of the adsorption column was observed, the feed was switched rapidly to 2-propanol.

For experiments C1 to C3, the column was also filled with around 300 g of dry zeolite 3A. At the time $t = 0$, the pump P1 was initiated with the desired feed flow rate. Samples were taken regularly at the outlet of the column.

2.3 Modelling Methodology

2.3.1 Chemical Reactions

Methanol, water, and formaldehyde form a reactive system: formaldehyde chemically binds to water and methanol by forming the oligomer species poly(oxymethylene) glycols (formula: $\mathrm{HO{-}(CH_2O)_{\mathit{n}}{-}H}$, abbreviation: MG_n) or poly(oxymethylene) hemiformals (abbreviation: HF_n, formula: $\mathrm{HO{-}(CH_2O)_{\mathit{n}}{-}CH_3}$), respectively. The oligomer formation is depicted in Reactions (10) - (13) [56]:

$$\mathrm{FA + WA} \rightleftharpoons \mathrm{MG_1} \tag{10}$$

$$\mathrm{FA + MG_{\mathit{n}-1}} \rightleftharpoons \mathrm{MG_{\mathit{n}}} \quad ; \quad n > 1 \tag{11}$$

$$\mathrm{FA + ME} \rightleftharpoons \mathrm{HF_1} \tag{12}$$

$$\mathrm{FA + HF_{\mathit{n}-1}} \rightleftharpoons \mathrm{HF_{\mathit{n}}} \quad ; \quad n > 1 \tag{13}$$

It was assumed that the chemical equilibrium in the liquid phase is established immediately and the kinetics of the reactions can be neglected. This assumption can be made because the reactions proceed rapidly even without a catalyst [26, 57]. Because of Reactions (10) to (13), the concentrations of methanolic and aqueous solutions of formaldehyde are usually expressed in two different ways [26]: While overall concentrations refer to the concentration of the solutions without considering the oligomer formation, true

concentrations take account of all poly(oxymethylene) glycols and poly(oxymethylene) hemiformals formed. Overall concentrations are denoted with a ˜ above the symbol, e.g., $\tilde{w}_{\mathrm{WA}}$ represents the overall mass fraction of water and w_{WA} the true mass fraction of water. The mathematical relations between overall concentrations and true concentrations are given in the Appendix A.1. In the experimental analytics of the present work, overall mass fractions are obtained and reported. For the models, true mass and mole fractions are used. The plots are expressed in terms of overall mass fractions.

For each chemical reaction j, the equilibrium constant $K_{x,j}^{\mathrm{chem}}$ based on mole fractions is given by:

$$K_j^{\mathrm{chem}} = \prod_i x_i^{\nu_{ij}} \tag{14}$$

where x_i represents the true mole fraction of component i in the liquid phase and ν_{ij} is the stoichiometric coefficient of species i in the reaction j. The temperature dependence of K_j^{chem} is described by:

$$\ln K_j^{\mathrm{chem}} = A_j + \frac{B_j}{T} \tag{15}$$

The parameters A_j, B_j, C_j, and D_j were taken from the work of Hahnenstein et al. [57] and are given in the Appendix A.2. In the present work, a maximum chain length of $n = 5$ was assumed for both poly(oxymethylene) glycols and poly(oxymethylene) hemiformals.

2.3.2 Adsorption Equilibrium

To model the adsorption equilibrium, the multi-component models Langmuir, Freundlich, Sips were tested [58–60]. The Langmuir model, which together with the Freundlich model has the smallest number of parameters, was found to be sufficient and performant, so it is used in the following. MG_1, HF_1 and the respective longer oligomers are assumed not to adsorb due to size considerations. The equilibrium loadings are modelled by:

$$\tilde{q}_{\mathrm{e},i} = \frac{q_{\mathrm{m},i} \cdot K_i^{\mathrm{ads}} \cdot a_i}{1 + K_{\mathrm{FA}}^{\mathrm{ads}} \cdot a_{\mathrm{FA}} + K_{\mathrm{ME}}^{\mathrm{ads}} \cdot a_{\mathrm{ME}} + K_{\mathrm{WA}}^{\mathrm{ads}} \cdot a_{\mathrm{WA}}} \;\; ; \;\; i = \mathrm{FA}, \mathrm{ME}, \mathrm{WA} \tag{16}$$

$$\tilde{q}_{\mathrm{e},i} = 0 \;\; ; \;\; i = \mathrm{OME}_n, 2-\mathrm{propanol}, \mathrm{acetone} \tag{17}$$

being $q_{\mathrm{m},i}$ and K_i^{ads} model parameters to be adjusted. The adsorption capacity $q_{\mathrm{m},i}$ represents the maximum achievable equilibrium loading of compound i and the adsorption constant K_i^{ads} is related to the affinity of the binding sites. As concentration measure in the liquid bulk, and hence the driving force for the adsorption, the true mass fractions w_i and the activities a_i (normalization according to Raoult) were considered:

$$a_i = x_i \cdot \gamma_i \tag{18}$$

where x_i and γ_i are the true mole fraction and the activity coefficient of species i, respectively. For the calculation of the activity coefficients, a tailor-made UNIFAC model [61] was used. The parameters needed for this were taken from Schmitz et al.[27]

The Van't Hoff equation can be used to relate the adsorption enthalpy $\Delta H_i^{\mathrm{ads}}$ of the component i with the temperature T and the adsorption constant K_i^{ads} obtained from the Langmuir model:

$$\frac{\mathrm{d} \ln K_i}{\mathrm{d}T} = \frac{\Delta H_i^{\mathrm{ads}}}{R\, T^2} \tag{19}$$

being R is the ideal gas constant.

2.3.3 Column Model

2.3.3.1 Mass and Energy Balances

The total mass balance in the liquid phase takes into account the convective transport through the column as well as the change in mass flow rate caused by adsorption and dispersion [62], resulting in the following equation:

$$
\begin{aligned}
&- \frac{\dot{m}}{A} \cdot \frac{\partial \tilde{w}_i}{\partial z} - \frac{\tilde{w}_i}{A} \cdot \frac{\partial \dot{m}}{\partial z} = \\
\epsilon \cdot \rho_{\text{liq}} \cdot \frac{\partial \tilde{w}_i}{\partial t} &+ (1-\epsilon) \cdot \rho_{\text{ads}} \cdot \frac{\partial \tilde{q}_i}{\partial t} - D_{\text{ax}} \cdot \rho_{\text{liq}} \cdot \epsilon \cdot \frac{\partial^2 \tilde{w}_i}{\partial z^2}
\end{aligned}
\tag{20}
$$

Hereby, A is the cross section area of the column, $\dot{m}$ the mass flow rate through the column, $\tilde{q}_i$ the overall adsorbent loading of component i, $\tilde{w}_i$ the overall mass fraction of component i in the liquid phase, ρ_{liq} the density of the liquid phase, ρ_{ads} the density of the zeolite 3A, D_{ax} the axial dispersion coefficient, and ϵ the bed porosity. A detailed derivation of Equation (20) is provided in the Appendix A.4.

The bed porosity ϵ is calculated as:

$$
\epsilon = \frac{V - \rho_{\text{ads}} \cdot m_{\text{ads}}}{V} \tag{21}
$$

where V, ρ_{ads}, and m_{ads} are the volume of the empty column, the density of the adsorbent and the mass of the adsorbent respectively.

The axial dispersion coefficient D_{ax} is assumed to depend solely on the mass flow rate through the column according to the equation:

$$
D_{\text{ax}} = k^{\text{disp}} \cdot \dot{m} \tag{22}
$$

which bases on the correlation presented by Butt [41, 63]. Hereby, k^{disp} is a proportionality constant to be determined by parameter fitting from experimental data.

Although adsorption is an exothermic process, a common assumption when modelling adsorptive processes in the liquid phase is to disregard the energy balance and assume an isothermal process due to the generally high heat capacities of liquids [40, 62]. In order to verify the validity of this assumption for the case considered here, the maximum possible temperature increase, i.e. the temperature increase under adiabatic conditions, was calculated for the experiment C2. The calculation method is described in detail in the Appendix A.5.

2.3.3.2 Mass Transfer of Adsorption

To describe the mass transfer of adsorption, a linear driving force (LDF) approach is employed [62]. Thereby, the mass transfer rate is linearly proportional to the difference between the equilibrium adsorbent loading and the actual adsorbent loading:

$$\frac{\partial \tilde{q}_i}{\partial t} = k_i^{\mathrm{LDF}} \ (\tilde{q}_{\mathrm{e},i} - \tilde{q}_i) \tag{23}$$

where the proportionality constants k_i^{LDF} are the overall mass transfer coefficients. In this work, the mass transfer coefficients are assumed to be constant, i.e. independent of the feed flow rate and composition.

2.3.3.3 Initial Conditions

To solve Equation (20), the initial adsorbent loadings $\tilde{q}_i(t = 0, z)$ and initial overall mass fractions $\tilde{w}_i(t = 0, z > 0)$ of the continuous phase have to be specified. Further, the column feed $\tilde{w}_i(t > 0, z = 0)$ has to be specififed at all times by its overall mass fractions $\tilde{w}_i^{\mathrm{feed}}$. In the dispersion experiments D1 and D2, the time $t = 0$ is when the column feed switches from acetone to 2-propanol. In experiments D1 and D2, no adsorption takes place. Thus, it follows:

$$\tilde{q}_i(t = 0, z) = 0 \ ; \ i = \mathrm{acetone}, 2-\mathrm{propanol} \tag{24}$$

$$\tilde{w}_{\mathrm{acetone}}(t = 0, z > 0) = 1 \ ; \ i = \mathrm{FA}, \mathrm{ME}, \mathrm{WA} \tag{25}$$

$$\tilde{w}_{\mathrm{acetone}}(t > 0, z = 0) = 0 \ ; \ i = \mathrm{FA}, \mathrm{ME}, \mathrm{WA} \tag{26}$$

In the adsorption experiments C1 to C3, the time $t = 0$ is the time the pump is turned on to feed liquid into the column. At this time, the continuous phase of the column is air. To not overcomplicate the model with the introduction of the gas phase, a simple workaround in the simulation was made:it was assumed that the column is filled with a non-adsorbing liquid, here OME_n, with chain length rations identical to the liquid feed:

$$\tilde{q}_i(t = 0, z) = 0 \;\; ; \;\; i = \mathrm{FA, ME, WA, OME_n} \tag{27}$$

$$\tilde{w}_i(t = 0, z > 0) = 0 \;\; ; \;\; i = \mathrm{FA, ME, WA} \tag{28}$$

$$\tilde{w}_i(t = 0, z > 0) = \frac{\tilde{w}_i^{\mathrm{feed}}}{\sum \tilde{w}_i^{\mathrm{feed}}} \;\; ; \;\; i = \mathrm{OME_n} \tag{29}$$

$$\tilde{w}_i(t > 0, z = 0) = \tilde{w}_i^{\mathrm{feed}} \;\; ; \;\; i = \mathrm{FA, ME, WA, OME_n} \tag{30}$$

While OME_n do not participate in adsorption or chemical reactions within the column, the chosen initial condition introduces the possibility for axial dispersion in the model as the feed gradually fills the column. This dispersion is not present in reality since the initial state of the column is air-filled. However, this deviation between the model and reality mainly impacts the behaviour of the column during the filling time, i.e., the mean residence time. As the time it takes for water to be detected at the column outlet considerably exceeds the residence time of the column, the concentration profile of water should remain mainly unaffected by this assumption. Nonetheless, this initial condition does influence the concentration profiles of formaldehyde and methanol. These compounds are minimally adsorbed and are rapidly detected at the column outlet. To account for this, the axial dispersion coefficient D_{ax} in Equation (20) was set to 0 for formaldehyde and methanol.

2.3.4 Separation Factors

The separation factors are a measure of the efficiency of an adsorptive separation between two components i and j, and are defined as [64, 65]:

$$\alpha_{i,j} = \frac{(\tilde{w}_i^{\mathrm{ads}}/\tilde{w}_j^{\mathrm{ads}})}{(\tilde{w}_i^{\mathrm{liq}}/\tilde{w}_j^{\mathrm{liq}})} \tag{31}$$

where $\tilde{w}_i^{\mathrm{ads}}$ is the overall mass fraction of compound i in the adsorbed or heavy phase, and $\tilde{w}_i^{\mathrm{liq}}$ the overall mass fraction of i in the non-adsorbed or light phase. Values of $\alpha_{i,j} > 0$ indicate a preferential adsorption of i over j. This equation is analogous to the expression for relative volatility in distillation.

In the equilibrium experiments, the overall mass fractions of component i in the heavy and light phase can be calculated by:

$$\tilde{w}_i^{\mathrm{ads}} = \frac{\tilde{q}_{\mathrm{e},i}}{\sum_i \tilde{q}_{\mathrm{e},i}} \tag{32}$$

$$\tilde{w}_i^{\mathrm{liq}} = \tilde{w}_i \tag{33}$$

In the continuous experiments, the fixed adsorption bed operates as a dynamic system, implying that $\alpha_{i,j}$ is a function of the time. The overall mass fractions of component i in the heavy and light phase at the time t can be calculated by:

$$\tilde{w}_i^{\mathrm{ads}}(t) = \frac{\tilde{q}_{i,\mathrm{col}}(t)}{\sum_i \tilde{q}_{i,\mathrm{col}}(t)} \tag{34}$$

$$\tilde{w}_i^{\mathrm{liq}}(t) = \frac{\int_0^t (\dot{m} \cdot \tilde{w}_i)\,\mathrm{d}t}{\int_0^t \dot{m}\,\mathrm{d}t} \tag{35}$$

2.3.5 Model Implementation and Parameter Estimation

The Langmuir parameters K_i^{ads} can only be reliably determined at small bulk phase concentrations. To avoid over-fitting, single-component adsorption isotherms of water from 2-propanol were measured and an activity-based Langmuir model was fitted to this data.

For both studied temperatures, $q_{m,\mathrm{ME}}$ and $q_{m,\mathrm{WA}}$ were set identical to the equilibrium loadings of pure methanol and water, respectively. $K_{\mathrm{WA}}^{\mathrm{ads}}$ was fitted to the single-component adsorption experiments of water from 2-propanol. The remaining parameters $q_{m,\mathrm{FA}}$, $K_{\mathrm{FA}}^{\mathrm{ads}}$, $K_{\mathrm{ME}}^{\mathrm{ads}}$ were adjusted simultaneously to all binary adsorption data at the respective temperature. In all fits, the following objective function was minimized:

$$\min \sum_{k=1}^{N_{\mathrm{exp}}} \sum_i \left| \tilde{q}_{\mathrm{e},ik}^{\mathrm{mod}} - \tilde{q}_{\mathrm{e},ik}^{\mathrm{exp}} \right| \quad ; \quad i \in \{\mathrm{FA}, \mathrm{ME}, \mathrm{WA}\} \tag{36}$$

Therein, N_{exp} is the number of experiments. $\tilde{q}_{\mathrm{e},ik}^{\mathrm{mod}}$ and $\tilde{q}_{\mathrm{e},ik}^{\mathrm{exp}}$ are, respectively, the modelled and experimental equilibrium loadings of component i in the experiment k. The sum of the absolute values of the residuals was chosen as objective function for the optimization,

since it tends to be less sensitive to outliers in the data [66]. For the parameter adjustment, the model was implemented in MATLAB R2019a. The optimization problem was solved with the solver *fminsearch*.

The column model was implemented in the commercial software gPROMS, where all simulations and parameter fittings were performed. The proportionality constant for the axial dispersion coefficient k^{disp} was fitted to the experimental data obtained from experiment D2 utilizing the maximum likelihood method. The overall mass transfer coefficients k_i^{LDF} were fitted to the experimental data from experiment C3, also employing the maximum likelihood method. For the sake of simplicity, it was assumed that $k_{\mathrm{FA}}^{\mathrm{LDF}} = k_{\mathrm{ME}}^{\mathrm{LDF}}$. To numerically solve the differential equations, the solver DAEBDF was utilized, making necessary the discretisation of the column into multiple axial steps. 200 steps were chosen for parameter fitting, while 50 steps sufficed for simulation purposes. The backward finite difference method (BFDM) was used as the discretisation method.

2.4 Results and Discussion

2.4.1 Density of the Adsorbent and the Liquid Solutions

The measured density of the zeolite 3A resulting from experiments Z1 - Z4 was 1.815 ± 0.010 g/cm³, where 0.010 g/cm³ is the standard deviation. The numerical results of these experiments are provided in the Appendix A.7.

Figure 4 shows the measured liquid densities of aqueous and methanolic formaldehyde solutions. For (methanol + formaldehyde), the following correlations were obtained:

$$\rho_{\mathrm{liq}}\ (22\ ^{\circ}\mathrm{C})\ /\ \mathrm{g/cm^3} = 0.4268 \cdot \tilde{w}_{\mathrm{FA}}\ /\ \mathrm{g/g} + 0.7863\ \ ;\ \ 0 \le \tilde{w}_{\mathrm{FA}} \le 0.53\ \mathrm{g/g} \tag{37}$$

$$\rho_{\mathrm{liq}}\ (40\ ^{\circ}\mathrm{C})\ /\ \mathrm{g/cm^3} = 0.4321 \cdot \tilde{w}_{\mathrm{FA}}\ /\ \mathrm{g/g} + 0.7677\ \ ;\ \ 0 \le \tilde{w}_{\mathrm{FA}} \le 0.41\ \mathrm{g/g} \tag{38}$$

The coefficients of determination are $R^2 = 0.9988$ at 22 °C and $R^2 = 0.9951$ at 40 °C.

2.4.2 Adsorption Equilibrium

2.4.2.1 Isotherm Data

The experimental and modeled adsorption isotherms of pure water from 2-propanol are shown in Figure 5. They are highly favorable for water, as the equilibrium loadings of water reaches about 80% of its maximal value for values of w_{WA} smaller than 0.005 g/g.

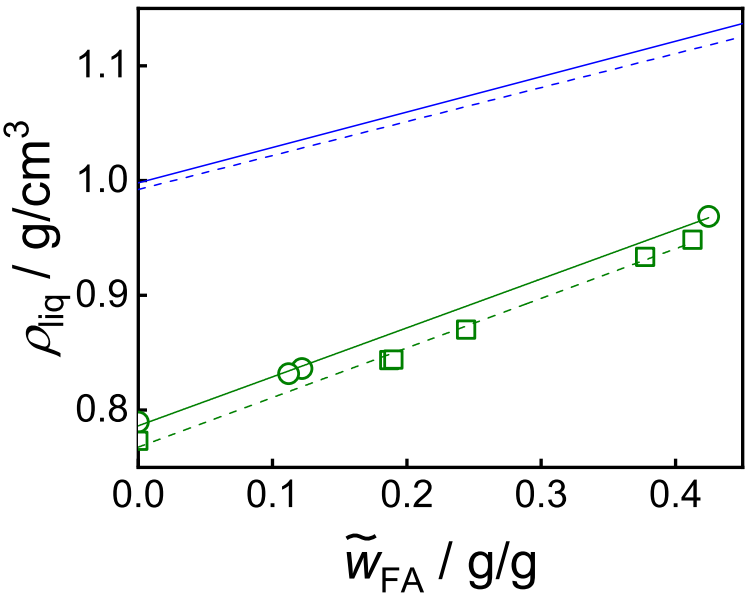

Figure 4: Densities of liquid aqueous (blue) and methanolic (green) formaldehyde solutions. Circles: Experimental data at 22 °C (this work). Squares: Experimental data at 40 °C (this work). Lines: Correlations for (formaldehyde + water) [55] and (formaldehyde + methanol) (this work) at 22 °C (solid lines) and 40 °C (dashed lines).

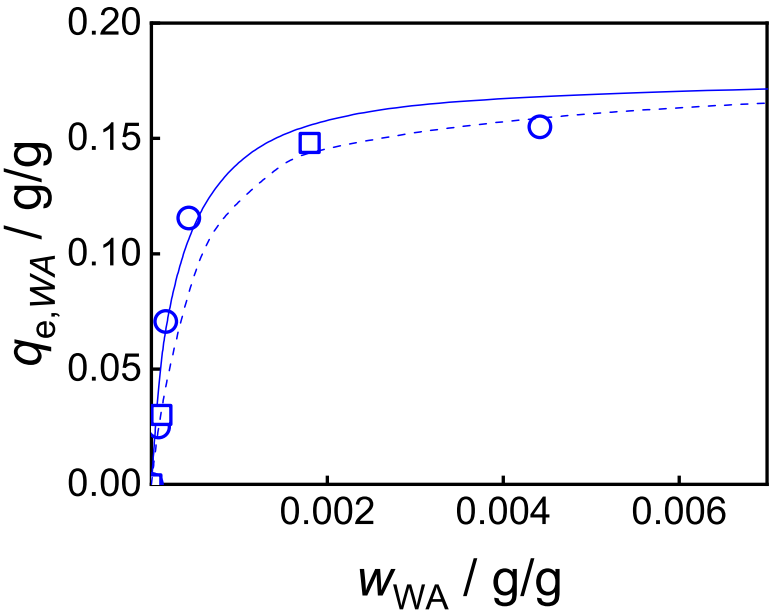

Figure 5: Adsorption isotherms of water from 2-propanol at 22 °C and 40 °C. Circles: Experimental data at 22 °C. Squares: Experimental data at 40 °C. Solid lines: Adsorption isotherm fits at 22 °C. Dashed lines: Adsorption isotherm fits at 40°C.

The experimental and modelled adsorption isotherms of the three binary mixtures at both temperatures are shown in Figure 6. The experimental uncertainties obtained via error propagation of the measurements are shown as whiskers. The procedure to determine these uncertainties is presented in the Appendix A.3. Given the large experimental uncertainties, the model is a good fit. The model parameters are tabulated in Table 5 with a 95% confidence interval.

The equilibrium loadings for pure water at 22 °C and 40 °C are 0.182 g/g and 0.181 g/g, respectively. These values are in line with some found in the literature, although a direct comparison is difficult since the experimental conditions and materials differ strongly from experiment to experiment. Teo et al. [39] report an equilibrium loading for pure water of about 0.16 g/g at 24 °C. Schmitz et al. [24] find a value of 0.166 g/g at 25° C. By measuring the adsorption of water only on the zeolite phase (i.e. not considering the less adsorbent binder material), Shukla et al. [67] and Yamamoto et al.[68] obtained higher values: 0.26 and 0.25 g/g, respectively. The manufacturer of the zeolite 3A indicates that the adsorbent equilibrium loading of pure water should be greater than 0.155 g/g at 25 °C [69].

The adsorption capacities of methanol at 22 °C and 40 °C are 0.121 and 0.120 g/g, respectively. It is not too surprising that the adsorption capacity of methanol represents about 60% of the adsorption capacity of water because of the differing molecular size. The experimental equilibrium loadings of methanol were sometimes negative at low methanol concentrations, suggesting a limitation of the method to detect very small adsorbed amounts. The estimated limit of detection of the method is 0.015 g/g. This estimation was done based on the standard deviation of blank replicates [70]. For this, the measured adsorbed amount of 2-propanol from mixtures containing water and 2-propanol were considered as blanks.

For the binary mixtures containing formaldehyde and water at 22 °C, a very pronounced, almost vertical increase in the calculated equilibrium loadings of formaldehyde was observed for $\tilde{w}_{\mathrm{FA}} \geq 0.220$ g/g. This value of $\tilde{w}_{\mathrm{FA}}$ concurs with the solubility of formaldehyde in water at 22 °C reported by Credali et al. and Breitkreuz et al. [71, 72] A similarly strong increase in the calculated equilibrium loadings of formaldehyde was observed for $\tilde{w}_{\mathrm{FA}} \geq 0.28$ g/g for the same mixtures at 40 °C, which also coincides with the solubility of formaldehyde in water at 40 °C indicated by Credali et al. and Breitkreuz et al. [71, 72] No precipitate was observed in the measuring flasks in these experiments. However, the zeolite 3A involved in these experiments could not be regenerated (i.e., they failed to adsorb formaldehyde in subsequent experiments), neither through heating (298 °C, 1 bar) nor vacuum (180 °C, 100 mbar). Therefore, it might be reasonable to assume

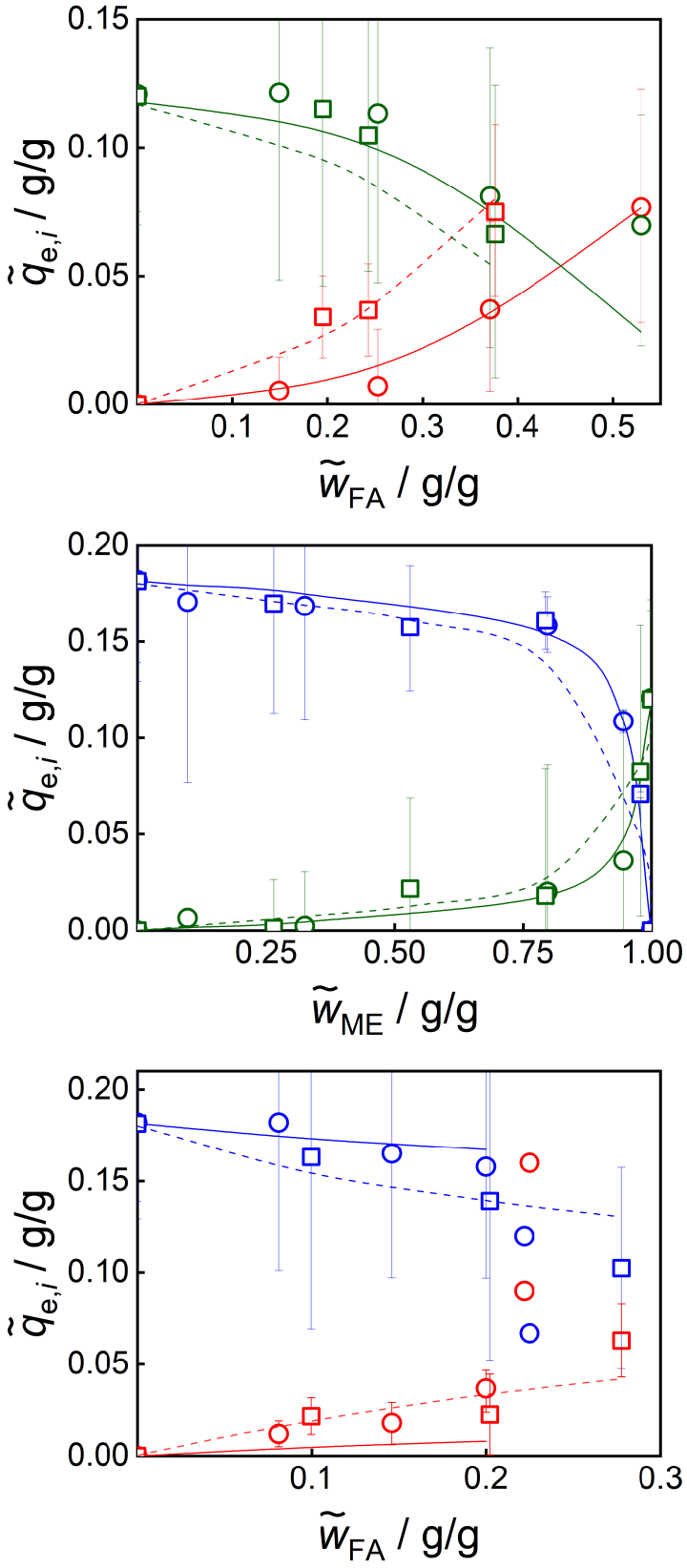

Figure 6: Adsorption isotherms of binary mixtures containing formaldehyde (red), methanol (green) and water (blue) at 22 °C and 40 °C. Circles: Experimental data at 22 °C. Squares: Experimental data at 40 °C. Solid lines: Adsorption isotherm fits at 22 °C. Dashed lines: Adsorption isotherm fits at 40°C.

that precipitation of formaldehyde from the solution in the pores of the zeolite 3A occurred in these cases. In view of these facts, adsorption on zeolite 3A could represent an alternative and faster method to determine the solubility of aqueous formaldehyde solutions.

The equilibrium loadings of formaldehyde in methanolic solutions are smaller than in aqueous solutions for a given overall mass fraction of formaldehyde in the bulk phase. This could be explained by the fact that the mole-based chemical equilibrium constant of Reaction (12) is about 40 times larger than the chemical equilibrium constant of Reaction (10) at room temperature, which means that methanolic solutions contain significantly less monomeric formaldehyde than aqueous solutions containing the same overall amount of formaldehyde [57].

2.4.2.2 Influence of Temperature

Figure 6 reveals that the influence of the temperature on the adsorption from binary mixtures (water + methanol) is relatively weak.

For the mixtures (formaldehyde + methanol) and (formaldehyde + water), the equilibrium loadings at 40°C are larger than at 22 °C. This is surprising, because physical adsorption is an exothermic process and should be enhanced at low temperatures. However, Reactions (10) – (13) are also exothermic, thus, higher temperatures increase the true concentration of monomeric formaldehyde in the liquid bulk leading to a larger driving force for adsorption.

To study this effect in more detail, Figure 7 shows the equilibrium loadings $\tilde{q}_{\mathrm{FA}}$ of formaldehyde as a function of the activity of monomeric formaldehyde in the bulk phase for the system (formaldehyde + methanol). The activities of monomeric formaldehyde were not measured directly, but calculated from the measurements of the overall mass fractions using the model of the chemical equilibrium. At 40 °C, the activities are generally larger although the overall mass fractions are similar to the experiments at 22 °C. At constant activity of monomeric formaldehyde, the adsorption is weaker at higher temperatures. This is in agreement with adsorption being an exothermic process.

It is surprising that the equilibrium loadings of formaldehyde are in the same order of magnitude as the ones of water and methanol, although the activity of monomeric formaldehyde in the liquid phase is several orders of magnitude smaller (cf. x-axis in Figure 7). This effect is also seen in the numerical values of the adsorption constants K_{FA}, which are several orders of magnitude larger than the ones of water and methanol. Although the formaldehyde molecule is slightly smaller than the water molecule, it

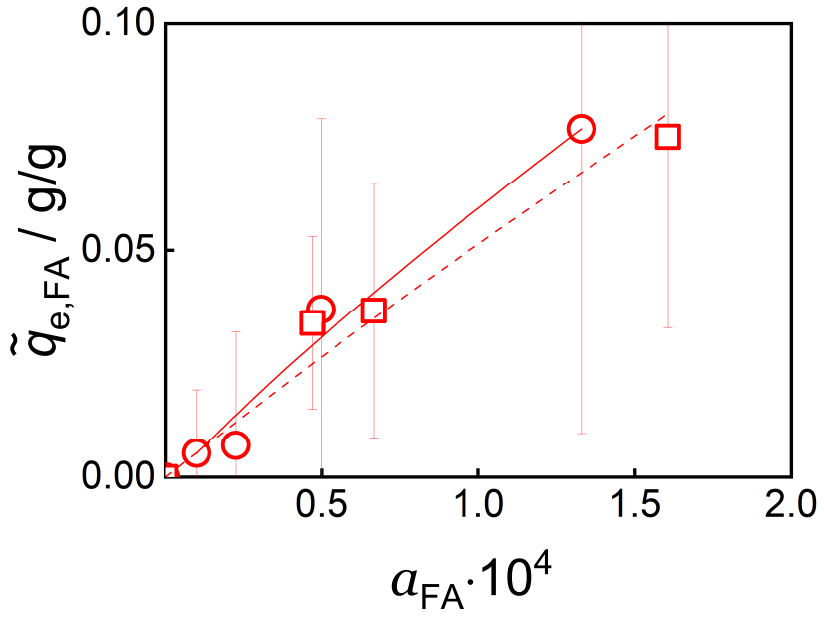

Figure 7: Adsorption isotherms of formaldehyde from binary mixtures containing formaldehyde and methanol at 22 °C and 40 °C as a function of the activity of formaldehyde. Circles: Experimental data at 22 °C. Squares: Experimental data at 40 °C. Solid lines: Adsorption isotherm fits at 22 °C. Dashed lines: Adsorption isotherm fits at 40 °C.

seems unlikely that size exclusion is responsible for such a large effect. Instead, a possible explanation is either that MG_1 and HF_1 also adsorb (their concentrations are significantly higher than the one of monomeric formaldehyde), or that formaldehyde undergoes oligomerization/polymerization after being adsorbed. The experiments of the present work are, however, not suited to evaluate the validity of the conjectures.

By integrating Equation (19) between T_1 = 295.15 and T_2 = 313.15 K and assuming constancy of ΔH_i^{ads} with the temperature within the studied temperature range, the values of ΔH_i^{ads} can be obtained from:

$$\Delta H_i^{\text{ads}} = \frac{\ln K_i(T_2) - \ln K_i(T_1)}{R\left(\frac{1}{T_1} - \frac{1}{T_2}\right)} \tag{39}$$

These values are summarized in Table 5. The adsorption enthalpy of water, -23.4 kJ/mol, agrees well with the value reported by Santos et al.[44] (-25 kJ/mol). Nevertheless, it is smaller (in absolute value) than other ones reported in the literature: -43 kJ/mol[73], -44 kJ/mol[68], -58 /kJ/mol[74]. A possible reason for these discrepancies could be related to differences of the adsorbent, especially of the binding materials [44].

$\Delta H_{\mathrm{FA}}^{\mathrm{ads}}$ and $\Delta H_{\mathrm{ME}}^{\mathrm{ads}}$ are substantially smaller than $\Delta H_{\mathrm{WA}}^{\mathrm{ads}}$. This is not surprising, since water is the most polar molecule of the system, which contributes to a stronger interaction with the solid surface. The reported values in Table 5 have a high uncertainty because they are derived from a small temperature range (ΔT = 18 K) and from considerably uncertain isotherm data.

2.4.2.3 Separation Factors

Figure 8 displays the separation factors calculated by the model as a function of the overall mass fraction in the bulk phase for the three binary mixtures studied in this work. The separation factor $\alpha_{\mathrm{WA,ME}}$ is large over the whole concentration range indicating that water can be selectively removed from methanol using zeolite 3A. The separation factor $\alpha_{\mathrm{WA,FA}}$ is closer to 1, especially at 40 °C, indicating problems to separate water selectively from aqueous formaldehyde mixtures. The separation factor $\alpha_{\mathrm{MeOH,FA}}$ is smaller than 1 for low methanol concentrations and larger than 1 for high methanol concentrations. The separation factors in all three subsystems are significantly larger at 22 °C than at 40 °C indicating a higher separation efficiency at low temperatures.

2.4.2.4 Model Validation

Through interpolation, the model predicts adsorption in the ternary system (formaldehyde + methanol + water). Predicted and experimental equilibrium loadings from ternary mixtures at 22 °C and 40 °C corresponding to the experiments B33 to B39 are compared in the parity plot in Figure 9. The agreement between predicted and measured adsorption values is good for water (smaller than 8.3% at 22°C and smaller than 11.4% at 40°C) and worse for formaldehyde and methanol, which are adsorbed considerably less and have thus a larger relative uncertainty in the experiments.

With respect to the experiments with mixtures containing OME_n, Figure 10 presents a comparison between the experimental and modelled values of $\tilde{q}_{\mathrm{e},i}$ for formaldehyde, methanol, water, OME_1, and OME_2 corresponding to the experiments B40 and B40a. The results corresponding to $\mathrm{OME}_{\geq 3}$ are not presented due to their low overall mass fraction ($\approx$ 0.02 g/g), which makes very challenging to detect any composition shift in the bulk phase due to adsorption. The experimental values of $\tilde{q}_{\mathrm{e},i}$ were determined as the arithmetic mean of the values obtained from at least two duplicates. The numeric results of these experiments including the composition of the liquid phase and the resulting equilibrium loadings are given in the Appendix. The model predicts the equilibrium loading of water and formaldehyde with reasonable accuracy. A slightly negative loading

Table 5: Adjusted parameters of the adsorption equilibrium model at 22 °C and 40 °C and adsorption enthalpies of formaldehyde, methanol and water on zeolites 3A. Data ranges correspond to 95% confidence intervals.

	$q_{\mathrm{m},i}$ / g/g		K_i^{ads}		$\Delta H_i^{\mathrm{ads}}$ / kJ/mol
	22 °C	40 °C	22 °C	40 °C	
formaldehyde	0.104 ± 0.019	0.151 ± 0.042	$(1.65 \pm 0.88) \cdot 10^5$	$(1.19 \pm 0.39) \cdot 10^5$	13.9
methanol	0.121	0.120	36.75 ± 10.02	36.09 ± 10.11	0.9
water	0.182	0.181	358.91 ± 76.30	207.46 ± 17.16	23.4

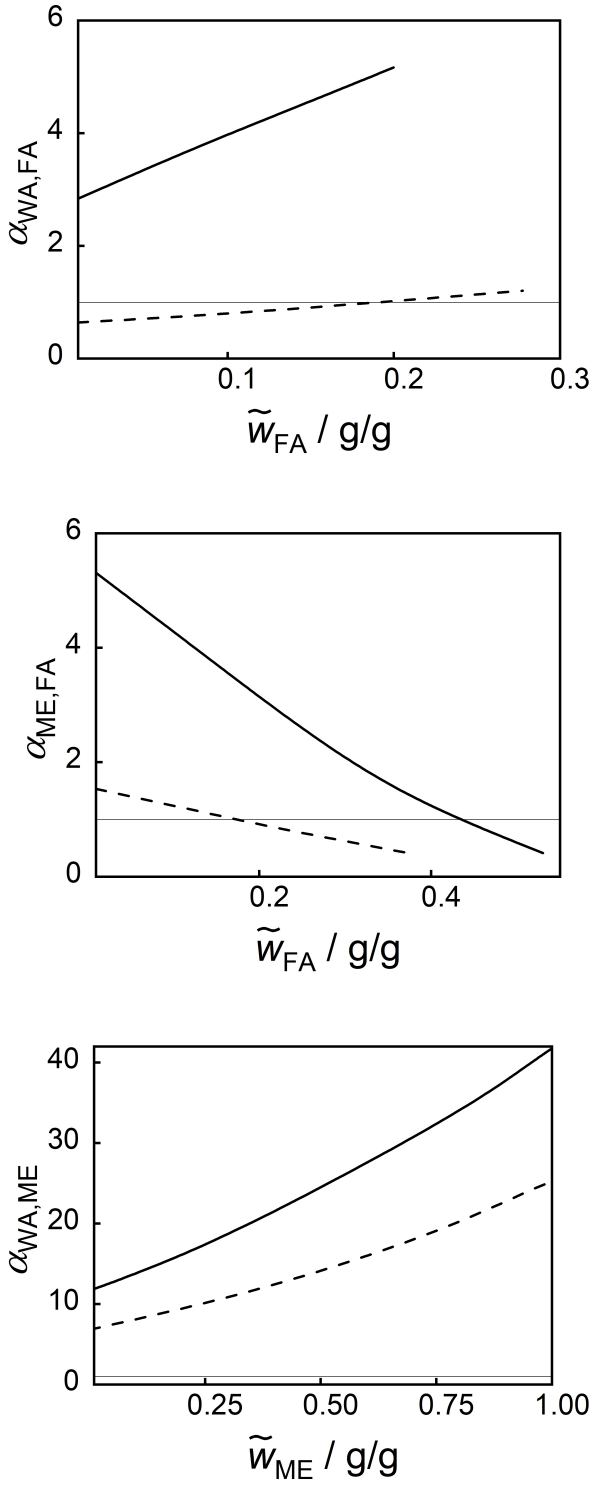

Figure 8: Estimated separation factors of the binary subsystems (formaldehyde + water), (formaldehyde + methanol) and (methanol + water) in equilibrium. Solid lines: Separation factors at 22 °C. Dashed lines: Separation factors at 40 °C.

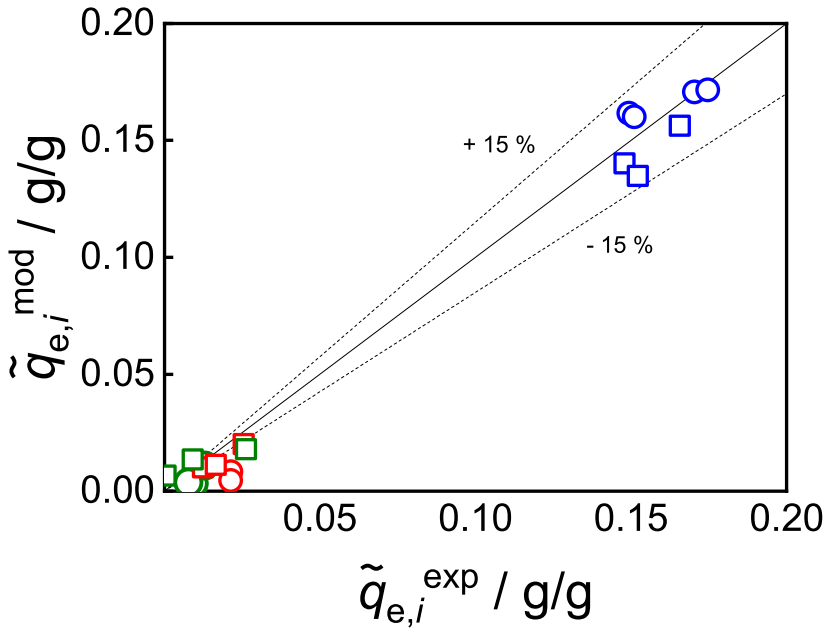

Figure 9: Predicted and experimental equilibrium loadings from ternary mixtures containing formaldehyde (red), methanol (green) and water (blue). Circles: Comparison at 22 °C. Squares: Comparison at 40 °C.

was calculated for OME_1 and OME_2, which are probably due to analytical inaccuracies. Nevertheless, the results support the assumption that there is no significant adsorption of OME_n on the zeolite 3A. On the other hand, a notably high methanol loading was measured. This discrepancy might be due to the relatively lower precision in determining the overall mass fractions of methanol, OME_1, and OME_2 compared to water and formaldehyde. Additionally, the change in the overall mass fractions of these components in the bulk phase is minimal for these components. Hence, the experimentally determined loadings of water and formaldehyde are considered to be more reliable in this context.

The equilibrium loadings of formaldehyde, methanol and water exhibited a slight decrease for the regenerated zeolite 3A (B40a) compared to the experiments with fresh adsorbent (B40), suggesting the eventual presence of a residual loading even after regeneration. Specifically, the equilibrium loading of water decreased by 8.6% when employing regenerated zeolite 3A. On the other hand, the equilibrium loading of OME_1 increased slightly when using regenerated zeolite 3A, which can possibly be attributed to its high volatility. It is conceivable that OME_1 might have evaporated from the liquid during the experiment or sample analysis, leading to its wrong interpretation as adsorbent loading [53]. Despite the inherent methodological limitations arising from the presence of numerous components, the results indicate that selective drying of mixtures containing

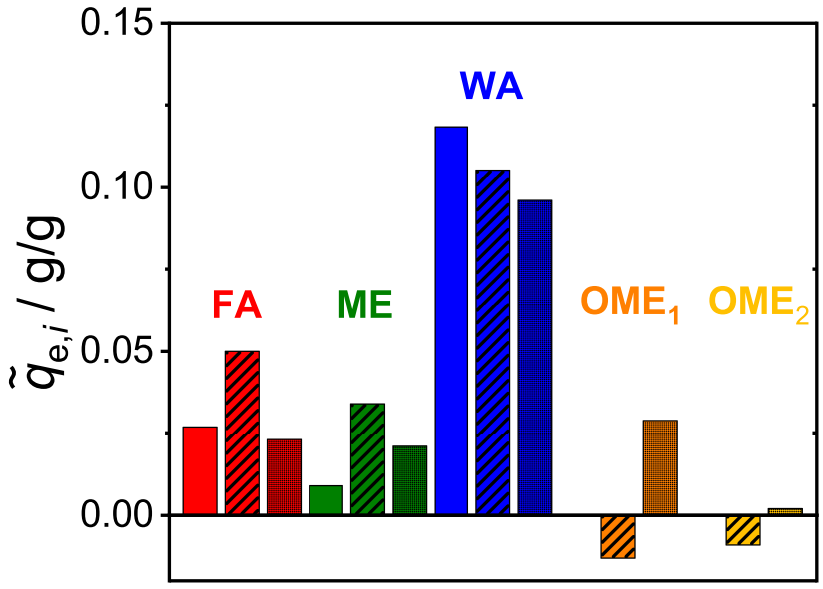

Figure 10: Experimental and modelled equilibrium loadings of formaldehyde (red), methanol (green), water (blue), OME_1 (orange) and OME_2 (yellow). Filled bars: Model corresponding to experiment B40. Dashed bars: Experiment B40. Dotted bars: Experiment B40a.

formaldehyde, methanol, water and OME_n using zeolite 3A is feasible. Moreover, the equilibrium model shows promising capability in predicting the overall loadings of all components within the system.

2.4.3 Continuous Experiments

2.4.3.1 Dispersion Experiments

Figure 11 shows the results of the dispersion experiments D1 and D2. By observing the gentle slope of the concentration profiles at the column outlet, it becomes evident that dispersion effects within the column are of significance since acetone and 2-propanol exhibit no adsorption onto zeolite 3A.

The value of the constant k^{disp} obtained through fitting the data from experiment D2 leads to an axial dispersion coefficient value of $6.8 \cdot 10^{-5}$ m^2/s for the experiment D2, which is in a typical range for axial dispersion coefficients in fixed beds [41]. The strong agreement observed between the experimental and modelled data for experiment D1 further validates the approach employed in linear scaling of the axial dispersion coefficient with the flow rate (cf. Equation (22)).

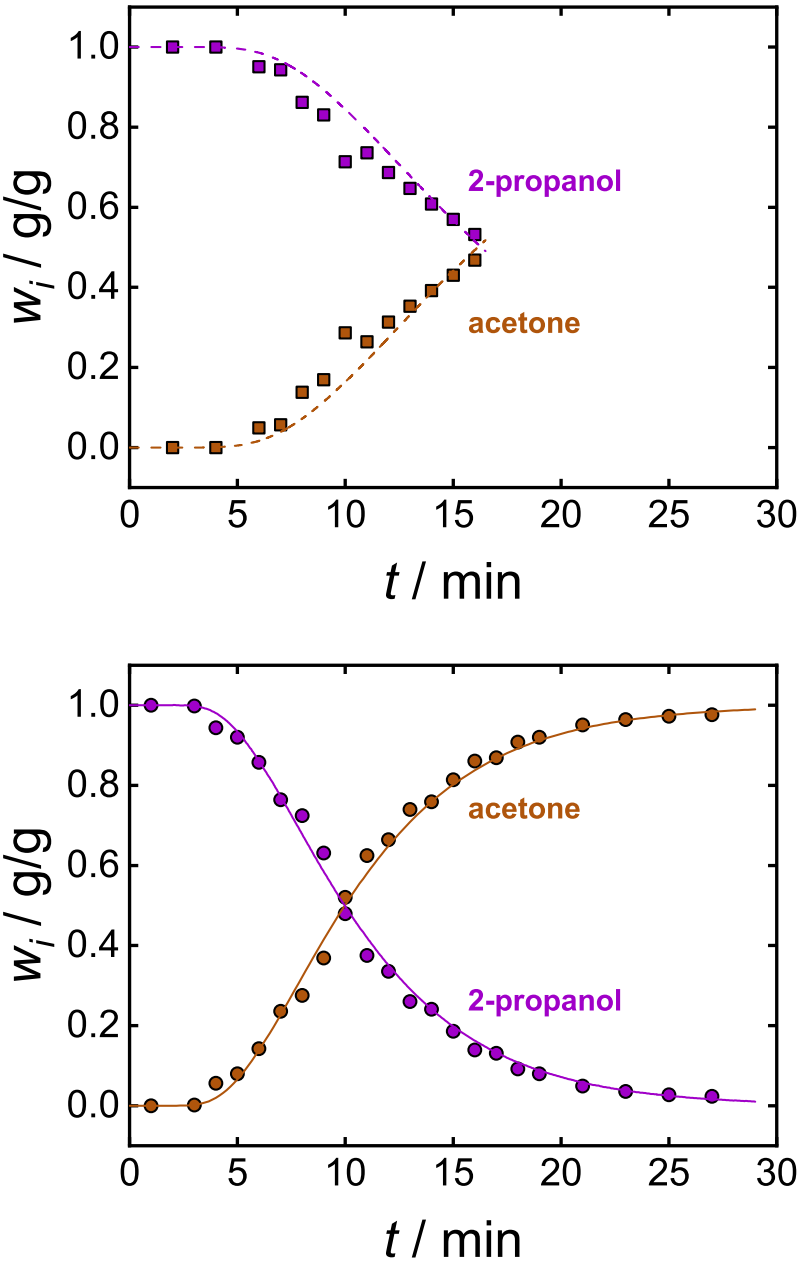

Figure 11: Mass fraction profiles at the column outlet for the experiments D1 (top) and D2 (bottom).

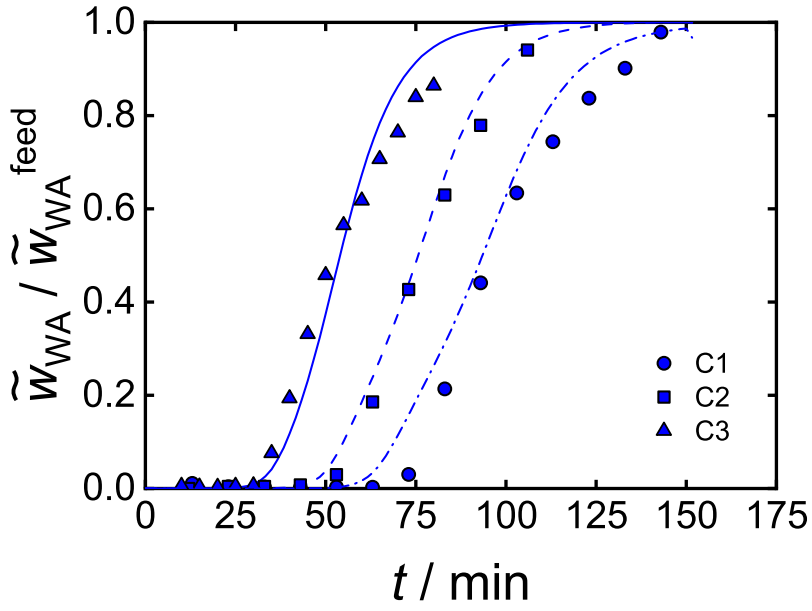

Figure 12: Experimental and modelled breakthrough curves of water for the experiments C1, C2 and C3. Markers: Experimental data. Lines: Model.

2.4.3.2 Adsorption Experiments

Figure 12 displays the breakthrough curves for water corresponding to experiments C1, C2, and C3. These curves have been normalized with respect to the feed composition to facilitate a direct comparison among the three experiments, despite slight variations in the overall mass fraction of water in the feed. The close alignment between the plotted lines and the experimental data points underscores the ability of the model to accurately predict the overall water mass fraction at the column outlet for all three experiments. The robust agreement between the model and experimental results supports the assumption that the mass transfer coefficient $k_{\mathrm{WA}}^{\mathrm{LDF}}$ is independent of the feed flow rate in the studied range. This finding is consistent with the results of Ambrożek et al. [41], who showed that the mass transfer coefficient of water $k_{\mathrm{WA}}^{\mathrm{LDF}}$ remains practically unchanged across different flow rates in the adsorptive drying of 1-propanol.

Figure 13 presents the breakthrough curves for formaldehyde and methanol corresponding to experiment C2. For the sake of clarity, the results corresponding to only one representative experiment are shown; similar plots for experiments C1 and C3 are given in the Appendix A.12. The model also predicts the breakthrough curves of formaldehyde and methanol with reasonable accuracy. The mean residence times for experiments C1, C2, and C3 are 13, 12, and 10 min, respectively. By comparing the breakthrough times

for formaldehyde and methanol with the residence times for experiments C1 to C3, it becomes clear that the adsorption of formaldehyde and methanol is significantly smaller than the adsorption of water.

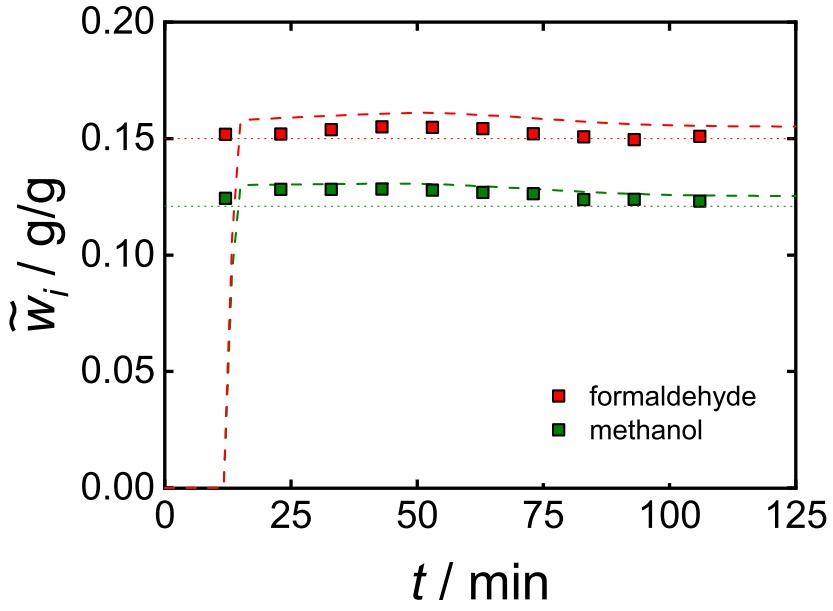

Figure 13: Experimental and modelled breakthrough curves of formaldehyde (red) and methanol (green) for the experiment C2. Markers: Experimental data. Dashed lines: Model. Dotted lines: Feed composition.

The fitted values of the mass transfer coefficients are $k_{\mathrm{WA}}^{\mathrm{LDF}} = 3.7 \cdot 10^{-3}$ s^{-1} and $k_{\mathrm{FA}}^{\mathrm{LDF}} = k_{\mathrm{ME}}^{\mathrm{LDF}} = 1.0 \cdot 10^{-4}$ s^{-1}. The reported values of $k_{\mathrm{WA}}^{\mathrm{LDF}}$ in the literature can vary significantly depending on the specific chemical system. For instance, Ambrożek et al.[41] reported values ranging from $4.0 \cdot 10^{-3}$ s^{-1} to $4.7 \cdot 10^{-2}$ s^{-1} for the adsorption of water from 1-propanol on zeolite 3A and 4A, respectively, at 303 K. Burrichter et al.[37] reported values ranging from $3.7 \cdot 10^{-4}$ s^{-1} to $4.8 \cdot 10^{-5}$ s^{-1} for the adsorption of water from different alcohols on zeolite 3A at 298 K, depending on the alcohol involved. Joshi et al. [34] reported values ranging from $1.5 \cdot 10^{-2}$ s^{-1} to $5.5 \cdot 10^{-2}$ s^{-1} for the adsorption of water from toluene on zeolite 3A and 4A. No comparison values were found in the literature for formaldehyde and methanol.

Table 6 presents the modelled mass fractions of the adsorbed phase $\tilde{w}_i^{\mathrm{a}}$ for experiments C1, C2 and C3 at t = 150 min. Afterwards, these values do not change anymore as the adsorbent is saturated. The adsorbed phase exhibits a significant overall mass fraction of water, 0.886 g/g on average. The average separation factors for formaldehyde and methanol over the experiments C1 to C3 are $\alpha_{\mathrm{WA,FA}} = 67.95$ and $\alpha_{\mathrm{WA,ME}} = 214.76$.

These values underscore the remarkable potential of adsorption as a promising method for tackling this challenging separation task.

Table 6: Modelled overall mass fractions of the adsorbed phase for the experiments C1, C2 and C3 at t = 150 min.

	$\tilde{w}^{\text{ads}}_{\text{WA}}$	$\tilde{w}^{\text{ads}}_{\text{FA}}$	$\tilde{w}^{\text{ads}}_{\text{ME}}$
C1	0.874	0.103	0.024
C2	0.877	0.094	0.029
C3	0.908	0.075	0.017

In terms of the adiabatic temperature increase, the calculations yielded a value of 16 °C. In practical applications, however, this temperature rise occurs only in the part of the column where adsorption is actively taking place [62]. Subsequently, this region is cooled by the subsequent feed stream. Furthermore, the real operation is not adiabatic. Comparing the equilibrium water for water at 40 °C, cf. Equation (16), with that at 22 °C for experiments C1 and C3, a difference of less than 10% is observed. Hence, even if the column temperature were to reach 40 °C, its impact on process performance would be minimal.

Regarding the potential for regeneration of the zeolite 3A, Figure 14 presents the experimental breakthrough curves for water adsorption in experiments C2, C2a, C2b, and C2c. A subtle reduction in adsorption capacity becomes evident, as the breakthrough curves of experiments C2a, C2b, and C2c exhibit a slight shift to the left compared to the curve corresponding to experiment C2. However, the shift of the curves to the left does not consistently increase with repeated number of regenerations (the curve corresponding to experiment C2c is not left of the curve corresponding to experiment C2b).

The experimental equilibrium loadings of water for experiments C2a, C2b, and C2c at t = 105 min are 0.144 g/g, 0.139 g/g, and 0.149 g/g, respectively, whereas the equilibrium loading of water for experiment C2 is 0.166 g/g. This discrepancy signifies an average loss of adsorption capacity of roughly 13% when compared to the fresh zeolite 3A. Regarding formaldehyde and methanol, the experimental equilibrium loadings at t = 105 min for the experiments C2, C2a, C2b, and C2c exhibit slight variations, but no systematic decrease is observed in the experiments employing regenerated zeolite 3A when compared to experiment C2.

In a related study, Gabruś et al. [75] conducted continuous fixed bed desorption experiments on 3A zeolite 3A previously used for ethanol and 1-butanol dewatering. In

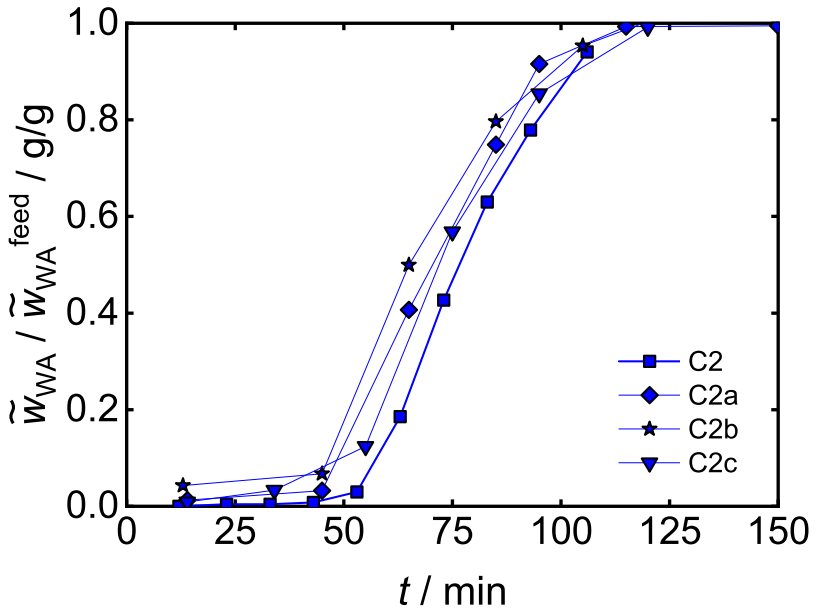

Figure 14: Experimental breakthrough curves of water for the experiments C2, C2a, C2b and C2c. Note that the lines are only straight connections between the experimental data points to facilitate the identification of the curves and and do not represent the model.

their regeneration process, the authors employed a hot air stream at 250 °C with air mass fluxes ranging from 0.27 to 0.31 kg /(m² s) over durations spanning from 176 to 360 minutes. Their results indicated a decrease in adsorption capacity of approximately 30% after multiple regeneration cycles compared to the fresh adsorbent.

The variations observed between the experiments of this work and those of Gabruś et al.[75] might be attributed to differences in desorption times. This could suggest that the slow kinetics associated with water desorption might limit the full regeneration of the zeolite 3A. An integration of the regeneration step in the OME_{3-5} process of Schmitz et al. [24] with hot air or another inert gas as done by Gabruś et al.[75] would be conceivable. To achieve continuous operation, multiple adsorber beds in parallel are necessary [62]. However, the energy consumption for the regeneration step in other industrial zeolite-based temperature swing adsorption processes in the liquid phase is significant (around 12000 kJ/kg water [62]). Further research should focus on exploring alternative desorption processes such as extraction-based methods, that could represent a more economically viable option.

3 Water Separation via Pervaporation

3.1 Introduction

Over the past few decades, pervaporation has emerged as an economical, safe, and environmentally friendly alternative to traditional processes for numerous applications, such as the dehydration of organics, among others [76, 77].

The dehydration of alcohols using membrane-based techniques has been extensively studied in the literature. For instance, Jiraratananon et al. [78] conducted dehydration experiments on chitosan/hydroxyethylcellulose composite membranes, focusing on the system (ethanol + water). They reported water fluxes ranging from 0.3 to 0.4 kg/(m^2 h) for water concentrations around 0.05 g/g in the feed at 60 °C. Castro-Muñoz et al. [79] investigated the system (ethanol + water) using polyvinyl alcohol (PVA)/graphene membranes and reported water fluxes below 0.15 kg/(m^2 h). Magalad et al. [80] studied PVA/polyvinyl pyrrolidone mixed matrix blend membranes for the system (ethanol + water). They found that incorporating 0.04 g/g of phosphomolybdic acid particles into the blend matrix of the membranes enhanced the pervaporation performance.

While PVA membranes are a promising option for dehydrating certain solvents like ethanol and higher alcohols, they may not be suitable for separating polar systems such as (methanol + water) or systems containing corrosive solvents [81]. In such cases, zeolite membranes present a compelling alternative solution. For example, Carretier et al. [77] investigated the separation of water from the system (methanol + water + OME_1) using three different PVA membranes and a zeolite membrane. They found that the PVA membranes were unsuitable due to degradation and weak permeate flows. The zeolite membrane, on the other hand, exhibited water fluxes between 0.3 and 0.35 kg/(m^2 h) for water concentrations around 0.05 g/g in the feed and very good selectivity towards water. The authors noted that the zeolite membranes showed no signs of degradation after multiple experiments. In a recent publication, Unlu [82] focused on the purification of OME_1 from mixtures containing (OME_1 + methanol) using a PVA/polyvinyl pyrrolidone

blend membrane. The authors reported methanol fluxes of approximately 0.45 kg/(m² h) for methanol concentrations around 0.1 g/g in the feed. The membrane remained stable after ten runs, indicating the potential beneficial effect of poly vinyl pyrrolidone on membrane stability. Shah et al. [81] conducted experiments on a zeolite NaA membrane in various systems, including (methanol + water), (ethanol + water), (isopropanol + water), and (dimethylformamide + water). In the system (methanol + water), they reported water fluxes around 0.6 kg/(m² h) for water concentrations around 0.1 g/g in the feed at 60 °C.

For systems containing $OME_{>1}$, the only study, to the best of author's knowledge, is the work of Schmitz et al. [32]. They performed pervaporation experiments on water separation from liquid mixtures containing (formaldehyde + methanol + water + OME_n) using two zeolite membranes (type NaA and type T) and three PVA membranes. The authors found the zeolite NaA membrane to be unstable in repeated measurements and observed low water fluxes for the zeolite T membrane. They mentioned that the PVA membranes exhibited favourable selectivity towards water and considerable water fluxes, and their performance did not deteriorate after one repeated measurement. However, the long-term stability of the PVA membranes remains uncertain since no further repetitions were conducted. Considering the findings reported by Carretier et al. [77] and Shah et al. [81], it seems less likely that PVA membranes would remain stable in systems containing methanol, formaldehyde, and OME.

In this chapter, this gap is tackled by systematically performing repeated pervaporation experiments within the system (formaldehyde + methanol + water + OME_n) in an experimental setup provided by DBI Gas- und Umwelttechnik. This setup was integrated in a mini-plant for OME_{3-5} production erected in the technology laboratory of the Technical University of Munich, with a nominal capacity of 1 kg/h (=8 tonnes/a). Further details about the mini-plant are given in Chapter 4. A model to characterize the water flux as a function of the overall mass fraction of water in the pervaporation unit is introduced. The selectivity and the stability of the membrane are discussed. Lastly, alternatives for further enhancing the water content of the permeate stream are discussed.

3.2 Experimental Methodology

3.2.1 Chemicals, Analytics and Membranes

Paraformaldehyde (>0.895 g/g) and methylal (>0.997 g/g) were purchased from Prefere and methanol (>0.998 g/g) was purchased from VWR. Ultra-pure water was obtained from a PURELAB Classic water purification system from ELGA.

The overall mass fractions of each component and the catalyst activity were determined according to the procedures described in Section 2.2.3.

A inorganic and hydrophilic SiO_2 membrane manufactured by the Fraunhofer Institute for Ceramic Technologies and Systems (IKTS), Hermsdorf, Germany, was used. The membranes had four channels, with a length of 1201 mm, an outer diameter of 21 mm, and an inner diameter of 6 mm. The basis is a porous ceramic support layer made of aluminium oxide (Al_2O_3), on which the active separating layer is situated. At both ends of the membranes, a glazing layer of 15 mm is present to seal the end faces. Table 7 presents a summary of some membrane properties as provided by the manufacturer. Furthermore, characterization studies including SEM imaging, XRD, and water contact-angle test of the membrane have been performed. Detailed information on these characterizations can be found in the Appendix B.

Table 7: Physical properties of the membranes.

active layer	SiO_2
d50 / mm	1
BET surface / m^2/g	400
layer thickness / nm	50
crystallinity	amorphous

3.2.2 Pervaporation Setup

The P&ID diagram of the mini-plant pervaporation setup is shown in Figure 15. The pervaporation unit is operated batch-wise. The feed mixture, from which water is to be removed, is placed in the feed tank B1. The feed pump P1 (AN, Cemp) pushes the feed mixture from the feed tank B1 towards the loop pump P2 (IE3, KSB). A throttle valve enables a reduction of the flow rate back into B1. The residual flow is circulated through the membrane modules M1 and M2 by means of the loop pump P2. Each of

the two modules M1 and M2 can hold up to four membranes, with a maximum flow rate of 8000 l/h (4000 l/h per module). The experiments in this study involved varying the total number of membranes used, ranging from 2 to 8. In cases where one or more channels were not utilized, stainless steel tubes of similar geometry were placed into the remaining channels, or one entire module was excluded by closing the corresponding valves. Vacuum is generated in the permeate side by the diaphragm pump P3 (MPC, Ilmvac). The temperature of the feed mixture can be adjusted by the electric heater TH1.

The evaporated permeate is transferred from the vacuum chamber of the modules to a two-stages condenser W1 and W2, where the permeate is condensed. Both condensers are cooled by means of the external recirculating chiller TH2 (FP50, Julabo). A mixture of water and ethylene glycol in a ratio of approximately 1:1 with a temperature of 2 °C is used as coolant. A touch control panel (Simatic HMI, Siemens) allows control of the entire plant by means of automatic or manual operation. During the experiment, the condensate is collected in the intermediate tanks B2 and B3. At the end of the experiment, B2 and B3 are emptied into the tanks B4 and B5, while the dewatered feed remains in the feed tank B1.

3.2.3 Experimental Plan

A total of 14 experiments (M1 - M14, as listed in Table 8) were conducted using the SiO_2 membranes in the mini-plant setup. Table 8 provides a summary of the experimental conditions, including the materials used, the permeate-side absolute pressure (p), the temperature (T), the initial overall mass fraction of water in the feed ($\tilde{w}_{\mathrm{WA}}^{\mathrm{feed}}$), and the number of membranes. The full composition of the feed mixtures in the experiments is given in the Appendix B. All of these experiments were carried out at 50 °C. Experiments M6 to M11 were specifically performed in the vicinity of the operating point defined in the water-tolerant OME_{3-5} production process described by Schmitz et al. [24].

It is important to note that in the mini-plant experiments, once the membranes were installed in the setup, they were not changed or replaced. Therefore, all experiments can be considered as repetitions, providing valuable data for analysis and comparison.

3.2.4 Preparation of Feed Mixtures

The feed for experiments M1 - M5 and M12 - M14 was prepared by mixing methanol, paraformaldehyde, ultra-pure water, OME_1, and/or $OME_{>1}$ in appropriate proportions.

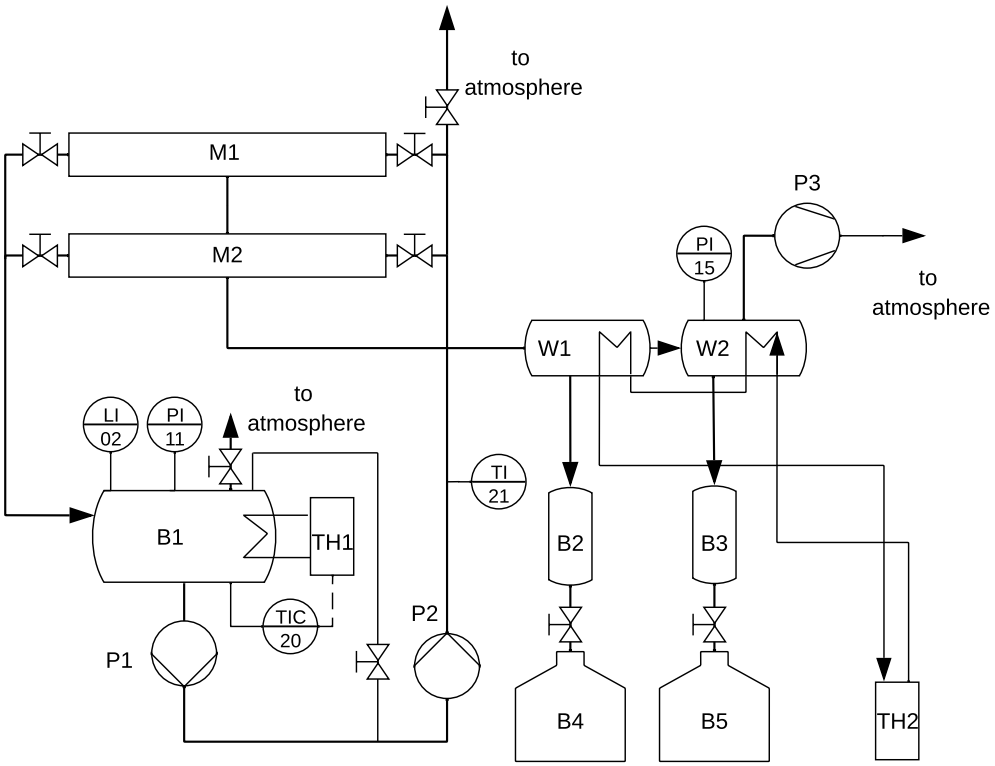

Figure 15: P&ID diagram of the pervaporation setup.

Table 8: Overview of the experiments performed in the pervaporation setup.

experiment	material	p / mbara	T / °C	$\tilde{w}_{\mathrm{WA}}^{\mathrm{feed}}$ / g/g	number of membranes
M1	SiO_2	80	50	0.088	2
M2	SiO_2	80	50	0.099	4
M3	SiO_2	80	50	0.070	4
M4	SiO_2	80	50	0.036	6
M5	SiO_2	80	50	0.036	6
M6	SiO_2	80	50	0.051	8
M7	SiO_2	80	50	0.047	4
M8	SiO_2	80	50	0.053	8
M9	SiO_2	80	50	0.049	8
M10	SiO_2	80	50	0.048	8
M11	SiO_2	80	50	0.046	8
M12	SiO_2	80	50	0.450	8
M13	SiO_2	80	50	0.428	8
M14	SiO_2	80	50	0.369	8

The feed for experiments M6 - M11 was obtained from the distillation column of the OME_{3-5} mini-plant (cf. Chapter 4, Runs 1 - 6). Prior to usage, the composition of the feed was determined by chemical analysis.

3.2.5 Procedure

The membranes undergo preliminary testing with water and process mixtures prior to conducting the experiments to ensure the proper functioning of the mini-plant setup. During each experiment, the feed tank B1 is filled with the feed mixture. The feed pump P1 is initially set to 30% power while the system is ventilated to remove any trapped air. Once a low but continuous return flow to tank B1 is achieved, the loop pump P2 is started with 30% power, which corresponds to a flow rate of around 2500 l/h. The temperature is then set and monitored closely. Once the desired temperature is reached, the vacuum pump is activated, establishing a vacuum of approximately 80 mbara on the permeate side of the membrane module. The setup is then set to automatic mode, ensuring that the temperature in the feed tank and the volumetric flow rate through the membrane modules remain constant. The volumetric flow rate is kept at either 8000 l/h (when operating with both membrane modules, M1 and M2) or 4000 l/h (if operating only with one membrane module). Regularly, samples are taken from the feed and

analysed. The experiment is stopped after a specific duration or when a certain water concentration in the feed is reached. The entire system is vented, and both permeate and feed tanks are emptied.

In all performed experiments, the total flux J was determined by weighing the mass of permeate m^{permeate} collected over the experiment duration Δt divided by the membrane area A_{membrane}:

$$J = \frac{m^{\text{permeate}}}{A_{\text{membrane}} \cdot \Delta t} \tag{40}$$

The overall flux of water $\tilde{J}_{\text{WA}}$ was determined from the total flux J and the overall mass fraction of water in the permeate $\tilde{w}_{\text{WA}}^{\text{permeate}}$:

$$\tilde{J}_{\text{WA}} = J \cdot \tilde{w}_{\text{WA}}^{\text{permeate}} \tag{41}$$

3.3 Modelling Methodology

3.3.1 Chemical Reactions

The model to describe the Reactions (10) – (13) is the same than in the Section 2.3.1.

3.3.2 Pervaporation Model

The component and total mass balances in the pervaporation unit for the experiments M1 to M14 are:

$$\frac{1}{A_{\text{membrane}}} \frac{\mathrm{d}(m \cdot \tilde{w}_{\text{WA}})}{\mathrm{d}t} = -\tilde{J}_{\text{WA}} \tag{42}$$

$$\frac{1}{A_{\text{membrane}}} \frac{\mathrm{d}m}{\mathrm{d}t} = -J \tag{43}$$

being m the mass of liquid in the pervaporation unit and $\tilde{w}_{\text{WA}}$ the overall mass fraction of water in the tank B1 at a given time.

The dependency of the overall fluxes of water $\tilde{J}_{\text{WA}}$ on the overall mass fraction of water in the tank B1 was correlated by the empirical equation [32]:

$$\tilde{J}_{\mathrm{WA}} \;/\; \frac{\mathrm{kg}}{\mathrm{h\ m^2}} = a \;\cdot\; \left(1 - e^{-b \,\cdot\, \tilde{w}_{\mathrm{WA}} \;/\; \mathrm{g/g}}\right) \tag{44}$$

where a and b are parameters to be fitted to the experimental data of experiments M1 to M14.

To include the total flux in the model and to solve the mass balances, a correlation between $\tilde{w}_{\mathrm{WA}}^{\mathrm{permeate}}$ and $\tilde{w}_{\mathrm{WA}}$ is needed. To keep the model simple and to avoid overfitting, the overall mass fraction of water in the permeate was assumed to be independent of the overall mass fraction of water in the tank B1 and equal to the average value of $\tilde{w}_{\mathrm{WA}}^{\mathrm{permeate}}$ over the experiments M1 to M14.

The parameters a and b from Equation (44) were fitted by minimizing the following objective functions in MATLAB R2019a with the solver *fminsearch*:

$$\min \sum_{k=\mathrm{M1}}^{\mathrm{M14}} \left(\tilde{J}_{\mathrm{WA},k}^{\mathrm{mod}} - \tilde{J}_{\mathrm{WA},k}^{\mathrm{exp}}\right)^2 \tag{45}$$

Once the parameters a and b were fitted, Equations (42) to (44) were solved numerically in MATLAB R2019a with the solver *ode45*. The initial conditions were:

$$\tilde{w}_{\mathrm{WA}}(t = 0) = \tilde{w}_{\mathrm{WA}}^{\mathrm{feed}}$$

$$m(t = 0) = m^{\mathrm{feed}}$$

where $\tilde{w}_{\mathrm{WA}}^{\mathrm{feed}}$ and m^{feed} are the initial overall mass fraction of water in the tank B1 and mass of feed, respectively.

3.3.3 Condensation Model

The condensation of the permeate in the mini-plant occurs in two stages and is modelled using an equilibrium stage approach, which takes into account the Reactions (10) – (13). It is assumed that both chemical equilibrium and vapour-liquid equilibrium are established at each stage. The model for vapour-liquid equilibrium is adopted from the work by Schmitz et al. [27], and details can be found there. To perform the simulations, the commercial process simulator Aspen Plus V8.8 was used. The pressure, inlet mass flow rate, composition, and masses of condensate in each stage were specified to the experimentally determined values as inputs for the simulations.

3.4 Results and Discussion

3.4.1 Experiments

For experiments M1 - M14, the relative error in the total mass balance was in average 1.6%. The relative errors in the mass balances of the individual components are in the same order of magnitude. Detailed stream tables of all performed experiments are provided in the Appendix B.

Figure 16 illustrates both the experimental and modelled overall fluxes of water through the membrane, along with the overall mass fractions of water in the permeate, plotted against the overall concentration of water in the tank B1. To account for the varying overall mass fraction of water in the tank B1 during an experiment, the average value is used to represent the results.

The adjusted values of the coefficients a and b are 1.195 kg h m^2 and 7.889 g/g, respectively. The overall flux of water increases with increasing concentrations of water. The fitted curve provides a reasonably good description of the experimental data, yielding a coefficient of determination R^2 of 0.948.

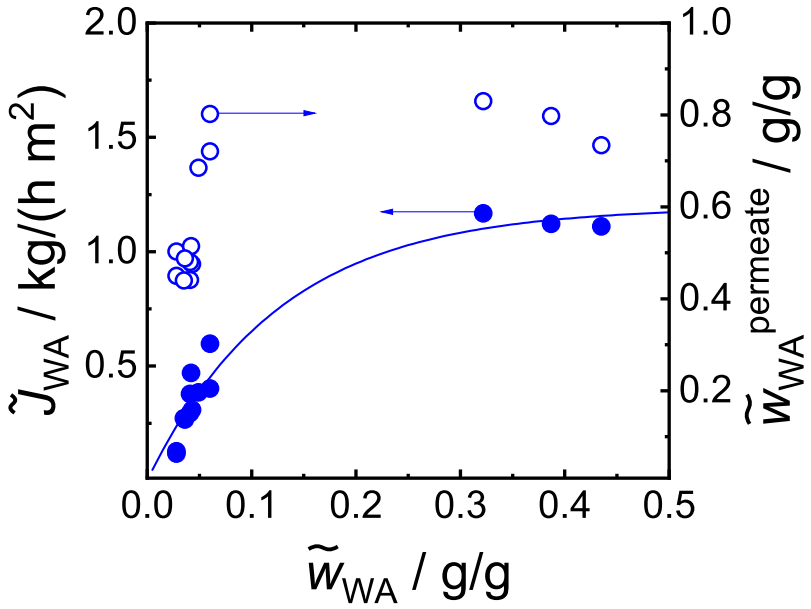

Figure 16: Overall fluxes of water (filled symbols) and overall mass fractions of water in the permeate (empty symbols) as a function of the overall mass fraction of water corresponding to the experiments M1 - M14 in the mini-plant setup with a SiO_2 membrane.

The overall concentration of water in the permeate initially increases with the water concentration in the tank B1, reaching an upper limit at about 0.8 g/g. The data exhibits a considerable dispersion that can be related to small variations in the operating conditions (permeate-side pressure, temperature) across the experiments, inhomogeneities between the membranes, and inconstancy of the overall mass fraction of water in the permeate over time. Around the operating point of the water tolerant $OME_{3–5}$ process, i.e., at an overall mass fraction of water of roughly 0.05 g/g, the overall mass fraction of water in the permeate varied between 0.441 g/g and 0.515 g/g.

Upon comparing the results obtained here (i.e., from the mini-plant experiments) with those from the membrane screening [33], it becomes evident that the overall fluxes of water and the overall mass fractions of water in the permeate are much lower in the mini-plant experiments compared to the screening experiments. The variation in the fluxes can be reasonably attributed to the distinct permeate-side pressures employed: 15 mbar for the screening experiments and 80 mbar for the mini-plant experiments. The higher pressure used in the mini-plant experiments likely contributed to the observed decrease in flux, as it results in a smaller driving force for the pervaporation process.

The exact cause of the discrepancy in the overall mass fraction of water in the permeate between the two sets of experiments remains elusive. It seems unlikely that the selectivity deteriorates over time due to structural damage to the membranes, as significant concentrations of formaldehyde, methanol, OME_1, and OME_2 were detected already in the first (preliminary) experiments conducted with the membranes in the mini-plant setup. Furthermore, the permeate purity remained consistent across experiments M6 - M11, which were performed under the same conditions. One plausible explanation could be the presence of structural differences among the membranes used for the screening experiments and those employed in the mini-plant experiments, which could be a consequence of upscaling of the membrane synthesis process. These differences might influence the selectivity of the membranes, leading to variations in the permeate composition. To comprehensively understand the underlying factors contributing to the differences in permeate quality, further investigations are desired.

By combining and numerically integrating Equations (42) to (44), it is possible to simulate the concentration profiles in the tank B1 during an experiment. To illustrate this, Figure 17 shows the evolution of the overall mass fraction of water in the tank B1 with the time for three experiments, namely experiments M1, M7 and M12. Similar plots for the other experiments can be found in the Appendix B.4. The agreement between the experimental data and the simulation is astonishingly good, attesting that the model for the water flux is sufficient to characterize the membrane operation.

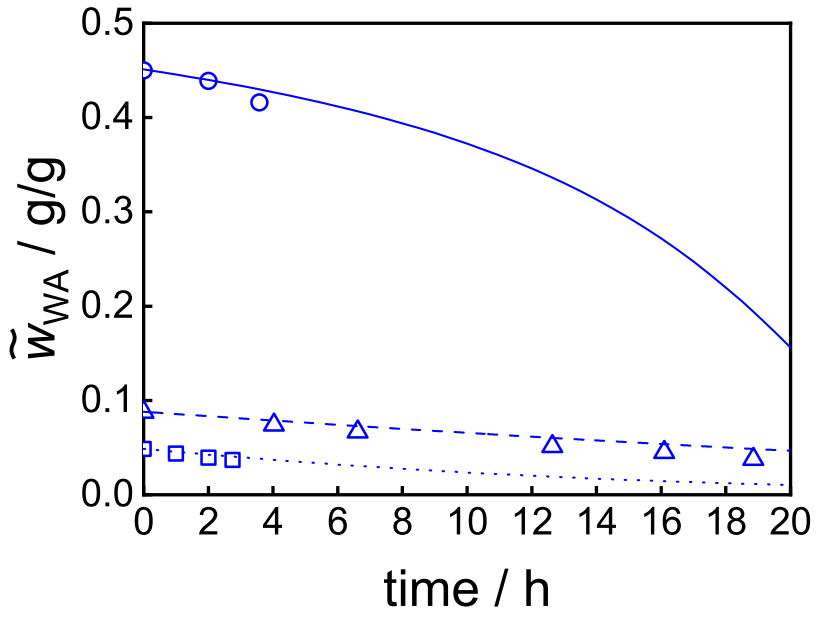

Figure 17: Evolution of the overall mass fraction of water for Experiments M1, M7 and M12. Symbols: Experimental data (triangles: Experiment M1, squares: Experiment M7, circles: Experiment M12). Lines: Model.

The selectivity of a pervaporation-based separation of two components i and j can be quantitatively characterized by the separation factor, defined as: [78]

$$\alpha_{i,j} = \frac{(\tilde{w}_i^{\text{permeate}} / \tilde{w}_j^{\text{permeate}})}{(\tilde{w}_i / \tilde{w}_j)} \tag{46}$$

being i the component that permeates preferably, in this case water. This expression is analogous to Equation (31) in Chapter 2. Table 9 presents the average separation factors observed during experiments M6 to M11, which were conducted around the operating point of the water-tolerant OME_{3-5} process. It is expected that the separation factors for OME_1 and OME_2 are higher compared to formaldehyde and methanol, given that the OME_n molecules are larger and less polar than formaldehyde and methanol. However, the separation factors are at least 16.42 in all cases, indicating that water can be selectively separated from all components. No evidence of flux or selectivity deterioration was observed. Figure 18 depicts the overall concentration of the permeate for experiments M6 to M11. The composition of the permeate remains remarkably stable throughout the experiments, indicating also that the selectivity of the membranes remains consistent over time. These findings indicate the stability of the membranes over the repeated measurements in the studied chemical system and under the studied operating conditions.

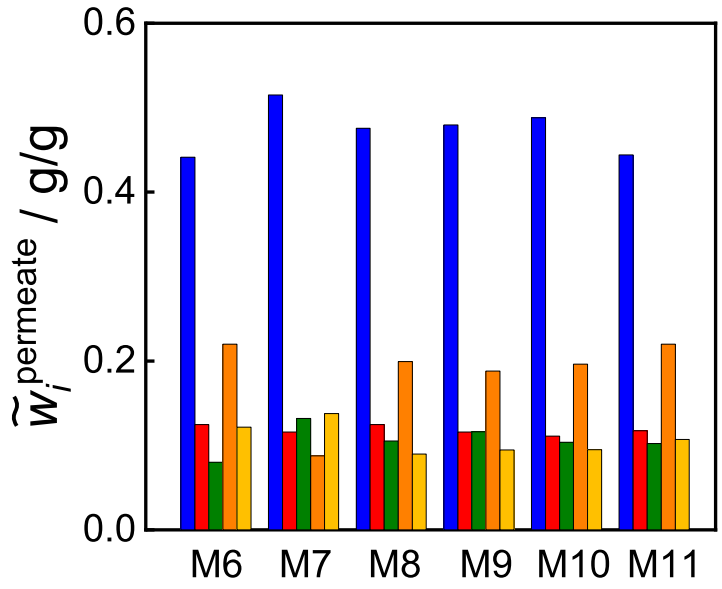

Figure 18: Experimental overall composition of the permeate for experiments M6 to M11. Blue: water, red: formaldehyde, green: methanol, orange: OME_1, yellow: OME_2.

While the separation factors for all components are indeed significant, it is worth noting that the overall concentration of water in the permeate, on average, is around 0.5 g/g for the operating point of the water-tolerant OME_{3-5} process described by Schmitz et al. [24]. Operating under such conditions would result in substantial losses of the organic components present in the system, as the permeate represents a stream that leaves the process. To address this issue, the next section explores alternative methods to further increase the selectivity towards water in the pervaporative separation.

Table 9: Average separation factors of experiments M6 to M11.

	$\alpha_{WA,j}$
formaldehyde	18.78
methanol	16.42
OME_1	24.01
OME_2	28.14

3.4.2 Further Purification of the Permeate

In the experiments, a two-stage condensation was employed. The compositions of the two condensates differed strongly. To illustrate this point, Figure 19 shows the experimental and simulated composition of the condensate from both the first and second stage. This data corresponds to one of the experiments conducted at the water-tolerant OME_{3-5} operating point by Schmitz et al. [24], specifically the experiment M9.

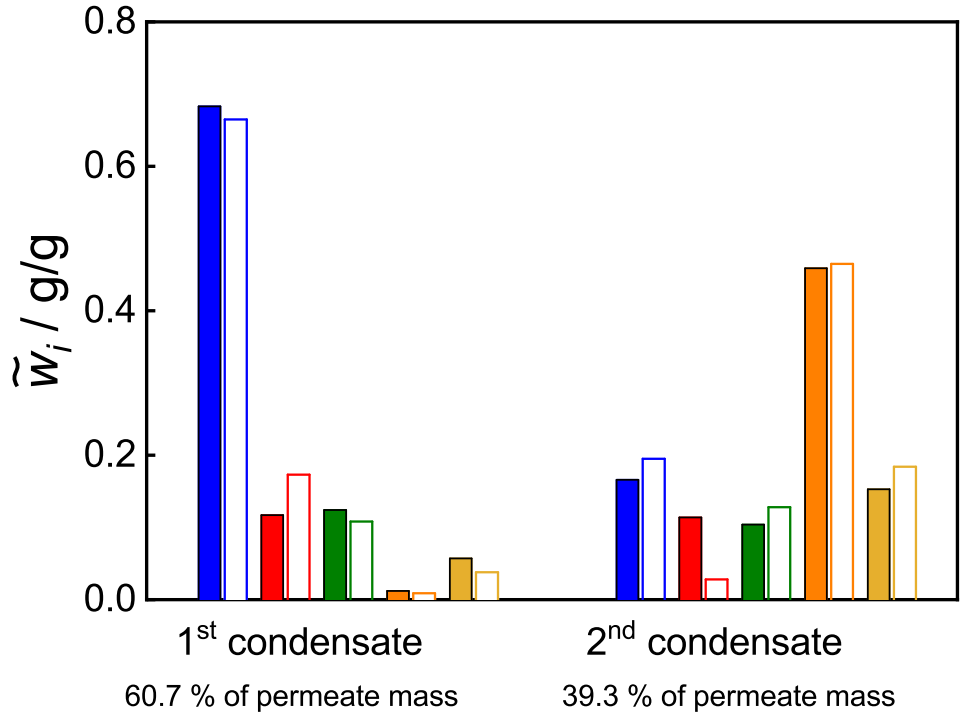

Figure 19: Experimental (filled bars) and simulated (empty bars) overall composition of the first and second condensate for experiment M9. Blue: water, red: formaldehyde, green: methanol, orange: OME_1, yellow: OME_2.

The first condensate primarily consists of water, while the second condensate is enriched with OME_1. This outcome is to be expected, considering that OME_1 is the most volatile component in this mixture. The overall mass fraction of water of the first condensate is 0.68 g/g, 42% higher than in the combined overall permeate. Therefore, it is possible to recycle the second condensate back into the process and to reject only the first condensate as a by-product stream of the process. To enhance this concept, the condensation ratio of the two stages could be adjusted, aiming to maximize the overall mass fraction of water in the first condensate.

The agreement between the experimental and the simulated composition is fairly good, especially for water, methanol, OME_1 and OME_2. The overall mass fraction of formalde-

hyde in the first condensate is slightly overestimated. One possible reason for this discrepancy could be that the chemical equilibrium of Reactions (10) – (13) is not fully achieved as assumed by the model. This is plausible considering the relatively low temperatures and residence times in both condensation stages, which influence the reaction kinetics. Since the model adequately captures the qualitative extent of the condensation, there was no consideration given to extending the model to include the kinetics of (10) – (13).

A generalization of the two-stage condensation concept could involve implementing a multi-stage separation process. To explore this idea, a further refinement of the combined overall permeate from experiment M9 in a rectification column was simulated. For this, an equilibrium stage column model, which considers the chemical Reactions (10) – (13) was used. The chemical equilibrium is assumed to be established on every stage. The results showed that it is feasible to obtain a bottom product with an extremely high overall mass fraction of water (> 0.9999 g/g) and achieve a water recovery of 77% under reasonable operating conditions (22 equilibrium stages, reflux ratio = 3, top pressure = 4 bar). The top product, predominantly composed of formaldehyde, methanol, OME_1, and OME_2, could be recycled back into the process. Details about the simulation including the specifications of the distillation column and a full stream table can be found in the Appendix B.5 By combining the membrane unit for breaking the azeotrope that water forms with formaldehyde and OME_2 [27] with the distillation unit for high-purity water production, this approach presents a potential solution for achieving an efficient separation of water in the process.

Another alternative to further purify the permeate stream is to employ two pervaporation units in series, where the condensed permeate from the first stage is fed into the second pervaporation unit. The composition of the permeate from experiment M9 is similar to the feed composition of experiment M12. In experiment M12, the overall mass fraction of water in the permeate is 0.73 g/g, i.e., 52% higher than in experiment M9. This concept can be extended by incorporating multiple pervaporation units in series, allowing for additional purification steps.

To enhance the overall mass fraction of water in the permeate, it would be beneficial to identify process conditions under which the SiO_2 membrane reaches the performance of the screening experiments also in larger scale. Further, it would be interesting to explore more selective membrane materials than SiO_2. Novel mixed matrix blend membranes could be potential candidates for this separation task, offering the possibility of improved performance and stability.

4 Overall Process

4.1 Introduction

The distillation column in the water-tolerant OME_{3-5} process by Schmitz et al. [24] is a complex separation step. This complexity arises from several factors including its reactive and multicomponent character, the high formaldehyde concentrations in the feed, and the presence of several azeotropes [24, 27].

Several experimental studies involving distillation of similar chemical systems containing formaldehyde and alcohols have been carried out. Ott et al. performed distillation experiments in the system (formaldehyde + methanol + water) and used an equilibrium stage model to predict column profiles [83]. Dyga et al. studied the behaviour of the system (formaldehyde + water + isoprenol) by performing single-stage batch distillation experiments [84]. Also a number of works have focused on the production of acetals like 1,3-dioxolane from aqueous formaldehyde and alcohols by catalysed reactive distillation [85–87]. Weidert et al. [88] investigated the system (formaldehyde + methanol + water + OME_1). Schmitz et al. [27] and Mantei et al. [29] presented experiments and models of reactive distillation columns in the system (formaldehyde + methanol + water + OME_n). However, they have studied operating points significantly varying from the operation point suggested by Schmitz et al. [24] For example, Schmitz et al. [27] studied relatively small formaldehyde concentrations below 0.05 g/g in the feed. In the operating point proposed by Schmitz et al., the concentration of formaldehyde in the column is very high and expected to be close to the solubility limit in the studied chemical system [24, 71, 72, 89]. The practical demonstration of the feasibility of the operation point of the distillation-based water-tolerant OME_{3-5} process remains hence an open question. Most importantly, the experimental demonstration of the process with closing recycles is missing.

This chapter presents a series of mini-plant experiments that closely approximate the operating conditions suggested by Schmitz et al. [24]. While the water separation has been extensively studied in Chapter 2 and Chapter 3, this chapter focuses on the distillation column and the overall process. As mentioned in Chapter 1, the second distillation col-

umn that further narrows down the product OME_{3-5} by removing $OME_{\geq 6}$ was omitted in the present work because the obtained product in Stream 4 was already quite clean and contained little $OME_{\geq 6}$, cf. Sections 4.4.2 and 4.4.4. Moreover, the cycle shown in Figure 1 is the core of the process.

4.2 Experimental Methodology

4.2.1 Chemicals, Catalyst and Membranes

Paraformaldehyde (> 0.895 g/g) and OME_1 (> 0.997 g/g) were acquired from Prefere. Methanol (> 0.998 g/g) was purchased from VWR. OME_{3-6} (> 0.9684 g/g) was obtained from ASG. Ultra-pure water was obtained from a PURELAB Classic water purification system from ELGA. The catalyst of the tubular reactor, the ion exchange resin Amberlyst 46, was provided by DuPont. The four-channel ceramic SiO_2 membranes were acquired from the Fraunhofer Institute for Ceramic Technologies and Systems (IKTS), as described in Section 3.2.1.

4.2.2 Analytics

The overall mass fractions of each component and the catalyst activity were determined according to the procedures described in Section 2.2.3.

4.2.3 Preparation of Feed Solutions

The feed consisting of a methanolic formaldehyde solution for Runs 1 - 6 was prepared by stirring paraformaldehyde and methanol at around 60 °C for several weeks within a 200 L barrel. For Runs 7 - 10, this methanolic formaldehyde solution was additionally reacted with OME_1 in a batch reactor employing the catalyst Amberlyst 46 and analysed prior to usage (volume = 200 L, temperature = 60 °C, pressure = 1 bara). In all cases, the composition of the feed was inspired by the studied operation point, cf. below.

4.2.4 Tubular Reactor Setup

The tubular reactor used in the present work is a fixed-bed tubular reactor with a tubular bed length of 4.8 m, a tube diameter of 16.6 m, a bed volume of 1.03 L, and is filled with

309 g of dry catalyst Amberlyst 46. Details regarding the reactor thermostatization and control structure as well as a P&ID diagram are given elsewhere [30]. A tank containing the reactor feed is placed on a scale (Kern, accuracy: 1 g) and the feed mass flow rate (Stream 2, cf. Figure 1) is determined from the change of the feed mass over time.

4.2.5 Distillation Column Setup and Control Structure

The distillation column is a stainless steel distillation column with 70 mm inner diameter from Iludest, which is operated under pressure. A P&ID diagram of the column including its control configuration is depicted in Figure 20. The top pressure is controlled using a small through-flow of inert gas (nitrogen). The condenser E102 is located directly at the top of the column and operated with water (inlet temperature roughly 7 °C). Eventual uncondensed gases are captured in the cold trap E106, which is filled with liquid nitrogen. The reflux ratio is set by the opening frequency of the automatic valve AV103. The temperature of the distillate is brought close to ambient temperature in the cooler E104, which is operated with a mixture of ethylene glycol, which is cooled down in an external thermostat to around 18 °C. The level in the distillate drum B102 is maintained by manipulating the automatic valve AV104 to let the liquid out. The liquid in the distillate drum also acts as a hydraulic lock to maintain the pressure in the column. Electrical heating jackets (SAF, maximal power: 100 W) along the column reduce the heat losses. The column is equipped with 3.84 m of a structured packing (Sulzer CY). The reboiler E101 is a shell-and-tube heat exchanger at the bottom of the column. The liquid evaporates in the tubes, while the shell is fed with hot oil. The oil is heated in the external thermostat TH101. The level in the reboiler E101 is measured by the differential pressure measurement PDI101 and controlled by manipulation of the heat duty of the thermostat TH101. The bottoms are pumped out of the column by a gear pump (Gather). Set-points are given for the reflux ratio, the feed mass flow rate and the bottom mass flow rate. The process control system is implemented using the commercial software LabVIEW v19.0. All controllers are PID except LC101, which is an only-P controller to avoid excessive delays. The mass flow rates of the bottom and the top product (Streams 4 and 5, cf. Figure 1) are determined from the change of the weight over time on the scales A103 and A102 respectively (Kern, accuracy: 2 g). Liquid samples can be then taken at various positions of the column and from the product streams.

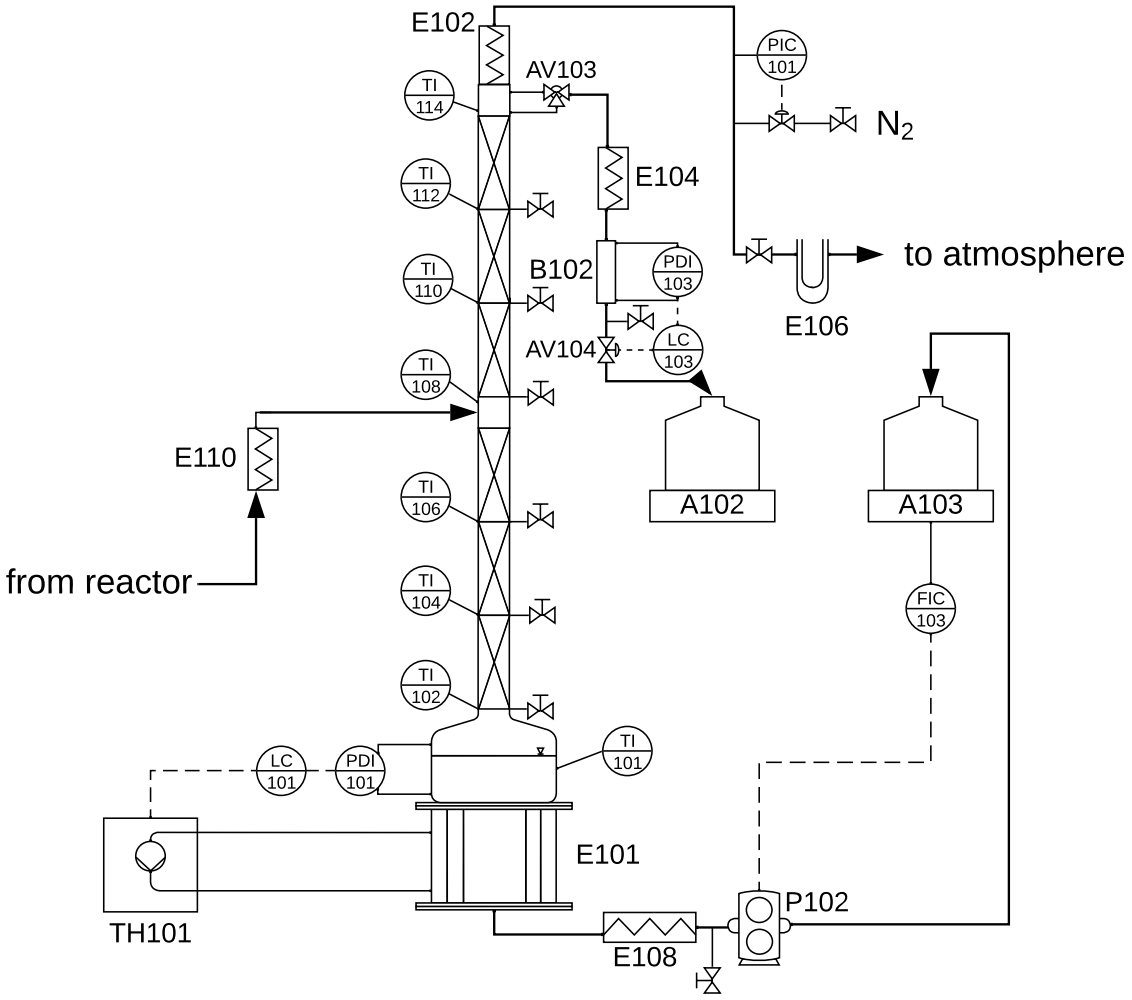

Figure 20: P&ID diagram of the distillation setup.

4.2.6 Pervaporation Setup

The pervaporation unit is described in detail in Section 3.2.2.

4.2.7 Procedure

4.2.7.1 General Procedure

Since the membrane unit could not operate continuously, the plant was operated for several runs with open cycle, i.e., the recycle Stream 6 was not continuously fed back but instead collected and then mixed with the feed mixture from Stream 1. This mixture yielded three tanks with the composition of Stream 2. The reactor and the distillation column were then operated continuously until the tanks were empty. Each tank, holding approximately 25 L, typically lasted around 3 hours.

The composition in chemical equilibrium (roughly given at Stream 3 after the reactor) has two degrees of freedom: (a) the ratio of $-CH_2$ and $-CH_3$ groups, and (b) the ratio of $-OH$ and $-CH_3$ groups, cf. Voggenreiter et al. [52] for details, who introduced the acidic overall composition to describe these degrees of freedom. Consequently, the composition of Stream 2 has the same two degrees of freedom when starting a run. In the initial run (Run 1), the tank of Stream 2 was filled based on the predicted composition of Schmitz et al. [24]: $\tilde{w}^{(2)}_{\mathrm{FA}} = 0.202$ g/g, $\tilde{w}^{(2)}_{\mathrm{ME}} = 0.082$ g/g, $\tilde{w}^{(2)}_{\mathrm{WA}} = 0.033$ g/g, $\tilde{w}^{(2)}_{\mathrm{OME_1}} = 0.448$ g/g, $\tilde{w}^{(2)}_{\mathrm{OME_2}} = 0.224$ g/g, $\tilde{w}^{(2)}_{\mathrm{OME_{\geq 3}}} = 0.011$ g/g. For the subsequent runs (Runs 2 - 6), the retentate of the membrane unit (Stream 6) was mixed in a mass ratio of 8:1 with fresh feed (Stream 1). This ratio was fixed and adopted from Schmitz et al. [24]. Following this procedure, the process flows will eventually converge to constant values, remaining consistent across runs.

Note that experiments M6 - M11 from Chapter 3 correspond to Runs 2 - 6 in this chapter. In Chapter 3, the emphasis was put on the pervaporation unit, whereas in this chapter, the focus shifts to the overall process and the material balances.

Additionally, a series of runs was performed in open loop using only the reactor and the distillation column (Runs 7 - 9) or only the distillation column (Run 10). These runs were carried out to vary some parameters of the distillation column, i.e., feed mass flow rate, feed composition, reflux ratio, and distillate-to-feed ratio. The duration of Runs 7 - 10 varied between 4 and 20 hours. Table 10 presents an overview of all runs performed in this work. For each run, the experiment type (reaction, distillation and pervaporation (R+D+P); reaction and distillation (R+D); or only distillation (D)), the mass flow rate

of the distillation column feed $\dot{m}^{(3)}$, the overall mass fraction of formaldehyde in the distillation column feed $\tilde{w}_{\mathrm{FA}}^{(3)}$, and the reflux ratio are given.

Table 10: Overview of the experimental conditions of Runs 1 - 10.

	experiment type	$\dot{m}^{(3)}$ / kg/h	$\tilde{w}_{\mathrm{FA}}^{(3)}$ / g/g	reflux ratio
Run 1	R+D+P	6.16	0.147	0.5
Run 2	R+D+P	5.86	0.153	0.5
Run 3	R+D+P	6.54	0.177	0.5
Run 4	R+D+P	6.78	0.172	0.5
Run 5	R+D+P	6.86	0.169	0.5
Run 6	R+D+P	6.98	0.166	0.5
Run 7	R+D	7.04	0.170	0.5
Run 8	R+D	7.40	0.183	0.5
Run 9	R+D	7.68	0.154	0.5
Run 10	D	4.82	0.122	1

4.2.7.2 Procedure of Each Unit

The reactor temperature was set to 70 °C and the inlet pressure to approximately 4 bara to ensure that the reaction mixture remains liquid during the operation. The reactor was preheated the day before. On the operation day, the reactor was completely filled with liquid. The reactor product was recirculated for approximately 30 minutes to allow for temperature stabilization [30]. The mass flow rate varied between 5.86 kg/h - 7.68 kg/h.

The top pressure in the distillation column was set at 1.4 bara. The reflux ratio was set at a value of 0.5 for Runs 1 - 9 and at 1 for Run 10. The heating power of the heating jackets was set to 70% of their maximum capacity. In preliminary experiments, the reboiler was filled with the feed mixture and heated at total reflux. After a few hours, formaldehyde precipitated in the bottom of the column. Because of the low boiling temperature of the feed mixture (about 80 Â°C at 1.4 bara), the light boiling solvents such as OME_1, methanol and eventually water evaporate, while formaldehyde tends to remain in the sump. Since the solubility of formaldehyde in OME_n is very low [89], it precipitates eventually. To overcome this problem, in the present work, the reboiler was filled prior to the experiment with approximately 5 kg of a liquid mixture having a high boiling temperature, in this case a mixture of $\mathrm{OME}_{3\text{–}6}$. This ensures a high enough temperature in the bottom right from the start of operation. For Run 1, a commercial

mixture of $OME_{3–6}$ was used while for the subsequent experiments, the bottom product of the previous run was used. Samples from different positions in the reactor and column as well as samples from the reactor feed, the column feed, the distillate and the bottom products were taken regularly. The average mass flow rates of the reactor feed, bottom and top products of the distillation column ($\dot{m}^{(2)}$, $\dot{m}^{(4)}$ and $\dot{m}^{(5)}$ cf. Figure 1) were determined and the material losses were calculated. The mass flow rate corresponding to the cold trap E106 (in all cases < 0.2 kg/h) was determined by weighing and added to the distillate stream

The procedure for the membrane operation for Runs 1 - 6 was described in Section 3.2.5. The temperature in the feed tank was set to 50 °C, while the pressure in the permeate side was approximately 80 mbara. Samples from the feed were taken regularly and analysed. When an overall mass fraction of water of roughly 0.025 g/g in the feed was reached, the run was stopped. The whole system was vented and both permeate and feed tanks were emptied.

4.3 Modelling Methodology

4.3.1 Chemical Reactions

The model to describe the Reactions (10) – (13) is the same than in the section 2.3.1. Furthermore, under acidic conditions hemiformals acetalize to OME_n and their chain length can be prolonged by addition of formaldehyde [26]:

$$HF_1 + ME \overset{H+}{\rightleftharpoons} OME_1 + WA \tag{47}$$

$$HF_n + ME \overset{H+}{\rightleftharpoons} OME_n + WA \quad ; \quad n > 2 \tag{48}$$

$$FA + OME_1 \overset{H+}{\rightleftharpoons} OME_2 \tag{49}$$

$$FA + OME_{n-1} \overset{H+}{\rightleftharpoons} OME_n \quad ; \quad n > 2 \tag{50}$$

The model used in the present work to describe the formation of OME_n from methanol and formaldehyde was adopted from Voggenreitter et al. [30] and is based on the model originally developed by Schmitz et al. [26]. The chemical equilibrium of Reactions (10) –

(13) is described using chemical equilibrium constants based on mole fractions. The temperature dependence of these constants is calculated using the Van 't Hoff equation. Reactions (47) – (50) proceed at a significantly slower rate compared to Reactions (10) – (13) [56], which are assumed to be instantaneous. Therefore, Reactions (47) – (50) are considered to be kinetically controlled and are modelled using temperature-dependent reaction rate constants adopted from [30].

4.3.2 Vapour-Liquid Equilibrium

The model for the vapour-liquid equilibrium is adopted from Schmitz et al. [27]. Since details can be found there, only the main assumptions are mentioned in the following. The extended Raoult's law is used to describe the vapour-liquid equilibrium of the system. The vapour phase is assumed to be a mixture of ideal gases, whereby poly(oxymethylene) glycols and poly(oxymethylene) hemiformals of chains longer than 1 are considered non-volatile. The liquid phase is treated as non-ideal mixture of formaldehyde, water, methanol, OME_n and the formaldehyde oligomers MG_n and HF_n with up to $n = 10$. It has been shown that this is sufficient when the overall mass fractions of formaldehyde are lower than 0.5 g/g [83]. The non-ideality of the liquid phases is described using a tailor-made version of the UNIFAC activity model [61]. A schematic representation of the combined model for the vapour-liquid equilibrium including the chemical reactions is given in Figure 21.

4.3.3 Solid-liquid Equilibrium

The solid-liquid equilibrium model for the solid formation in the system (formaldehyde + water + methanol + OME_n) is adopted from the work of Breitkreuz et al. [72] Details regarding the model are not discussed here, but only the main idea is mentioned. Reactions (10) – (13) are considered. It is assumed that one poly(oxymethylene) glycol of chain length p = 9 reaches the solubility limit first. Upon getting solid, it releases one molecule of water to the liquid phase while forming polymeric formaldehyde within the solid phase. Assuming temperature independence of p, the model enables to predict the freezing temperature of a certain liquid mixture. Furthermore, it offers estimates for the time required to achieve equilibrium, which can be over 1000 days depending on the conditions [72].

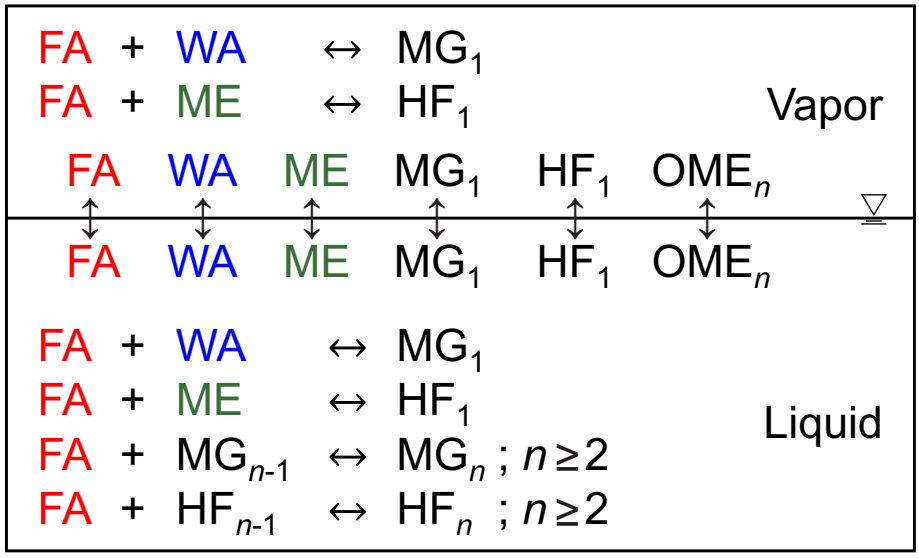

Figure 21: Scheme of the reactive vapour-liquid equilibrium model in the system (formaldehyde + methanol + water + OME_n). Adapted from the work of Schmitz et al. [27].

4.3.4 Reactor Model

The model of the tubular reactor is adopted from Voggenreiter et al. [30] The reactor is thereby modelled as an isothermal plug flow reactor (PFR) with pseudo-homogeneous kinetics, whereby all Reactions (10) – (13) and (47) – (50) are considered. The reactor model is implemented using the software gPROMS 7.0.7. For the simulations, the feed composition, the feed mass flow rate, the inlet pressure, and the temperature were specified.

4.3.5 Distillation Column Model

The distillation column C is modelled using an equilibrium stage approach that considers the chemical Reactions (10) – (13) and the vapour-liquid equilibrium, cf. Figure 21. The chemical equilibrium is assumed to be established on every stage, following Schmitz et al. [27]. The solid-liquid equilibrium is not considered when calculating the distillation column, because it would change the structure of the equation depending on the existence of a solid phase. Instead, in a post-processing step, the freezing temperature of the liquid phase is calculated from the solid-liquid equilibrium model [72] at different column positions using the experimentally determined overall mass fractions. The separation efficiency of the CY-packing is taken from the Sulzer product data sheet with

a HETP-value of 0.128 m/stage, leading to a total separation efficiency of 30 stages for the packing [88, 90]. The equilibrium stage model is implemented in Aspen Plus v.8.8. For the simulations, the top pressure, the reflux ratio, the feed mass flow rate and composition as well as the mass fraction of OME_3 at 0.43 m from below were specified to the experimental values. This selection is based on preliminary sensitivity studies.

4.4 Results and Discussion

4.4.1 Tubular Reactor

Figure 22 presents the composition profiles along the reactor in steady-state for Run 4 as an example. Corresponding profiles for other runs can be found in the Appendix C.1. The results are expressed in terms of pseudo residence time, defined as the mass of catalyst passed divided by the mass flow rate through the reactor. This parameter serves as an indicator of the reactor length [30]. At the outlet, the reactor product closely approaches chemical equilibrium conditions, as expected for the process [24]. However, a slight catalyst deactivation is noticeable in the first half of the reactor, as the model is faster in this section. As highlighted by Voggenreiter et al. [30], catalyst deactivation primarily results from the presence of cations in the feed solutions. The authors discussed potential remedies for this issue, such as feed pretreatment or the implementation of a guard bed before the reactor. None of these measures were applied in the current study. Since the catalyst had been in use for over 100 hours before the present work, the first half of the reactor exhibited some deactivation. Throughout Runs 1 - 9, no further change or deactivation was observed, cf. Appendix C.1. The observed catalyst deactivation in the initial section of the reactor did not hinder the performance of the distillation column and the water separation, as equilibrium conditions were approached in the second half of the reactor. The duration of the experimental runs (time on stream) was not sufficient to provide further insights into deactivation kinetics.

4.4.2 Distillation Column

4.4.2.1 Composition and Temperature Profiles

Typically, steady-state was achieved after 4 to 5 hours of operation. This was judged based on constant temperatures and liquid composition profiles. In the following, it is always referred to steady-state results. Figures 23 and 24 exhibit the composition and

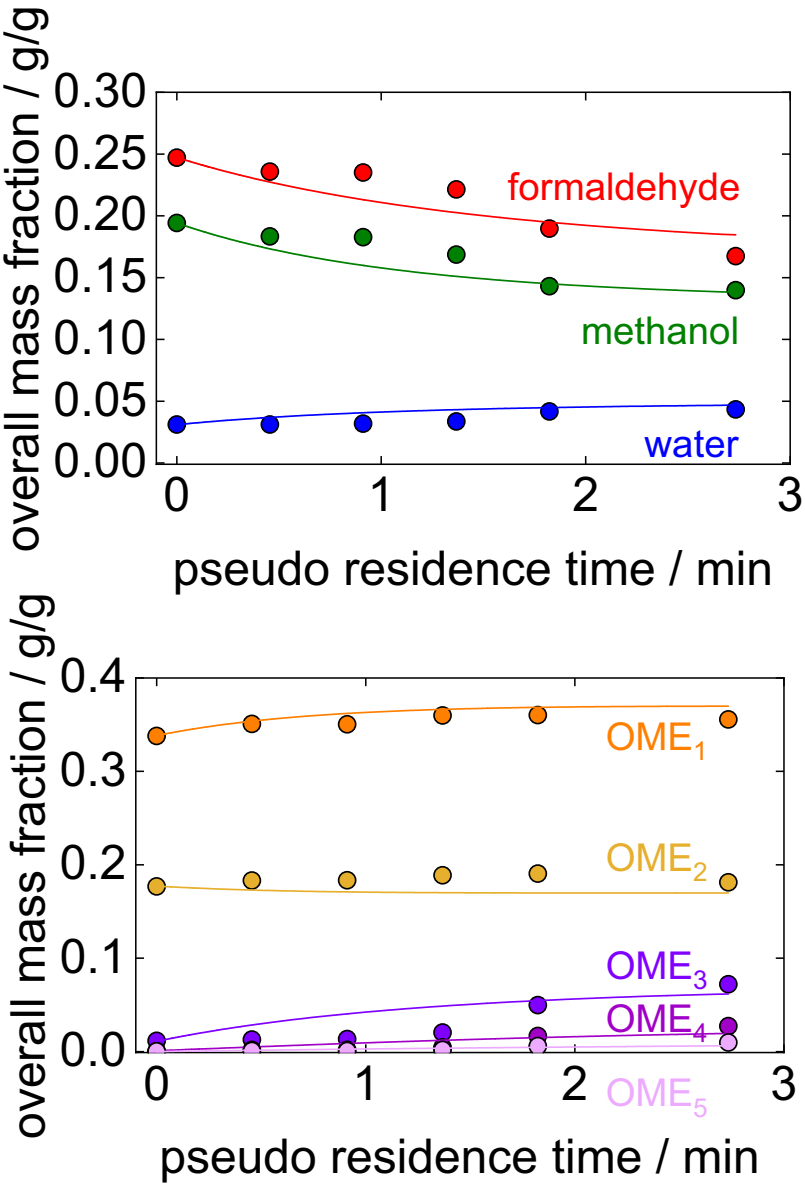

Figure 22: Reactor profiles of overall mass fractions corresponding to steady-state of Run 4. Filled circles: Experimental results. Solid lines: Simulation specified with the experimental starting composition.

temperature profiles corresponding to Run 7 and Run 10, respectively. Similar plots for other runs are given in the Appendix C.2. The agreement between experiments and simulations is good for the majority of components. Particularly, the agreement for both key components of the separation, formaldehyde and OME_3, is satisfactory. However, in both runs, the simulation underestimates the overall mass fraction of methanol along the column. This disagreement is stronger for Run 10. A possible reason for this discrepancy in the methanol profiles could be that the model assumption of chemical equilibrium in the liquid phase is not completely satisfied. Since Reactions (12) – (13) are much slower than Reactions (10) and (11), methanol could remain bound in form of long-chain poly(oxymethylene) hemiformals and not be able to be transferred to the gas phase [83]. The internal liquid mass flow rates in the column are smaller for the Run 7 than for Run 10 because the reflux ratio is smaller. Hence, the residence time is larger and the kinetic limitations are less important than in Run 10. To improve the model, Reactions (10) – (13) could be modelled kinetically. This would however increase the complexity of the model notably and was out of scope of the present work.

Overall mass fractions of formaldehyde around 0.5 g/g in the middle part of the column are typical in all runs. For both Run 7 and Run 10, the freezing temperatures predicted by the solid-liquid equilibrium model using the experimental compositions are slightly higher than the actual temperatures as shown in Figures 23 and 24, i.e., the model predicted that formaldehyde precipitation is possible in the central part of the column. However, no solid precipitation was observed during the runs. All samples were clear liquids when taken. Some of them got solid once they had cooled down completely and after several hours. These solid samples were heated up to 65 °C in order to be able to analyse them. Thereby, the samples dissolved completely and remained clear even for some minutes after the heating had been turned off. This discrepancy between model and experimental observation could be explained by the fact that the model has a considerable uncertainty due to extrapolation [72]. Here, the model is used far outside the conditions where it was developed. Moreover, the precipitation of formaldehyde is kinetically limited and can take up to many hundreds of days [72]. Since the residence time of the liquid internal streams in the column is much smaller than this, the equilibrium is probably not reached in any case.

4.4.2.2 Trade-Off Formaldehyde - $OME_{\geq 3}$

The separation task of the distillation column is to separate the key components formaldehyde (distillate) from $OME_{\geq 3}$. According to the literature [24, 27, 29], a sharp split is not possible for both simultaneously. The reason is the non-ideal phase behaviour of

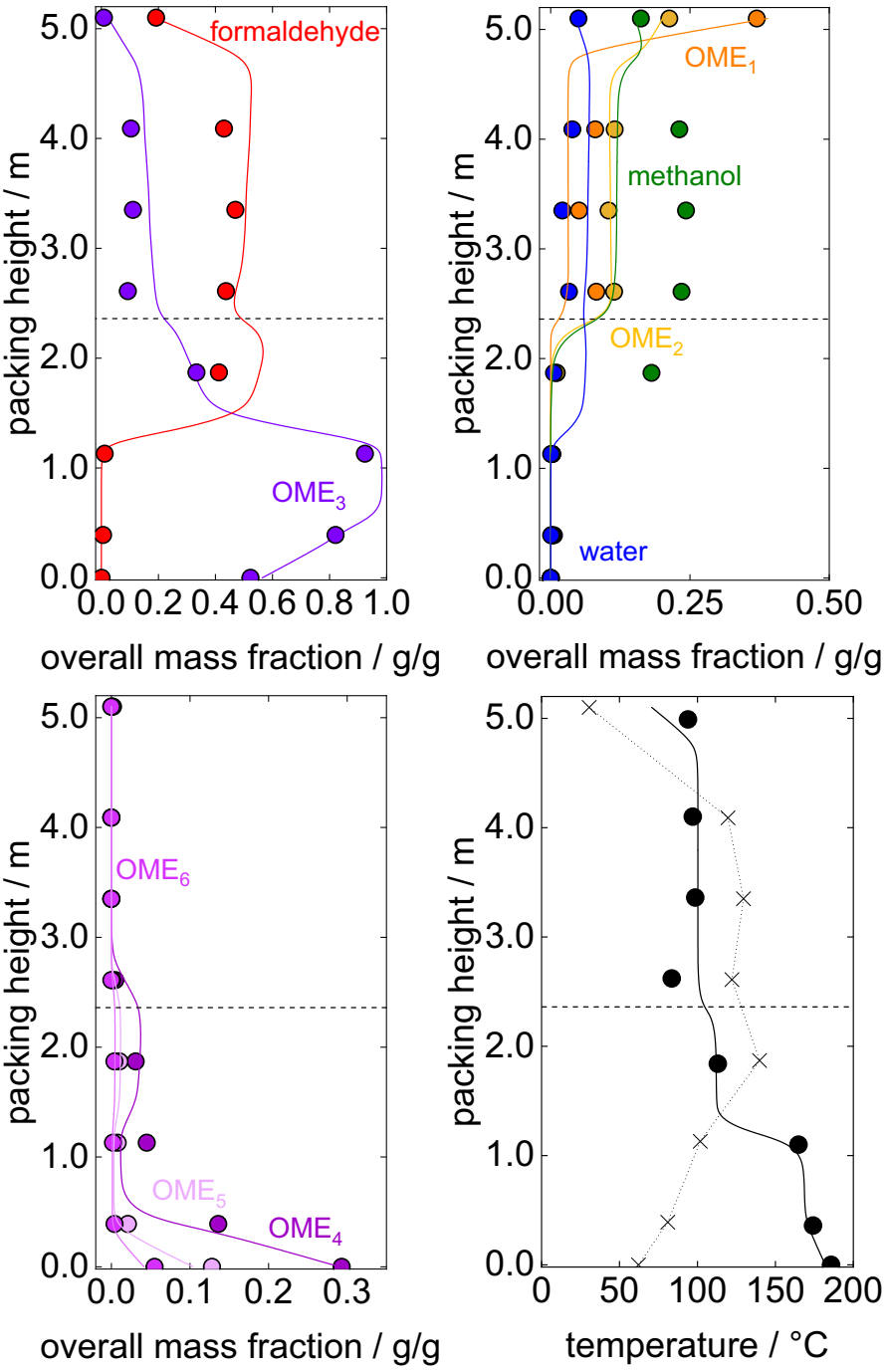

Figure 23: Distillation profiles of overall mass fractions in the liquid phase and temperature corresponding to Run 7. Filled circles: Experimental results. Solid lines: Simulation using equilibrium stage model, where the mass fraction of OME_3 at 0.43 m and reflux ratio were specified. Dashed line: Feed position. Crosses: predicted freezing temperatures. Dotted line: predicted freezing temperatures (interpolation).

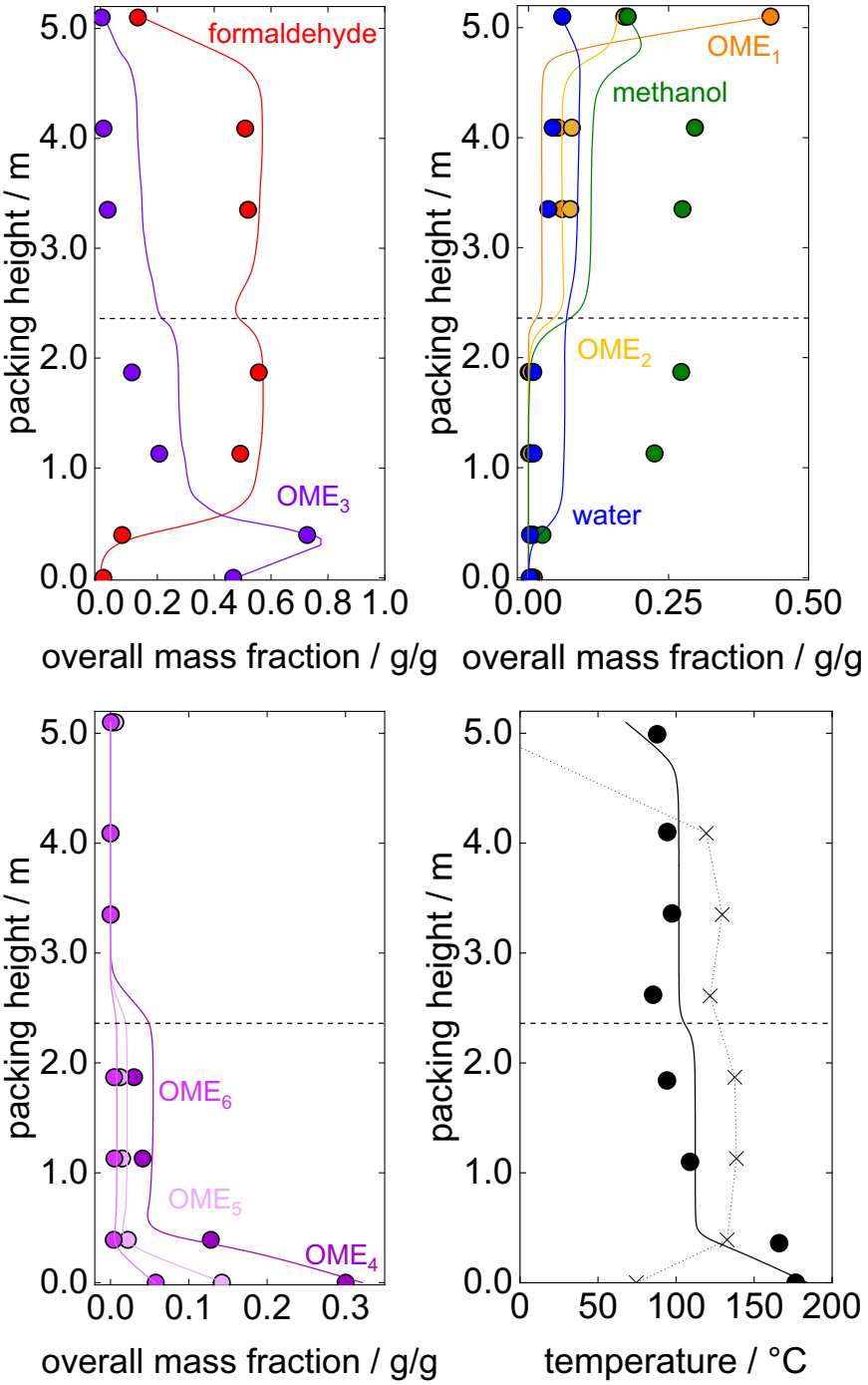

Figure 24: Profiles of mass fractions in the liquid phase and temperature corresponding to Run 10. Filled circles: Experimental results. Solid lines: Simulation using equilibrium stage model, where the mass fraction of OME_3 at 0.43 m and reflux ratio were specified. Dashed line: Feed position. Crosses: predicted freezing temperatures. Dotted line: predicted freezing temperatures (interpolation).

the system. In the present work, the trade-off between the recoveries of the two key components at different distillate-to-feed ratios of the distillation column around the operating point are studied. The results are shown in Figure 25. The x-axis shows a dimensionless measure P for the distillate-to-feed mass ratio:

$$P = \frac{1 - \frac{\dot{m}^{\text{bottom}}}{\dot{m}^{\text{feed}}}}{1 - \tilde{w}^{\text{feed}}_{\text{OME}_{\geq 3}}} \tag{51}$$

When $P = 1$, the distillate-to-feed ratio is equal to the one needed for an ideally sharp split, i.e., the sum of the overall mass fractions of formaldehyde, water, methanol, OME_1 and OME_2 in the column feed. When $P > 1$, the distillate-to-feed ratio is larger, respectively.

The mass recovery MR_i of component i in the distillate as shown on the y-axis is defined as:

$$MR_i = \frac{\tilde{w}_i^{\text{feed}} \cdot \dot{m}^{\text{feed}} - \tilde{w}_i^{\text{bottom}} \cdot \dot{m}^{\text{bottom}}}{\tilde{w}_i^{\text{feed}} \cdot \dot{m}^{\text{feed}}} \tag{52}$$

The mass recovery of component i in the distillate is calculated in this indirect way via the bottom product as it is assumed that the material losses in the experiments occur mainly in the distillate stream.

In Figure 25, the modelled curve corresponds to the feed condition of Run 7. Note that every run has a slightly different feed and thus its own modelled curve, but since these curves are very similar and for the sake of clarity, only one of them is presented. The agreement between simulation and experiments is fairly good for $\text{OME}_{\geq 3}$. For formaldehyde, the experiments slightly outperform the model predictions. A clear trade-off between formaldehyde recovery and $\text{OME}_{\geq 3}$ recovery is recognisable, confirming that achieving a perfectly sharp separation between formaldehyde and $\text{OME}_{\geq 3}$ is not feasible. However, it is possible to reach a very high formaldehyde recovery in the distillate by accepting a loss of between 20% and 30% of the $\text{OME}_{\geq 3}$ present in the feed into the top product, which is recycled.

The overall mass fractions of formaldehyde in the bottom products of the distillation column were consistently below 0.002 g/g. In the final runs, formaldehyde became undetectable using the sodium-sulfite method, proving a very high product quality, even when omitting the second distillation column. In an external post hoc analysis of two bottom samples from Run 11 conducted by ASG Analytik-Service using the method ASG 1855 [91], a formaldehyde mass fraction of approximately 0.0008 g/g (800 ppm)

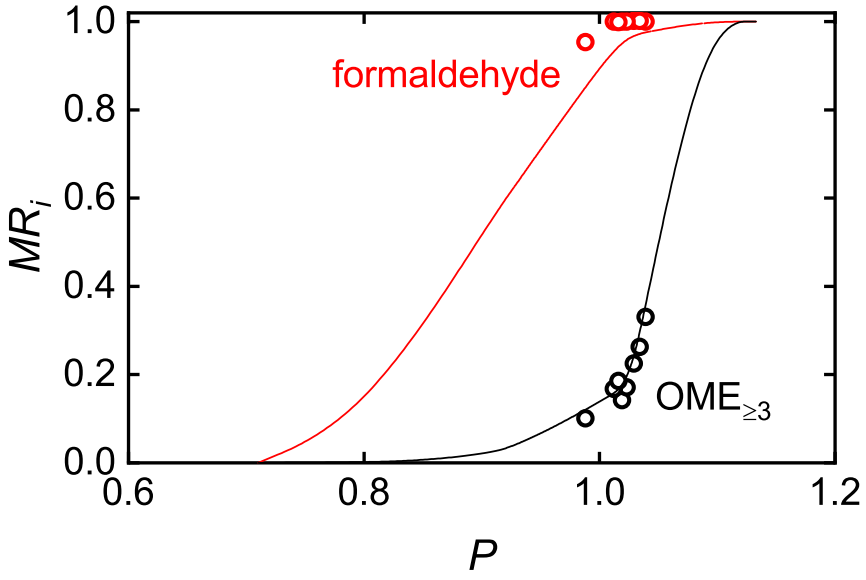

Figure 25: Mass recovery of formaldehyde (red) and $OME_{\geq 3}$ (black) in the distillate as a function of the proportion of the real to the theoretical distillate-to-feed ratio.

was measured. It is reasonable to infer that further increasing the distillate-to-feed ratio would result in even lower impurity levels in the bottom product.

Furthermore, it is worth noting that after each run and during the cooling-down phase in between, formaldehyde, water, and other light components inevitably accumulate in the lower part of the column. Despite the efforts to empty the distillation column before commencing a new experiment, completely purging the reboiler, the bottom pump, and the tubing of formaldehyde residues remains an arduous task. To effectively remove any residual formaldehyde, an extensive cleaning of the column and/or prolonged operation times would be necessary.

4.4.3 Pervaporation

Detailed results on the drying using the pervaporation unit in Runs 1 - 6 are reported in Chapter 3, cf. Section 3.4.

4.4.4 Overall Material Balance

The unaccounted material losses in the distillation column were on average 3.7% of the column feed, while the material losses in the membrane unit only 1.2% of the membrane feed. It is not too surprising that the losses in the distillation column are around three times larger than the losses in the membrane unit since the temperatures in the distillation column are considerably higher. While these losses appear small on first sight, when put into respect of the process feed, they are 41% for the distillation column and 13% for the membrane, respectively. This occurs because of the intrinsically large recycle-to-product ratio of the process, which is determined by the chemical equilibrium of the system [24]. Hence, minimizing the losses of both the distillation column and the membrane are crucial for commercial operation.

The presence of side products reported in the literature [52] such as methyl formate, formic acid, and trioxane was detected only in negligible amounts, being their mass fractions < 0.002 g/g in all cases. Also, no systematic increase in their values was observed along from run to run.

Throughout Runs 1 - 6, consistent operating conditions were maintained: mixing ratio of recycle and process feed; temperature and pressure in the reactor; top pressure, reflux ratio, and distillate-to-feed ratio in the distillation column; final overall mass fraction of water in the membrane feed, membrane temperature and permeate-side pressure. Although the compositions of Streams 1 - 7 exhibited minor fluctuations during these experiments, these fluctuations did not display any significant trend over time. Figure 26 visually illustrates the overall mass fractions of water and formaldehyde in the reactor feed (Stream 3) across Runs 1 to 6. Additionally, Table 11 offers detailed information on the overall mass fractions and mass flow rates of Streams 1 to 7 for Run 6. The stream tables for the remaining runs are given in the Appendix C.3.

Upon observing Table 11, it becomes evident that there are significant losses of organics in the permeate (Stream 7), which represent a notable drawback. As previously discussed, this issue primarily stems from the limited selectivity of the SiO_2 membrane against water under the investigated conditions.

4.4.5 Water Separation via Adsorption: Simulation Study

In the following, the scenario in which an adsorption unit is used for the water separation is simulated.

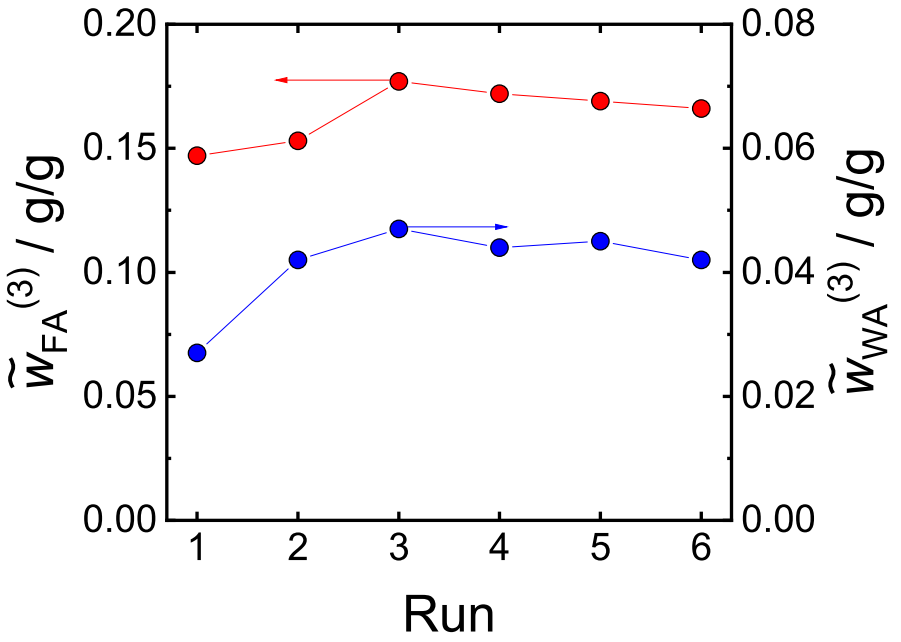

Figure 26: Overall mass fractions of water (blue) and formaldehyde (red) in Stream 3 (reactor feed) over Runs 1 to 6.

Based on the insights gained on water separation efficiency using zeolite 3A in Chapter 2, it is aimed to obtain a rough estimate of the overall performance for the water separation step by simulation. In this regard, Figure 1 will be referred. For the reactor R, the isothermal reactor model developed by Voggenreiter et al. [30] is used (tubular bed length = 4.8 m, tube diameter = 16.6 mm, bed volume = 1.03 L, dry mass of catalyst = 309 g, temperature = 70 °C). Regarding the distillation column D, a complete separation of formaldehyde, methanol, water, OME_1, and OME_2 in the top product is assumed, along with 0.3 g/g of the OME_3 contained in Stream 3. Simultaneously, 0.7 g/g of the OME_3 in conjunction with all $OME_{>3}$ present in Stream 3, is directed to the bottom product [27]. This assumption was made as a simplification of the observations outlined in Section 4.4.2.

For the adsorption step A, Stream 5 is assumed to have a consistent flow rate of 1 kg/h (= 16.7 g/min), within the experimental range studied in the present work. This stream enters a freshly regenerated column (dimensions as in the experiments of this work). The cumulative average stream from the column become Stream 6, and the adsorbed components become Stream 7. The model developed within this study is used to calculate the outlet and loading of the column over time. The regeneration of the adsorbent was not modelled explicitly, under the assumption that enough beds are available to ensure uninterrupted operation, with a regeneration efficiency of 100%, i.e.,

Table 11: Stream table of Run 6.

		stream number						
		1	2	3	4	5	6	7
overall mass fractions /g/g	FA	0.521	0.221	0.166	0.001	0.181	0.203	0.118
	ME	0.423	0.176	0.136	0.000	0.152	0.151	0.102
	WA	0.053	0.028	0.042	0.000	0.046	0.030	0.444
	OME_1	0.000	0.367	0.356	0.000	0.391	0.388	0.220
	OME_2	0.000	0.193	0.185	0.000	0.206	0.202	0.107
	OME_3	0.000	0.013	0.073	0.499	0.022	0.024	0.009
	OME_4	0.000	0.000	0.028	0.329	0.000	0.000	0.000
	OME_5	0.000	0.000	0.010	0.132	0.001	0.000	0.000
	OME_6	0.000	0.000	0.003	0.039	0.000	0.000	0.000
mass flow rate / kg/h		0.78	6.98	6.98	0.58	6.17	6.20	0.30

without any decrease in adsorption capacity due to regeneration.

When the feed composition (i.e., the composition of Stream 1) is fixed, only one degree of freedom remains, namely the time the adsorption column is on stream. This time between was varied 97 and 247 min in four steps to explore the impact of the adsorption step on key process parameters as the recycle-to-feed ratio or the overall mass fraction of water in Stream 7.

Table 12 presents the mass balance for one of the simulated operating points corresponding to a time-on-stream of the adsorption column of 197 min. Analogous tables for the remaining three operating points are given in the Appendix C.4.

In Figure 27, the relationships among the recycle-to-feed ratio ($\frac{\dot{m}^{(6)}}{\dot{m}^{(1)}}$), the overall mass fraction of water in Stream 7 ($\tilde{w}_{\mathrm{WA}}^{(7)}$), and the overall mass fraction of water in Stream 6 ($\tilde{w}_{\mathrm{WA}}^{(6)}$) are depicted. A trade-off emerges between the selectivity of the adsorption step towards water and the recycle-to-feed ratio of the process.

At low times-on-stream of the adsorption column, the recycle-to-feed ratio is small, resulting in a poor overall mass fraction of water in Stream 7 (< 0.4 g/g). This implies lower recycle costs but considerable organic losses and the necessity of further purification of Stream 7. The recycle-to-feed ratio of the process cannot be arbitrarily low but presents a lower limit, which is dictated by the chemical equilibrium [30]. In contrast, higher times-on-stream of the adsorption column lead to increased recycle-to-feed ratios and higher overall mass fractions of water in Stream 7 (> 0.9 g/g). The upper limit of

Table 12: Stream table of the operating point 3 in the water-tolerant OME_{3-5} process by Schmitz et al. [24] including the adsorptive step. Time-on-stream of the adsorption column = 197 min.

		stream number						
		1	2	3	4	5	6	7
overall mass fractions /g/g	FA	0.560	0.191	0.144	0.000	0.154	0.156	0.061
	ME	0.340	0.161	0.132	0.000	0.141	0.144	0.023
	WA	0.100	0.043	0.051	0.000	0.055	0.038	0.916
	OME_1	0.000	0.426	0.426	0.000	0.457	0.466	0.000
	OME_2	0.000	0.162	0.162	0.000	0.174	0.178	0.000
	$OME_{\geq 3}$	0.000	0.017	0.085	1.000	0.018	0.019	0.000
mass flow rate / kg/h		0.092	1.073	1.073	0.073	1.000	0.981	0.020

the overall mass fraction of water in Stream 7 is however not arbitrary but given by the adsorption equilibrium at feed conditions, cf. Equation (32). The selected design point should strike a balance among these factors.

From Tables 11 and 12, it can be seen that the use of adsorption allows obtaining much higher overall mass fractions of water in Stream 7 than pervaporation in a single stage. This observation can be confirmed by examining the separation factors $\alpha_{WA,j}$ for pervaporation and adsorption, cf. Sections 2.4.3.2 and 3.4.1. However, although adsorption allows for higher water enrichment in Stream 7, the maximum achievable overall mass fraction of water in Stream 7 by adsorption at the studied feed conditions is around 0.92 g/g. Thus, further purification of this stream remains necessary to minimize the organic losses in Stream 7. In Chapter 3, simulation results demonstrate that a distillative separation of the pervaporation unit's permeate stream can yield a product with an overall mass fraction of water exceeding 0.9999 g/g. The same concept could be applied for the adsorption unit. The comparison may be however premature, as there is still potential for improvement in the membrane material. Ultimately, the decision between adsorption and pervaporation in the water-tolerant OME_{3-5} process by Schmitz et al. should rely on an economic assessment that considers the further purification of the water-rich product from the water separation step as well as the regeneration process in the case of adsorption.

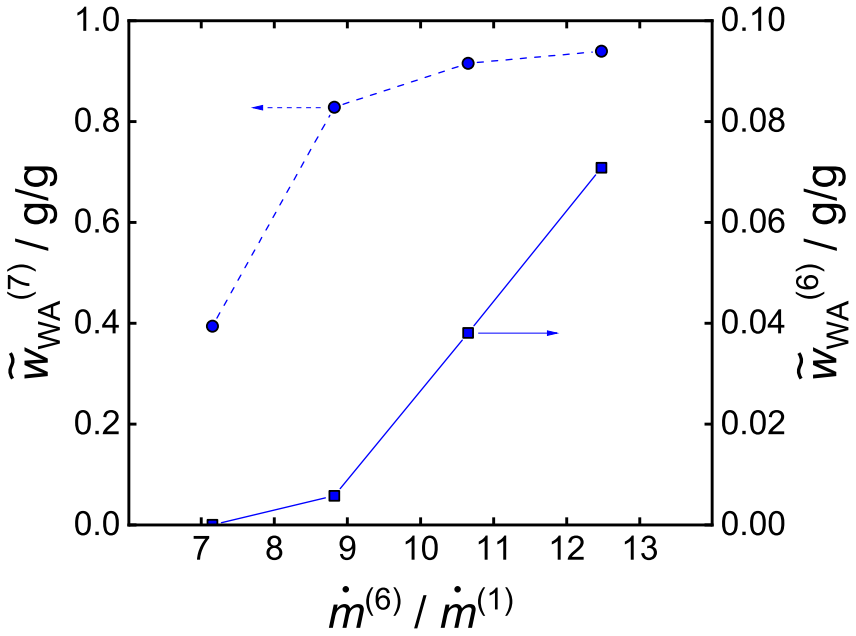

Figure 27: Overall mass fraction of water in Stream 6 and 7 as a function of the recycle-to-feed ratio for the four operating points simulated.

5 Conclusion

Adsorption isotherms of formaldehyde, water and methanol on molecular sieves 3A were measured at two temperatures. A model, which simultaneously considers the physical adsorption equilibrium and the chemical equilibrium occurring in the liquid bulk phase, was successfully regressed to measurements. Formaldehyde undergoes chemical reactions with water and methanol in the liquid phase, forming oligomers. It was found that these reactions have to be considered to describe the temperature dependency of the adsorption equilibrium in a thermodynamically consistent manner. Although formaldehyde is bound mainly to oligomers and is barely present in its molecular form in the liquid bulk phase, it shows appreciable adsorption in the order of magnitude that is observed for water and methanol. While the molecular sieves 3A show a clear selectivity for water over methanol, the selective separation of water from formaldehyde is only possible, if at all, at low temperatures. These results are key for the design of adsorptive processes for drying mixtures containing methanol or formaldehyde. Additionally, the densities of liquid methanolic formaldehyde solutions were measured and correlated at 22 °C and 40 °C.

The equilibrium experiments in the system (formaldehyde + methanol + water + OME_n) confirmed that the equilibrium model yields reasonable predictions for water and formaldehyde adsorption when OME_n are present. The model slightly overestimates the adsorption of methanol, but this deviation may be due to limitations in accurately detecting subtle concentration changes of methanol during the adsorption process. No significant adsorption of OME_n was measured.

Continuous experiments in a packed bed column revealed the dynamic behaviour of the system. The developed column model accurately describes breakthrough curves for formaldehyde, methanol, and water. The selectivity towards water is evident through remarkable separation factors and achieving high overall mass fractions of water, reaching up to 0.908 g/g within the adsorbed phase in the studied composition range.

Concerning the regeneration of zeolite 3A, the findings of this work suggest that regeneration at a temperature of 185 °C and a pressure of 100 mbar is feasible, with a decline of around 13% in adsorption capacity after the initial regeneration cycle. Subsequent cy-

cles do not exhibit further decreases in adsorption capacity. Further research is needed to explore the potential for continuous regeneration, including the role of desorption kinetics.

14 pervaporation experiments were carried out. The average separation factors for formaldehyde, methanol, OME_1, and OME_2 ranged from 16 to 28, indicating that it is possible to separate water from these mixtures. However, the selectivity of the membranes towards water was observed to be diminished compared to previously performed screening experiments [33]. In experiments performed under similar conditions, the composition of the permeate did not change across the experiments, indicating a good reproducibility and stability of the membranes.

For the currently available membranes, it is necessary to after-treat the permeate to prevent significant organic losses. A hybrid process combining the membrane separation with multi-stage condensation or distillation processes presents a viable strategy for achieving higher purity in the water product. A process simulation confirmed that distillation of the permeate stream to obtain pure water with a significant recovery is possible. Implementing multiple pervaporation units in series also showed potential for further purification of the permeate. Moving forward, it is imperative to search for process conditions that enhance the selectivity of the SiO_2 membrane towards water. Concurrently, optimization efforts aimed at enhancing membrane properties should be prioritised in future research.

The process units were integrated in a continuous mini-plant at a scale of around 5 tonnes/a to experimentally demonstrate the water-tolerant $OME_{3–5}$ production process by Schmitz et al. [24] with closing recycles. In this process, the distillation column constitutes the most critical operation because of its reactive multicomponent character and the restricted solubility of formaldehyde. A start-up strategy for the distillation column was developed to avoid formaldehyde precipitation in the reboiler. The experiments showed that $OME_{>3}$ can be separated as bottom product in the column from mixtures of formaldehyde, water, methanol, and $OME_{1–2}$ in the distillate. Only very small impurities of around 800 ppm of formaldehyde are present in the bottoms product, which is to be purified in a subsequent distillation column [24]. The experimental results were compared with simulations based on a reactive equilibrium stage model. Good agreement in the temperature and the composition profiles is observed for the majority of the components of the system. Extrapolations from the solid-liquid equilibrium model of Breitkreuz et al. [89] do not exclude precipitation of solid formaldehyde at experimental conditions. However, no solid precipitation was found in the experiment. Besides the individual feasibilities of the reactor, the distillation column, and the pervaporation unit,

the combined operation also confirms the feasibility of the overall process with recycles. No side products were found accumulating in the loop. Also, the scenario where the water separation is accomplished via adsorption was studied via simulation. By simulating several operating points, a trade-off between the selectivity of the adsorption step and the recycle-to-feed ratio of the process was shown. The industrial-scale production of OME_{3-5} from methanolic formaldehyde solutions using the process suggested by Schmitz et al. [24] has become an important step closer.

Literature

[1] "Framing and context" in Global warming of 1.5 ° C: IPCC special report on impacts of global warming of 1.5 ° C above pre-industrial levels in context of strengthening response to climate change, sustainable development, and efforts to eradicate poverty, Cambridge University Press, 2018, pp. 49–92.

[2] Renewable energy directive, 2023. URL: https://energy.ec.europa.eu/topics/renewable-energy/renewable-energy-directive-targets-and-rules/renewable-energy-directive_en, accessed 30-June-2023.

[3] Y. Zhao, T. Li, T. Niu, W. Zheng, Y. Xie, W. E: Performance and emissions of a diesel engine fueled by coal-based diesel fuels and their blends with polyoxymethylene dimethyl ethers, Sci. Rep. 13 (2023).

[4] S. Arias, J. R. Agudelo, A. Ramos, M. Lapuerta: Emissions from a Euro 6 engine using polyoxymethylene dimethyl ethers: Chemical effects vs mapping strategy, Fuel 335 (2023).

[5] J. Liua, Z. Liua, L. Wanga, P. Wang, P. Suna, H. Mab, P. Wua: Effects of PODE/diesel blends on particulate matter emission and particle oxidation characteristics of a common-rail diesel engine, Fuel Process. Technol. 212 (2021).

[6] M. H. artl, K. Gaukel, D. Pélerin, G. Wachtmeister: Oxymethylene ether as potentially CO_2-neutral fuel for clean diesel engines part 1: Engine testing, MTZ worldwide 78 (2017) 52–59.

[7] H. Gu, S. Liu, Y. Wei, X. Liu, X. Zhu, Z. Li: Effects of polyoxymethylene dimethyl ethers addition in diesel on real driving emission and fuel consumption characteristics of a CHINA VI heavy-duty vehicle, Energies 15 (2022).

[8] J. Burger, M. Siegert, E. Ströfer, H. Hasse: Poly(oxymethylene) dimethyl ethers as components of tailored diesel fuel: Properties, synthesis and purification concepts, Fuel 89 (2010) 3315–3319.

[9] S. E. Iannuzzi, C. Barro, K. Boulouchos, J. Burger: Combustion behavior and soot formation/oxidation of oxygenated fuels in a cylindrical constant volume chamber, Fuel 167 (2016) 49–59.

[10] C. F. Breitkreuz, A. Holzer, T. Fuchs, M. Günther, H. Hasse: Miscibility in systems containing (poly(oxymethylene) ethers (OME) + hydrocarbons + water), Fuel. 338 (2023).

[11] S. Mross, S. Schmitt, S. Stephan, K. Münnemann, H. Hasse: Diffusion coefficients in mixtures of poly(oxymethylene) dimethyl ethers with alkanes, Ind. Eng. Chem. Res. 63 (2024).

[12] L. Lautenschütz, D. Oestreich, P. Seidenspinner, U. Arnold, E. Dinjus, J. Sauer: Physico-chemical properties and fuel characteristics of oxymethylene dialkyl ethers, Fuel 173 (2016) 129–137.

[13] C. J. Baranowski, A. M. Bahmanpour, O. Kröcher: Catalytic synthesis of polyoxymethylene dimethyl ethers (OME): A review, App. Catal. B 217 (2017) 407–420.

[14] J. Burger, M. Siegert, E. Ströfer, H. Hasse: Production process for diesel fuel components poly(oxymethylene) dimethyl ethers from methane-based products by hierarchical optimization with varying model depth, Chem. Eng. Res. Des. 91 (2013) 2648–2662.

[15] L. Lautenschütz, D. Oestreich, P. Haltenort, U. Arnold, E. Dinjus, J. Sauer: Efficient synthesis of oxymethylene dimethylethers (OME) from dimethoxymethane and trioxane over zeolites, Fuel Process. Technol. 165 (2017) 27–33.

[16] D. Wang, F. Zhao, G. Zhu, C. Xia: Production of eco-friendly poly(oxymethylene) dimethyl ethers catalyzed by acidic ionic liquid: A kinetic investigation, Chem. Eng. J. 334 (2018) 2616–2624.

[17] P. Haltenort, L. Lautenschütz, U. Arnold, J. Sauer: Transacetalization reactions for the synthesis of oligomeric oxymethylene dialkyl ethers catalyzed by zeolite BEA25, Top. Catal. 62 (2019) 551–559.

[18] R. Peláez, P. Marín, S. Ordóñez: Synthesis of poly(oxymethylene) dimethyl ethers from methylal and trioxane over acidic ion exchange resins: A kinetic study, Chem. Eng. J. 396 (2020).

[19] C. F. Breitkreuz, N. Hevert, N. Schmitz, J. Burger, H. Hasse: Synthesis of methylal and poly(oxymethylene) dimethyl ethers from dimethyl ether and trioxane, Ind. Eng. Chem. Res. 61 (2022) 7810–7822.

[20] M. Drexler, P. Haltenort, U. Arnold, J. Sauer: Continuous synthesis of oxymethylene ether fuels from dimethyl ether in a heterogeneously catalyzed liquid phase process, Chem. Ing. Tech. 94 (2022) 256–266.

[21] M. Drexler, P. Haltenort, U. Arnold, J. Sauer, S. A. Karakoulia, K. S. Triantafyllidis: Progress in the anhydrous production of oxymethylene ethers (OME) as a renewable diesel fuel in a liquid phase process, Catal. Today 424 (2023).

[22] D. Oestreich, L. Lautenschütz, U. Arnold, J. Sauer: Production of oxymethylene dimethyl ethere (OME)-hydrocarbon fuel blends in a one-step synthesis/extraction procedure, Fuel 214 (2018) 39–44.

[23] Z. Han, Y. Ren, H. Li, X. Li, X. Gao: Simultaneous extractive and azeotropic distillation separation processes for production of PODEn from formaldehyde and methylal, Ind. Eng. Chem. Res. 58 (2019) 5252–5260.

[24] N. Schmitz, E. Ströfer, J. Burger, H. Hasse: Conceptual design of a novel process for the production of poly(oxymethylene) dimethyl ethers from formaldehyde and methanol, Ind. Eng. Chem. Res. 56 (2017) 11519–11530.

[25] N. Schmitz, F. Homberg, J. Berje, J. Burger, H. Hasse: Chemical equilibrium of the synthesis of poly(oxymethylene) dimethyl ethers from formaldehyde and methanol in aqueous solutions, Ind. Eng. Chem. Res. 54 (2015) 6409–6417.

[26] N. Schmitz, J. Burger, H. Hasse: Reaction kinetics of the formation of poly(oxymethylene) dimethyl ethers from formaldehyde and methanol in aqueous solutions, Ind. Eng. Chem. Res. 54 (2015) 12553–12560.

[27] N. Schmitz, C. F. Breitkreuz, E. Ströfer, J. Burger, H. Hasse: Vapor-liquid equilibrium and distillation of mixtures containing formaldehdye and poly(oxymethylene) dimethyl ethers, Chem. Eng. Process. 131 (2018) 116–124.

[28] F. Mantei, M. Ouda, A. Schaadt: Verfahren zur Herstellung von Polyoxymethylendimethylethern, 2022.

[29] F. Mantei, C. Schwarz, A. Elwalily, F. Fuchs, A. Pounder, H. Stein, M. Kraume, O. Salem: A novel process towards the industrial realization of large-scale oxymethylene dimethyl ether production - COMET, React. Chem. Eng. (2023).

[30] J. Voggenreiter, A. Ferre, J. Burger: Scale-up of the continuous production of poly(oxymethylene) dimethyl ethers from methanol and formaldehyde in tubular reactors, Ind. Eng. Chem. Res. 61 (2022) 10034–10046.

[31] J. Voggenreiter: Model-based Scale-up of the Continuous Production of Poly(oxymethylene) Dialkyl Ethers, Ph.D. thesis, Technische Universität München, 2022.

[32] N. Schmitz, C. F. Breitkreuz, E. Ströfer, J. Burger, H. Hasse: Separation of water from mixtures containing formaldehyde, water, methanol, methylal and poly(oxymethylene) dimethyl ethers by pervaporation, J. Membr. Sci. 564 (2018) 806–812.

[33] A. Ferre, D. Worch, J. Voggenreiter, U. Lubenau, J. Burger: Dewatering of mixtures containing formaldehyde, methanol, water, and poly(oxymethylene) dimethyl ethers by pervaporation: Membrane screening and mini-plant operation, J. Memb. Sci. 690 (2024).

[34] S. Joshi, J. R. Fair: Adsorptive drying of toulene, Ind. Eng. Chem. Res. 27 (1988) 2078–2085.

[35] S. Joshi, J. R. Fair: Adsorptive drying of hydrocarbon liquids, Ind. Eng. Chem. Res. 30 (1991) 177–185.

[36] Hendriyana, B. H. Prabowo, L. Nurdini, G. Trilaksono: Adsorption of water from methanol solution using various adsorbent, AIP Conference Proceedings 1904 (2017) 020031.

[37] B. Burrichter, C. Pasel, M. Luckas, D. Bathen: Experimental and theoretical study on the adsorptive drying of primary alcohols in a fixed bed adsorber, Sep. Purif. Technol. 145 (2015) 39–49.

[38] C. Pahl, C. Pasel, M. Luckas, D. Bathen: Adsorptive water removal from primary alcohols and acetic acid esters in the ppm-region, J. Chem. Eng. Data 57 (2012) 2465–2471.

[39] W. K. Teo, D. M. Ruthven: Adsorption of water from aqueous ethanol using 3A molecular sieves, Ind. & Eng. Chem. Process Des. Dev. 25 (1986) 17–21.

[40] B. Ambrożek, J. Nastaj, E. Gabruś: Modeling and experimental studies of adsorptive dewatering of selected aliphatic alcohols in temperature swing adsorption system, Dry. Technol. 31 (2013) 1780–1789.

[41] B. Ambrożek, J. Nastaj, E. Gabruś: Modeling of adsorptive drying of n-propanol, Dry. Technol. 30 (2012) 1072–1080.

[42] B. Burrichter, C. Pasel, M. Luckas, D. Bathen: Parameter study on the adsorptive drying of isopropanol in a fixed bed adsorber, Sep. Purif. Technol. 132 (2014) 736–743.

[43] A. K. Jain, A. K. Gupta: Adsorptive drying of isopropyl alcohol on 4A molecular sieves: Equilibrium and kinetic studies, Sep. Sci. Tech. 29 (1994) 1461–1472.

[44] B. A. V. Santos, V. M. T. M. Silva, J. M. Loureiro, A. E. Rodrigues: Adsorption of H_2O and dimethyl carbonate at high pressure over zeolite 3A in fixed bed column, Ind. Eng. Chem. Res. 53 (2014) 2473–2483.

[45] H. Hasse: Dampf-Flüssigkeits-Gleichgewichte, Enthalpien und Reaktionskinetik in formaldehydhaltigen Mischungen, Ph.D. thesis, Technische Universität Kaiserslautern, 1990.

[46] E. M. Carter, L. E. Katz, G. Speitel, Jr, D. Ramirez: Gas-phase formaldehyde adsorption isotherm studies on activated carbon: Correlations of adsorption capacity to surface functional group density, Environ. Sci. Technol. 45 (2011) 6498–6503.

[47] J.-P. Bellat, G. Weber, I. Bezverkhyy, J.-F. Lamonier: Selective adsorption of formaldehyde and water vapors in NaY and NaX zeolites, Microporous Mesoporous Mater. 288 (2019) 1387–1811.

[48] L. Novikova, D. S. Bogdanov, L. I. Belchinskaya, D. Kolousek, B. Doushova, M. Lhotka, G. A. Petukhova: Adsorption of formaldehyde from aqueous solutions using metakaolin-based geopolymer sorbents, Prot. Met. Phys. Chem. Surf. 55 (2019) 864–871.

[49] B. Bettens, S. Dekeyzer, B. van der Bruggen, J. Degrève, C. Vandecasteele: Transport of pure components in pervaporation through a microporous silica membrane, J. Phys. Chem. B 109 (2005) 5216–5222.

[50] F. J. Alguacil, F. A. López: On the active adsorption of chromium(iii) from alkaline solutions using multiwalled carbon nanotubes, Appl. Sci. 10 (2020) 1–10.

[51] M. Simo, S. Sivashanmugam, C. J. Brown, V. Hlavacek: Adsorption/desorption of water and ethanol on 3A zeolite in near-adiabatic fixed bed, Ind. Eng. Chem. Res. 48 (2009) 9247–9260.

[52] J. Voggenreiter, J. Burger: Side products in the water-tolerant synthesis of poly(oxymethylene) dimethyl ethers: Formation kinetics and implications for process design, Ind. Eng. Chem. Res. 60 (2021) 2418–2429.

[53] M. Yu, J. L. Falconer, R. D. Noble: Adsorption of liquid mixtures on silicalite-1 zeolite: a density-bottle method, Langmuir 21 (2005) 7390–7397.

[54] Z. Song, Y. Huang, W. L. Xu, L. Wang, Y. Bao, S. Li, M. Yu: Continuously adjustable, molecular-sieving gate on 5A zeolite for distinguishing small organic molecules by size, Sci. Rep. 5 (2015) 1–7.

[55] J. G. M. Winkelman, A. A. C. M. Beenackers: Correlations for the density and viscosity of aqueous formaldehyde solutions, Ind. Eng. Chem. Res. 39 (2000) 557–562.

[56] J.-O. Drunsel, M. Renner, H. Hasse: Experimental study and model of reaction kinetics of heterogeneously catalyzed methylal synthesis, Chem. Eng. Res. Des. 90 (2012) 696–703.

[57] I. Hahnenstein, M. Albert, H. Hasse, C. G. Kreiter, G. Maurer: NMR spectroscopic and densimetric study of reaction kinetics of formaldehyde polymer formation in water, deuterium oxide, and methanol, Ind. Eng. Chem. Res. 34 (1995) 440–450.

[58] R. Duarte Silva, I. S. Monteiro, T. de Camargo Chaparro, R. S. Hardt, R. Giudici, A. Barros-Timmons, E. Bourgeat-Lami, A. M. dos Santos: Investigation of the adsorption of amphipathic macroraft agents onto montmorillonite clay, Langmuir 33 (2017) 9598–9608.

[59] R. Pelech, A. Bembnowska, E. Milchert: Adsorption of hydrocarbon chloroderivatives onto dto commercial activated carbon from multi-component aqueous solutions, Adsorpt. Sci. Technol. 8 (2003) 707–720.

[60] H. O. Rubiera Landa: Development of an efficient method for simulating fixed-bed adsorption dynamics using Ideal Adsorbed Solution Theory, Ph.D. thesis, Otto-von-Guericke-Universität Magdeburg, 2016.

[61] C. Kuhnert, M. Albert, S. Breyer, I. Hahnenstein, H. H. G. Maurer: Phase equilibrium in formaldehyde containing multicomponent mixtures: Experimental results for fluid phase equilibria of (formaldehyde + (water or methanol) + methylal)) and (formaldehyde + water + methanol + methylal) and comparison with predictions, Ind. Eng. Chem. Res. 45 (2006) 5155–5164.

[62] D. Bathen, M. Breitbach: Adsorptionstechnik, 2001.

[63] J. B. Butt: Reaction Kinetics and Reactor Design, Prentice-Hall, 1980.

[64] B. J. Mair, J. W. Westhaver, F. D. Rossini: Theoretical analysis of fractionating process of adsorption, Ind. Eng. Chem. Res. 42 (1950) 1279–1286.

[65] C. N. Rowe, R. W. Schiessler: Adsorption separation factors and selective adsorbent capacities of some binary liquid hydrocarbon mixtures, J. Phys. Chem. 70 (1966) 787–797.

[66] Least Absolute Deviation Regression, Springer New York, New York, NY, 2008, pp. 299–302. URL: https://doi.org/10.1007/978-0-387-32833-1_225. doi:10.1007/978-0-387-32833-1_225.

[67] P. Shukla, K. Dong, V. Rudolph, S. K. Bhatia, H. C. Bajaj, R. V. Jasra: Adsorptive dehydration of ethanol using 3A zeolite: an evaluation of transport behaviour in a two-phase zeolite pellet, Adsorption 25 (2019) 1611–1623.

[68] T. Yamamoto, Y. H. Kim, B. C. Kim, A. Endo, N. Thongprachan, T. Ohmori: Adsorption characteristics of zeolites for dehydration of ethanol: Evaluation of diffusivity of water in porous structure, Chem. Eng. J. 181–182 (2012) 443–448.

[69] Molecular sieves 3A, 2020. URL: https://www.carlroth.com/com/en/molecular-sieves/molecular-sieve-3-%C3%A5/p/8487.1.

[70] B. Magnusson, U. Örnemark (Eds.): The Fitness for Purpose of Analytical Methods: A Laboratory Guide to Method Validation and Related Topics, 2 ed., Eurachem, 2014.

[71] L. Credali, L. Mortillaro, G. Galiazzo, M. Russo, C. de Checchi: Pressione di vapore sul sistema H_2O-CH_2O liquido e solido, Chim. Ind. 47 (1965) 732–735.

[72] C. F. Breitkreuz, J. Burger, H. Hasse: Solid-liquid equilibria and kinetic of the solid formation in binary and ternary mixtures containing (formaldehyde + water + methanol), Ind. Eng. Chem. Res. 61 (2022) 1871–1884.

[73] M. J. Carmo, J. C. Gubulin: Ethanol-water adsorption on commercial 3A zeolites: kinetic and thermodynamic data, Braz. J. Chem. Eng. 14 (1997) 217–224.

[74] E. Lalik, R. Mirek, J. Rakoczy, A. Groszek: Microcalorimetric study of sorption of water and ethanol in zeolites 3A and 5A, Catal. Today 114 (2006) 242–247.

[75] E. Gabruś, J. Nastaj, P. Tabero, T. Aleksandrzak: Experimental studies on 3A and 4A zeolite molecular sieves regeneration in TSA process: Aliphatic alcohols dewateringâwater desorption, Chem. Eng. J. 259 (2015) 232–242.

[76] B. Smitha, D. Suhanya, S. Sridhar, M. Ramakrishna: Separation of organic-organic mixtures by pervaporation - a review, J. Mem. Sci. 241 (2004) 1–21.

[77] E. Carretier, P. Moulin, M. Beaujean, F. Charbit: Purification and dehydration of methylal by pervaporation, J. Mem. Sci. 217 (2003) 159–171.

[78] R. Jiraratananon, A. Chanachai, R. Y. M. Huang, D. Uttapap: Pervaporation dehydration of ethanolâwater mixtures with chitosan/hydroxyethylcellulose (CS/HEC) composite membranes I. Effect of operating conditions, J. Membr. Sci. 195 (2002) 143–151.

[79] R. Castro-Muñoz, J. Buera-González, Óscar de la Iglesia, F. Galiano, V. Fíla, M. Malankowska, C. Rubio, A. Figoli, C. Téllez, J. Coronas: Towards the dehydration of ethanol using pervaporation cross-linked poly(vinyl alcohol)/graphene oxide membranes, J. Mem. Sci. 582 (2019) 423–434.

[80] V. T. Magalad, G. S. Gokavi, K. Raju, T. M. Aminabhavi: Mixed matrix blend membranes of poly(vinyl alcohol)-poly(vinyl pyrrolidone) loaded with phosphomolybdic acid used in pervaporation dehydration of ethanol, J. Membr. Sci. 354 (2010) 150–161.

[81] D. Shah, K. Kissick, A. Ghorpade, R. Hannah, D. Bhattacharyya: Pervaporation of alcoholâwater and dimethylformamideâwater mixtures using hydrophilic zeolite naa membranes: mechanisms and experimental results, J. Mem. Sci. 179 (2000) 185–205.

[82] D. Unlu: High-efficiency pervaporative separation of fuel bioadditive methylal from methanol by poly(vinyl alcohol)/poly(vinylpyrrolidone) blend membrane, Braz. J. Chem. Eng. 40 (2023) 257–268.

[83] M. Ott, H. Schoenmakers, H. Hasse: Distillation of formaldehyde containing mixtures: laboratory experiments, equilibrium stage modeling and simulation, Chem. Eng. Process. 44 (2005) 687–694.

[84] M. Dyga, A. Keller, H. Hasse: Distillation behavior of the system (formaldehyde + water + isoprenol), Chem. Eng. Sci. 263 (2022).

[85] H. Li, C. Wu, Q. Zhang, X. Li, X. Gao: Synthesis of 1,3-dioxolane from aqueous formaldehyde solution and ethylene glycol: Kinetics and reactive distillation, Ind. Eng. Chem. Res. 58 (2019) 7025–7036.

[86] A. Hasabnis, S. Mahajani: Acetalization of glycerol with formaldehyde by reactive distillation, Ind. Eng. Chem. Res. 53 (2014) 12279–12287.

[87] A. K. Kolah, S. M. Mahajani, M. M. Sharma: Acetalization of formaldehyde with methanol in batch and continuous reactive distillation columns, Ind. Eng. Chem. Res. 35 (1996) 3707–3720.

[88] M. Ott, H. Schoenmakers, H. Hasse: Development of an integrated reaction-distillation process for the production of methylal, Ind. Eng. Chem. Res. 56 (2017) 575–582.

[89] C. F. Breitkreuz, J. Burger, H. Hasse: Solubility of formaldehyde in mixtures of water + methanol + poly(oxymethylene) dimethyl ethers, Fluid Phase Equilib. 565 (2023).

[90] S. C. LTD: Structured packings for distillation, absorption and reactive distillation, 2011.

[91] Oxymethylene ether DIN/TS 51699, 2023. URL: `https://asg-analytik.de/en/analytics/liquid-fuels3/ome`.

[92] N. Schmitz: Production of poly(oxymethylene) dimethyl ethers from formaldehyde and methanol, Ph.D. thesis, Technische Universität Kaiserslautern, 2018.

[93] S. H. Madani, A. Badalyan, M. J. Biggs, P. Pendleton: Uncertainty in pore size distribution derived from adsorption isotherms: I. classical methods, Microporous Mesoporous Mat. 214 (2015) 210–216.

[94] D. Himmel, R. J. White, E. Jacob, I. Krossing: Highly correlated: Ab initio thermodynamics of oxymethylene dimethyl ethers (OME): Formation and extension to the liquid phase, Sustain. Energy Fuels 1 (2017) 1177–1183.

[95] A. Hauer: Beurteilung fester Adsorbentien in offenen Sorptionssystemen für energetische Anwendungen, Ph.D. thesis, Technische Universität Berlin, 2002.

Appendix

A Water Separation via Adsorption

A.1 Mathematic Relations between True and Overall Mass Fractions

The overall masses $\tilde{m}_i$ are calculated from the true amounts of substance n_i and the molar masses M_i[92]:

$$\tilde{m}_{\mathrm{FA}} = \left(n_{\mathrm{FA}} + \sum_{i=1}^{\infty} i \cdot n_{\mathrm{MG}_i} + \sum_{i=1}^{\infty} i \cdot n_{\mathrm{HF}_i}\right) \cdot M_{\mathrm{FA}} \tag{53}$$

$$\tilde{m}_{\mathrm{WA}} = \left(n_{\mathrm{WA}} + \sum_{i=1}^{\infty} n_{\mathrm{MG}_i}\right) \cdot M_{\mathrm{WA}} \tag{54}$$

$$\tilde{m}_{\mathrm{ME}} = \left(n_{\mathrm{ME}} + \sum_{i=1}^{\infty} n_{\mathrm{HF}_i}\right) \cdot M_{\mathrm{ME}} \tag{55}$$

The total overall mass $\tilde{m}_{\mathrm{tot}}$ is given by:

$$\tilde{m}_{\mathrm{tot}} = \tilde{m}_{\mathrm{FA}} + \tilde{m}_{\mathrm{ME}} + \tilde{m}_{\mathrm{WA}} \tag{56}$$

The overall mass fractions $\tilde{w}_i$ are given by:

$$\tilde{w}_i = \frac{\tilde{m}_i}{\tilde{m}_{\mathrm{tot}}} \tag{57}$$

A.2 Parameters for the Chemical Equilibrium Constants

Table 13 lists the parameter values for A_j and B_j to calculate the chemical equilibrium constant based on mole fractions K_j^{chem} of Reaction (9) - (12).

Table 13: Parameters for the calculation of the chemical equilibrium constants based on mole fractions K_j^{chem} using the correlation $\ln K_j^{\text{chem}} = A_j + \frac{B_j}{T}$ [57].

reaction	A_j	B_j
(9)	-2.325	2579
(10) ($n = 2$)	-2.311	3140
(10) ($n > 2$)	-2.433	3039
(11)	-1.902	3512
(12)	-2.250	3009

A.3 Propagation of Uncertainty

Since $\tilde{q}_{\mathrm{e},i}$ is determined as a function of many variables according to Equation (7) in in Section 2.2.5, the experimental uncertainty associated to the measurements is obtained by the formula [93]:

$$\Delta\tilde{q}_{\mathrm{e},i} = \Bigg[\left(\frac{\partial \tilde{q}_{\mathrm{e},i}}{\partial m_{\mathrm{liq}}^{\mathrm{feed}}} \cdot \Delta m_{\mathrm{liq}}^{\mathrm{feed}} \right)^2 + \left(\frac{\partial \tilde{q}_{\mathrm{e},i}}{\partial \tilde{w}_i^{\mathrm{feed}}} \cdot \Delta \tilde{w}_i^{\mathrm{feed}} \right)^2 + \left(\frac{\partial \tilde{q}_{\mathrm{e},i}}{\partial m_{\mathrm{liq}}^{\mathrm{rem}}} \cdot \Delta m_{\mathrm{liq}}^{\mathrm{rem}} \right)^2 + \left(\frac{\partial \tilde{q}_{\mathrm{e},i}}{\partial V_{\mathrm{flask}}} \cdot \Delta V_{\mathrm{flask}} \right)^2 + \left(\frac{\partial \tilde{q}_{\mathrm{e},i}}{\partial m_{\mathrm{ads}}} \cdot \Delta m_{\mathrm{ads}} \right)^2 + \left(\frac{\partial \tilde{q}_{\mathrm{e},i}}{\partial \rho_{\mathrm{ads}}} \cdot \Delta \rho_{\mathrm{ads}} \right)^2 + \left(\frac{\partial \tilde{q}_{\mathrm{e},i}}{\partial \tilde{w}_i} \cdot \Delta \tilde{w}_i \right)^2 + \left(\frac{\partial \tilde{q}_{\mathrm{e},i}}{\partial \rho_{\mathrm{liq}}} \cdot \Delta \rho_{\mathrm{liq}} \right)^2 \Bigg]^{\frac{1}{2}} \tag{58}$$

For this, the partial derivatives of $\tilde{q}_{\mathrm{e},i}$ are needed. These derivatives are calculated from Equation (7) in Section 2.2.5:

$$\frac{\partial \tilde{q}_{\mathrm{e},i}}{\partial m_{\mathrm{liq}}^{\mathrm{feed}}} = \frac{\tilde{w}_i^{\mathrm{feed}}}{m_{\mathrm{ads}}} \tag{59}$$

$$\frac{\partial \tilde{q}_{\mathrm{e},i}}{\partial \tilde{w}_i^{\mathrm{feed}}} = \frac{m_{\mathrm{liq}}^{\mathrm{feed}}}{m_{\mathrm{ads}}} \tag{60}$$

$$\frac{\partial \tilde{q}_{\mathrm{e},i}}{\partial m_{\mathrm{liq}}^{\mathrm{rem}}} = \frac{\tilde{w}_i}{m_{\mathrm{ads}}} \tag{61}$$

$$\frac{\partial \tilde{q}_{\mathrm{e},i}}{\partial V_{\mathrm{flask}}} = \frac{\rho_{\mathrm{liq}} \cdot \tilde{w}_i}{m_{\mathrm{ads}}} \tag{62}$$

$$\frac{\partial \tilde{q}_{\mathrm{e},i}}{\partial m_{\mathrm{ads}}} = \frac{\frac{\rho_{\mathrm{liq}} \cdot \tilde{w}_i}{\rho_{\mathrm{ads}}} \cdot m_{\mathrm{ads}} - \tilde{q}_{\mathrm{e},i}}{{m_{\mathrm{ads}}}^2} \tag{63}$$

$$\frac{\partial \tilde{q}_{\mathrm{e},i}}{\partial \rho_{\mathrm{ads}}} = \frac{-\rho_{\mathrm{liq}} \cdot \tilde{w}_i}{{\rho_{\mathrm{ads}}}^2} \tag{64}$$

$$\frac{\partial \tilde{q}_{\mathrm{e},i}}{\partial \tilde{w}_i} = \frac{m_{\mathrm{liq}}^{\mathrm{rem}} - (V_{\mathrm{flask}} - \frac{m_{\mathrm{ads}}}{\rho_{\mathrm{ads}}}) \cdot \rho_{\mathrm{liq}}}{m_{\mathrm{ads}}} \tag{65}$$

$$\frac{\partial \tilde{q}_{\mathrm{e},i}}{\partial \rho_{\mathrm{liq}}} = \left(V_{\mathrm{flask}} - \frac{m_{\mathrm{ads}}}{\rho_{\mathrm{ads}}}\right) \cdot \frac{\tilde{w}_i}{m_{\mathrm{ads}}} \tag{66}$$

The uncertainties of all involved variables are known or estimated as follows: $\Delta m_{\mathrm{liq}}^{\mathrm{feed}} = \Delta m_{\mathrm{ads}} = 0.0008$ g, $\Delta \rho_{\mathrm{ads}} = 0.01$ g/cm^3, $\frac{\Delta \tilde{x}_i^{\mathrm{feed}}}{\tilde{x}_i^{\mathrm{feed}}} = \frac{\Delta \tilde{x}_i}{\tilde{x}_i} = 0.02$, $\Delta V_{\mathrm{flask}} = 1$ cm^3, $\Delta m_{\mathrm{liq}}^{\mathrm{rem}} = 0.0008$ g, and $\Delta \rho_{\mathrm{liq}} = 0.0001$ g/cm^3.

Each experimental point $\tilde{q}_i^{(k)}$ is the arithmetic mean of $m \leq 3$ repetitions:

$$\tilde{q}_i^{(k)} = \frac{\sum_{j=1}^{m} \tilde{q}_{i_j}^{(k)}}{m} \tag{67}$$

For each repetition j, the uncertainty is calculated with the formulas detailed above. Then, the length of the error bar of the experimental point k is obtained as:

$$\sigma_k = \sigma_k^+ - \sigma_k^- \tag{68}$$

where

$$\sigma_k^+ = \min_{1 \leq j \leq m} \left\{\tilde{q}_{i_j}^{(k)} + \Delta \tilde{q}_{i_j}^{(k)}\right\} \tag{69}$$

$$\sigma_k^- = \max_{1 \leq j \leq m} \left\{\tilde{q}_{i_j}^{(k)} - \Delta \tilde{q}_{i_j}^{(k)}\right\} \tag{70}$$

A.4 Mass Balance of the Adsorption Column

In the following, the detailed derivation of the mass balance of the adsorption column (Equation (20) in Section 2.3.3.1) is provided.

A differential element of the fluid phase of length $\mathrm{d}z$ and mass $\mathrm{d}m$ in a column packed with the adsorbent is considered. In the mass balance of the component i, the accumulation term $\frac{\partial m_i}{\partial t}$ is related to the convective mass flow $\dot{m}_i^{\mathrm{conv}}$, the dispersive mass flow $\dot{m}_i^{\mathrm{disp}}$ and the adsorptive mass flow $\dot{m}_i^{\mathrm{ads}}$ [62]:

$$\frac{\partial m_i}{\partial t} = \dot{m}_i^{\mathrm{conv}}(z) - \dot{m}_i^{\mathrm{conv}}(z+\mathrm{d}z) + \dot{m}_i^{\mathrm{disp}}(z) - \dot{m}_i^{\mathrm{disp}}(z+\mathrm{d}z) - \mathrm{d}\dot{m}_i^{\mathrm{ads}} \tag{71}$$

Through a Taylor series expansion, Equation (71) is rewritten as Equation (72)[62]:

$$\frac{\partial m_i}{\partial t} = -\frac{\partial \dot{m}_i^{\mathrm{conv}}}{\partial z}\mathrm{d}z - \frac{\partial \dot{m}_i^{\mathrm{disp}}}{\partial z}\mathrm{d}z - \mathrm{d}\dot{m}_i^{\mathrm{ads}} \tag{72}$$

The accumulation in the considered differential element is calculated using Equation (73). The convective material transport can be described as in Equation (74). The dispersion term is presented in Equation (75). The final term of the equation can be replaced by Equation (76) [62].

$$\frac{\partial m_i}{\partial t} = \epsilon \cdot A \cdot \mathrm{d}z \cdot \frac{\partial c_i}{\partial t} = \epsilon \cdot A \cdot \frac{\rho_{\mathrm{l}}}{M_i}\mathrm{d}z \cdot \frac{\partial \tilde{w}_i}{\partial t} \tag{73}$$

$$\frac{\partial \dot{m}_i^{\mathrm{conv}}}{\partial z} = \dot{V} \cdot \frac{\partial c_i}{\partial z} + c_i \cdot \frac{\partial \dot{V}}{\partial z} = \frac{\dot{m}}{M_i} \cdot \frac{\partial \tilde{w}_i}{\partial z} + \frac{\tilde{w}_i}{M_{\mathrm{i}}} \cdot \frac{\partial \dot{m}}{\partial z} \tag{74}$$

$$\frac{\partial \dot{m}_i^{\mathrm{disp}}}{\partial z} = D_{\mathrm{ax}} \cdot \epsilon \cdot A \cdot \frac{\partial^2 c_i}{\partial z^2} = D_{\mathrm{ax}} \cdot \epsilon \cdot A \cdot \frac{\rho_{\mathrm{l}}}{M_i} \cdot \frac{\partial^2 \tilde{w}_i}{\partial z^2} \tag{75}$$

$$-\mathrm{d}\dot{m}_i^{\mathrm{ads}} = (1-\epsilon) \cdot A \cdot \frac{\rho_{\mathrm{ads}}}{M_i} \cdot \mathrm{d}z \cdot \frac{\partial q_i}{\partial z} \tag{76}$$

By substituting Equations (73) through (76) into Equation (72), Equation (20) from Section 2.3.3.1 is obtained:

$$\begin{aligned} &- \frac{\dot{m}}{A_{\mathrm{K}}} \cdot \frac{\partial \tilde{w}_i}{\partial z} - \frac{\tilde{w}_i}{A_{\mathrm{K}}} \cdot \frac{\partial \dot{m}}{\partial z} = \\ &\epsilon \cdot \rho_{\mathrm{liq}} \cdot \frac{\partial \tilde{w}_i}{\partial t} + (1-\epsilon) \cdot \rho_{\mathrm{ads}} \cdot \frac{\partial \tilde{q}_i}{\partial t} - D_{\mathrm{ax}} \cdot \rho_{\mathrm{liq}} \cdot \epsilon \cdot \frac{\partial^2 \tilde{w}_i}{\partial z^2} \end{aligned} \tag{77}$$

A.5 Calculation of the Adiabatic Temperature Increase

Table 14 summarizes the main parameters and their numerical values required for the calculation of the temperature increase under adiabatic conditions in experiment C2. First, the equilibrium loadings of formaldehyde, methanol and water at the feed composition are multiplied by the mass of zeolite to obtain the adsorbed masses m_i^{ads} of each component i. Using the specific adsorption enthalpies $\Delta H_i^{\mathrm{ads}}$, the enthalpy change caused by each component can be computed. These enthalpy changes are then summed up to obtain the total enthalpy change due to adsorption ΔH^{ads}.

Table 14: Main parameters required for the calculation of the temperature increase under adiabatic conditions corresponding to the experiment C2.

	$\tilde{w}_i^{\mathrm{Feed}}$ / g/g	m_i^{ads} / g	$\Delta H_i^{\mathrm{ads}}$ / kJ	$c_{\mathrm{p},i}$ / kJ / (kg K)
formaldehyde	0.150	1.2	0.56	1167
water	0.038	51.8	67.29	4200
methanol	0.121	0.3	0.01	2500

The heat capacity of the mixture is calculated from the heat capacities of the individual components, $c_{\mathrm{p},i}$, which are obtained from the work of Himmel et al. [94] The mass m_i of each component that is heated up is calculated from the feed flow rate and the time it took to reach approximately equilibrium loading. This time was assumed to be 110 minutes. Additionally, for the zeolite 3A, a heat capacity of $c_{\mathrm{p,ads}} = 850$ J/(kg K) was assumed [95].

By substituting these values into Equation (78), the maximum temperature increase under adiabatic conditions $\Delta T_{\mathrm{adiab}}$ can be calculated:

$$\Delta T_{\mathrm{adiab}} = \frac{\Delta H^{\mathrm{ads}}}{\sum c_{\mathrm{p},i} \cdot m_i + c_{\mathrm{p,ads}} \cdot m_{\mathrm{ads}}} \tag{78}$$

A.6 Model Based on True Mass Fractions

In this section, the model based on the true mass fraction is presented. For formaldehyde, methanol and water, the specific overall adsorbed mass is modeled by:

$$\tilde{q}_{\mathrm{e},i} = \frac{q_{\mathrm{m},i} \cdot K_i^{\mathrm{ads}} \cdot w_i}{1 + K_{\mathrm{FA}}^{\mathrm{ads}} \cdot w_{\mathrm{FA}} + K_{\mathrm{ME}}^{\mathrm{ads}} \cdot w_{\mathrm{ME}} + K_{\mathrm{WA}}^{\mathrm{ads}} \cdot w_{\mathrm{WA}}} \; ; i = \mathrm{FA}, \mathrm{ME}, \mathrm{WA} \tag{79}$$

For water and 2-propanol, the equilibrium loading is modelled by:

$$q_{\mathrm{e,WA}} = \frac{q_{m,\mathrm{WA}} \cdot K_{\mathrm{WA}}^{\mathrm{ads}} \cdot w_{\mathrm{WA}}}{1 + K_{\mathrm{WA}}^{\mathrm{ads}} \cdot w_{\mathrm{WA}}} \tag{80}$$

The methodology to determine the model parameters is analogous to the case of the activity-based model described in Section 2.3.5. The values of the fitted parameters are presented in Table 15.

Table 15: Adjusted model parameters at 22 °C and 40 °C.

	$q_{\mathrm{m},i}$ / g/g		K_i^{ads}	
	22 °C	40 °C	22 °C	40 °C
formaldehyde	0.097	0.177	$6.94 \cdot 10^5$	$3.90 \cdot 10^5$
methanol	0.121	0.120	151.44	149.73
water	0.182	0.181	3878.26	1982.63

A.7 Densities of Methanolic Formaldehyde Solutions

Table 16 presents the densities of liquid methanolic solutions of formaldehyde at 22 °C and 40 °C.

Table 16: Experimental densities of liquid methanolic formaldehyde solutions at 22 °C and 40 °C (cf. Figure 4).

T / °C	$\tilde{w}_{\mathrm{FA}}$ / g/g	ρ_{liq} / g/cm^3
22	0	0.7895
	0.112	0.8317
	0.122	0.8361
	0.425	0.9687
	0.530	1.0248
40	0	0.7733
	0.187	0.8436
	0.190	0.8439
	0.244	0.8700
	0.377	0.9335
	0.413	0.9484

A.8 Numerical Data of Experiments Z1 - Z4

Table 17 provides the numerical results of the experiments Z1 - Z4 used to determine the density of the adsorbent. For each experiment, the mass of adsorbent used, the initial mass of liquid, the mass of liquid removed and the resulting adsorbent density are given.

Table 17: Densities of liquid methanolic formaldehyde solutions at 22 °C and 40 °C (cf. Figure 4).

experiment	repetition	m_{ads} / g	$m_{\text{liq}}^{\text{feed}}$ / g	$m_{\text{liq}}^{\text{rem}}$ / g	ρ_{ads} / g/cm^3
Z1	I	17.765	32.611	0.838	1.816
	II	17.238	32.567	0.588	1.811
	III	14.673	34.220	1.137	1.806
Z2	I	15.964	34.039	0.929	1.810
	II	19.926	32.158	0.819	1.808
Z3	I	20.088	31.073	0.716	1.813
	II	12.476	35.417	1.736	1.831
	III	5.310	38.473	1.734	1.831
Z4	I	19.958	32.654	1.825	1.818
	II	20.199	30.974	0.337	1.800
	III	20.352	31.835	1.142	1.826

A.9 Numerical Data of Experiments B1 - B40a

Tables 18,19, 20, and 21 present the numerical data of the experiments B1 - B40a.

Table 18: Overall composition of the liquid phase in equilibrium for the experiments B1 - B40a.

experiment	$\tilde{w}_i$ / g/g						T / °C
	FA	WA	ME	OME_1	OME_2	2-propanol	
B1	-	$8.30 \cdot 10^{-5}$	-	-	-	1.000	22
B2	-	$1.64 \cdot 10^{-4}$	-	-	-	1.000	22
B3	-	$4.26 \cdot 10^{-4}$	-	-	-	1.000	22
B4	-	0.004	-	-	-	0.996	22
B5	-	$1.14 \cdot 10^{-4}$	-	-	-	1.000	40
B6	-	0.002	-	-	-	0.998	40
B7	-	0.016	-	-	-	0.984	40
B8	-	1.000	-	-	-	-	22
B9	0.081	0.919	-	-	-	-	22
B10	0.146	0.854	-	-	-	-	22
B11	0.200	0.800	-	-	-	-	22
B12	-	-	1.000	-	-	-	22
B13	0.149	-	0.851	-	-	-	22
B14	0.253	-	0.747	-	-	-	22
B15	0.371	-	0.629	-	-	-	22
B16	0.530	-	0.470	-	-	-	22
B17	-	0.903	0.097	-	-	-	22
B18	-	0.675	0.325	-	-	-	22
B19	-	0.202	0.798	-	-	-	22
B20	-	0.055	0.945	-	-	-	22
B21	-	1.000	-	-	-	-	40
B22	0.099	0.901	-	-	-	-	40
B23	0.202	0.798	-	-	-	-	40

Table 18 – continued from previous page

experiment	$\tilde{w}_i$ / g/g						T / °C
	FA	WA	ME	OME_1	OME_2	2-propanol	
B24	0.278	0.722	-	-	-	-	40
B25	-	-	1.000	-	-	-	40
B26	0.195	-	0.805	-	-	-	40
B27	0.243	-	0.757	-	-	-	40
B28	0.376	-	0.624	-	-	-	40
B29	-	0.735	0.265	-	-	-	40
B30	-	0.470	0.530	-	-	-	40
B31	-	0.205	0.795	-	-	-	40
B32	-	0.022	0.978	-	-	-	40
B33	0.407	0.173	0.420	-	-	-	22
B34	0.224	0.163	0.613	-	-	-	22
B35	0.219	0.375	0.406	-	-	-	22
B36	0.211	0.589	0.200	-	-	-	22
B37	0.199	0.166	0.635	-	-	-	40
B38	0.197	0.379	0.424	-	-	-	40
B39	0.294	0.140	0.566	-	-	-	40
B40	0.134	0.007	0.117	0.594	0.137	-	22
B40a	0.145	0.010	0.122	0.578	0.133	-	22

Table 19: Experimental overall equilibrium loadings for the experiments B1 - B40a.

experiment	$\tilde{q}_{e,i}^{exp}$ / g/g						T / °C
	FA	WA	ME	OME_1	OME_2	2-propanol	
B1	-	0.025	-	-	-	-	22
B2	-	0.071	-	-	-	-	22
B3	-	0.115	-	-	-	-	22
B4	-	0.155	-	-	-	-	22
B5	-	0.030	-	-	-	-	40
B6	-	0.148	-	-	-	-	40
B7	-	0.175	-	-	-	-	40
B8	-	0.182	-	-	-	-	22
B9	0.012	0.182	-	-	-	-	22
B10	0.018	0.165	-	-	-	-	22
B11	0.037	0.158	-	-	-	-	22
B12	-	-	0.121	-	-	-	22
B13	0.005	-	0.121	-	-	-	22
B14	0.007	-	0.113	-	-	-	22
B15	0.037	-	0.081	-	-	-	22
B16	0.077	-	0.070	-	-	-	22
B17	-	0.171	0.006	-	-	-	22
B18	-	0.168	0.002	-	-	-	22
B19	-	0.158	0.020	-	-	-	22
B20	-	0.109	0.036	-	-	-	22
B21	-	0.181	-	-	-	-	40
B22	0.022	0.163	-	-	-	-	40
B23	0.023	0.139	-	-	-	-	40
B24	0.063	0.102	-	-	-	-	40
B25	-	-	0.120	-	-	-	40
B26	0.034	-	0.115	-	-	-	40

Table 19 – continued from previous page

experiment	$\tilde{q}_{e,i}^{exp}$ / g/g						T / °C
	FA	WA	ME	OME_1	OME_2	2-propanol	
B27	0.037	-	0.105	-	-	-	40
B28	0.075	-	0.067	-	-	-	40
B29	-	0.170	0.001	-	-	-	40
B30	-	0.157	0.022	-	-	-	40
B31	-	0.161	0.018	-	-	-	40
B32	-	0.071	0.082	-	-	-	40
B33	0.021	0.149	0.009	-	-	-	22
B34	0.010	0.151	0.013	-	-	-	22
B35	0.008	0.170	0.008	-	-	-	22
B36	0.021	0.175	-0.008	-	-	-	22
B37	0.012	0.148	0.026	-	-	-	40
B38	0.017	0.166	0.000	-	-	-	40
B39	0.026	0.152	0.009	-	-	-	40
B40	0.023	0.096	0.021	0.029	0.002	-	22
B40a	0.050	0.105	0.034	-0.013	-0.009	-	22

Table 20: Modelled overall equilibrium loadings for the experiments B1 - B40a.

experiment	$\tilde{q}_{e,i}^{mod}$ / g/g						T / °C
	FA	WA	ME	OME_1	OME_2	2-propanol	
B1	-	0.044	-	-	-	-	22
B2	-	0.071	-	-	-	-	22
B3	-	0.113	-	-	-	-	22
B4	-	0.172	-	-	-	-	22
B5	-	0.034	-	-	-	-	40
B6	-	0.141	-	-	-	-	40
B7	-	0.175	-	-	-	-	40
B8	-	0.181	-	-	-	-	22
B9	0.004	0.174	-	-	-	-	22
B10	0.012	0.170	-	-	-	-	22
B11	0.013	0.167	-	-	-	-	22
B12	-	-	0.118	-	-	-	22
B13	0.005	-	0.111	-	-	-	22
B14	0.013	-	0.101	-	-	-	22
B15	0.034	-	0.077	-	-	-	22
B16	0.077	-	0.028	-	-	-	22
B17	-	0.179	0.001	-	-	-	22
B18	-	0.175	0.004	-	-	-	22
B19	-	0.154	0.018	-	-	-	22
B20	-	0.109	0.047	-	-	-	22
B21	-	0.180	-	-	-	-	40
B22	0.022	0.154	-	-	-	-	40
B23	0.034	0.139	-	-	-	-	40
B24	0.055	0.130	-	-	-	-	40
B25	-	-	0.117	-	-	-	40
B26	0.025	-	0.096	-	-	-	40

Table 20 – continued from previous page

experiment	$\tilde{q}_{e,i}^{mod}$ / g/g						T / °C
	FA	WA	ME	OME_1	OME_2	2-propanol	
B27	0.036	-	0.088	-	-	-	40
B28	0.058	-	0.053	-	-	-	40
B29	-	0.171	0.006	-	-	-	40
B30	-	0.161	0.012	-	-	-	40
B31	-	0.139	0.027	-	-	-	40
B32	-	0.047	0.086	-	-	-	40
B33	0.008	0.162	0.006	-	-	-	22
B34	0.002	0.160	0.011	-	-	-	22
B35	0.003	0.171	0.004	-	-	-	22
B36	0.005	0.172	0.001	-	-	-	22
B37	0.010	0.140	0.018	-	-	-	40
B38	0.011	0.156	0.007	-	-	-	40
B39	0.020	0.135	0.014	-	-	-	40
B40	0.027	0.118	0.009	0.000	0.000	-	22
B40a	0.023	0.128	0.007	0.000	0.000	-	22

Table 21: Experimental overall equilibrium loadings for the experiments B1 - B40a.

experiment	repetition	m_{ads} / g	$m_{\text{liq}}^{\text{feed}}$ / g	$m_{\text{liq}}^{\text{feed}}$ / g
B1	I	15.129	34.629	1.515
	II	15.068	33.841	0.727
	III	15.092	34.167	1.038
B2	I	15.140	35.685	1.804
	II	15.135	34.259	0.463
	III	14.995	34.604	0.779
B3	I	15.183	35.398	0.935
	II	15.144	34.476	0.038
B4	I	15.029	35.161	0.115
	II	15.013	35.423	0.354
B5	I	14.970	34.550	2.233
	II	15.030	35.040	2.563
	III	15.170	34.720	2.501
B6	I	15.210	35.260	1.073
	II	15.370	35.720	1.812
	III	15.150	36.470	2.322
B7	I	15.160	37.320	2.536
	II	15.190	36.280	1.723
	III	15.060	34.800	0.132
B8	I	15.047	46.323	1.991
	II	15.271	47.040	2.640
	III	15.123	47.013	2.616
	IV	15.371	45.824	1.711

Table 21 – continued from previous page

experiment	repetition	m_{ads} / g	$m_{\mathrm{liq}}^{\mathrm{feed}}$ / g	$m_{\mathrm{liq}}^{\mathrm{feed}}$ / g
B9	I	18.315	44.611	0.273
	II	17.488	44.729	0.000
B10	I	14.745	47.350	0.944
	II	17.389	47.749	2.508
	III	19.045	45.706	0.905
B11	I	16.607	47.508	1.045
	II	16.109	48.012	1.291
	III	18.875	46.870	1.179
B12	I	15.342	34.834	0.147
	II	15.205	35.627	0.926
B13	I	15.015	39.068	1.817
	II	15.060	41.102	3.797
	III	15.131	41.961	4.666
B14	I	15.179	40.652	1.553
	II	15.168	40.644	1.650
	III	15.131	40.958	1.884
B15	I	15.084	42.902	1.654
	II	15.017	42.182	1.052
	III	15.036	42.641	1.339
B16	I	15.083	47.179	2.476
	II	15.014	46.863	2.197
	III	15.105	46.889	2.127
B17	I	14.179	46.830	2.762
	II	15.390	44.940	1.299

Table 21 – continued from previous page

experiment	repetition	m_{ads} / g	$m_{\text{liq}}^{\text{feed}}$ / g	$m_{\text{liq}}^{\text{feed}}$ / g
B18	I	15.061	42.931	0.840
	II	15.092	43.979	1.905
	III	16.262	43.141	1.459
B19	I	15.149	38.218	0.365
	II	14.873	38.788	0.849
	III	15.073	38.960	1.130
	IV	15.029	38.270	0.501
B20	I	15.084	36.519	0.758
	II	15.093	36.197	0.425
	III	15.355	36.328	0.541
	IV	15.431	36.925	1.131
B21	I	15.184	46.047	1.737
	II	15.263	47.273	3.389
	III	15.075	45.828	1.609
	IV	15.250	46.083	2.010
B22	I	15.062	47.524	2.201
	II	15.346	46.741	1.567
	III	15.274	47.223	2.492
	IV	15.197	46.994	2.045
B23	I	15.154	47.599	1.397
	II	15.101	48.246	2.005
	III	15.155	48.027	1.956
	IV	15.044	48.500	2.402

Table 21 – continued from previous page

experiment	repetition	m_{ads} / g	$m_{\mathrm{liq}}^{\mathrm{feed}}$ / g	$m_{\mathrm{liq}}^{\mathrm{feed}}$ / g
B24	I	15.323	48.833	1.336
	II	15.273	48.817	2.371
	III	15.059	50.358	2.820
	IV	15.133	48.931	2.077
B25	I	15.425	34.387	0.573
	II	15.367	48.363	0.510
	III	15.306	35.540	1.589
	IV	15.056	35.262	1.248
B26	I	15.426	38.754	1.283
	II	15.465	37.923	0.433
B27	I	15.036	39.278	0.531
	II	15.180	38.370	0.004
	III	16.051	38.171	0.005
B28	I	15.480	41.148	0.246
	II	15.002	41.891	0.923
	III	15.361	41.502	0.631
B29	I	15.124	43.911	1.800
	II	15.057	43.646	1.485
	III	15.345	44.149	2.107
	IV	15.115	43.669	1.524
B30	I	15.128	43.396	3.380
	II	15.422	41.537	1.644
	III	15.167	41.664	1.668
	IV	15.324	41.705	1.806

Table 21 – continued from previous page

experiment	repetition	m_{ads} / g	$m_{\text{liq}}^{\text{feed}}$ / g	$m_{\text{liq}}^{\text{feed}}$ / g
B31	I	15.404	38.759	1.432
	II	15.067	38.096	0.636
	III	15.462	38.063	0.968
	IV	15.147	37.952	0.793
B32	I	15.335	35.615	0.826
	II	15.334	36.070	1.307
	III	15.692	34.771	0.101
B33	I	15.055	46.221	1.309
	II	15.008	46.982	2.082
	III	15.100	46.403	1.450
B34	I	15.043	42.084	1.203
	II	15.041	41.258	0.431
	III	15.097	42.546	1.758
B35	I	14.330	45.615	2.236
	II	15.055	45.317	2.058
	III	15.117	43.808	0.601
B36	I	15.237	46.575	1.470
	II	15.097	46.411	1.146
	III	15.264	47.277	2.124
B37	I	15.135	45.226	4.866
	II	15.099	44.242	3.952
	III	15.107	44.644	4.303
B38	I	15.098	47.533	4.955
	II	15.132	47.470	4.752
	III	15.121	46.366	3.713

Table 21 – continued from previous page

experiment	repetition	m_{ads} / g	$m_{\mathrm{liq}}^{\mathrm{feed}}$ / g	$m_{\mathrm{liq}}^{\mathrm{feed}}$ / g
B39	I	15.078	42.449	0.740
	II	14.863	43.710	1.820
B40	I	15.180	42.297	1.375
	II	15.114	41.428	0.465
	III	15.424	40.934	0.109
B40a	I	15.710	42.982	2.512
	II	15.636	42.291	2.048
	III	16.087	41.035	0.613

A.10 Numerical Data of Experiments D1 - D2

Tables 22 and 23 provide the numeric data corresponding to the experiments D1 and D2, respectively.

Table 22: Experimental data corresponding to the experiment D1.

t / min	$\tilde{w}_{\text{acetone}}$ / g/g	$\tilde{w}_{\text{2-propanol}}$ / g/g
2	0.000	1.000
4	0.000	1.000
6	0.049	0.951
7	0.057	0.943
8	0.138	0.862
9	0.169	0.831
11	0.264	0.736
12	0.313	0.687
13	0.353	0.647
14	0.392	0.608
15	0.430	0.570
16	0.468	0.532

Table 23: Experimental data corresponding to the experiment D2.

t / min	$\tilde{w}_{\text{acetone}}$ / g/g	$\tilde{w}_{\text{2-propanol}}$ / g/g
1	0.000	1.000
3	0.002	0.998
4	0.056	0.944
5	0.080	0.921
6	0.143	0.857
7	0.236	0.764
8	0.275	0.725
9	0.369	0.631
10	0.520	0.480
11	0.624	0.376
12	0.664	0.336
13	0.740	0.260
14	0.759	0.241
15	0.814	0.186
16	0.861	0.139
17	0.869	0.131
18	0.908	0.092
19	0.920	0.080
21	0.951	0.049
23	0.964	0.036
25	0.973	0.027
27	0.977	0.023

A.11 Numerical Data of Experiments C1 - C3

Tables 24, 25, and 26 provide the numeric data corresponding to the experiments C1, C2, and C3, respectively.

Table 24: Experimental data corresponding to the experiment C1.

t / min	$\tilde{w}_{\mathrm{WA}}$ / g/g	$\tilde{w}_{\mathrm{FA}}$ / g/g	$\tilde{w}_{\mathrm{ME}}$
13	0.001	0.205	0.148
23	0.000	-	-
33	0.000	0.195	0.146
43	0.000	-	-
53	0.000	0.197	0.146
63	0.000	-	-
73	0.001	0.199	0.150
83	0.010	-	-
93	0.021	0.197	0.145
103	0.030	-	-
113	0.035	0.196	0.142
123	0.039	-	-
133	0.042	0.192	0.141
143	0.046	-	-

Table 25: Experimental data corresponding to the experiment C2.

Time / min	$\tilde{w}_{\mathrm{WA}}$ / g/g	$\tilde{w}_{\mathrm{FA}}$ / g/g	$\tilde{w}_{\mathrm{ME}}$
12	0.000	0.152	0.124
23	0.000	0.152	0.128
33	0.000	0.154	0.128
43	0.000	0.155	0.128
53	0.001	0.155	0.128
63	0.007	0.154	0.127
73	0.016	0.152	0.126
83	0.024	0.151	0.124
93	0.030	0.150	0.124
106	0.036	0.151	0.123

Table 26: Experimental data corresponding to the experiment C3.

Time / min	$\tilde{w}_{\mathrm{WA}}$ / g/g	$\tilde{w}_{\mathrm{FA}}$ / g/g	$\tilde{w}_{\mathrm{ME}}$
10	0.001	0.198	0.147
15	0.000	-	-
20	0.000	0.196	0.146
25	0.000	-	-
30	0.000	0.199	0.146
35	0.004	-	-
40	0.009	0.198	0.144
45	0.016	-	-
50	0.022	0.196	0.143
55	0.027	-	-
60	0.029	0.192	0.141
65	0.033	-	-
70	0.036	0.193	0.140
75	0.039	-	-
80	0.041	0.195	0.140

A.12 Breakthrough Curves of Formaldehyde and Methanol in Experiments C1 and C3

Figures 28 and 29 depict the breakthrough curves of formaldehyde and methanol in experiments C1 and C3, respectively.

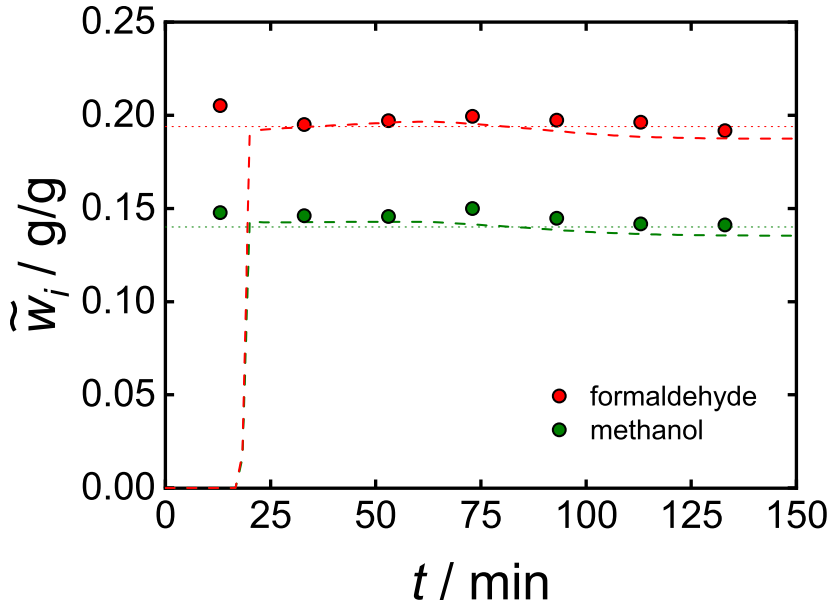

Figure 28: Experimental and modelled breakthrough curves of formaldehyde (red) and methanol (green) in the experiment C1. Markers: Experimental data. Dashed lines: Model. Dotted lines: Feed composition.

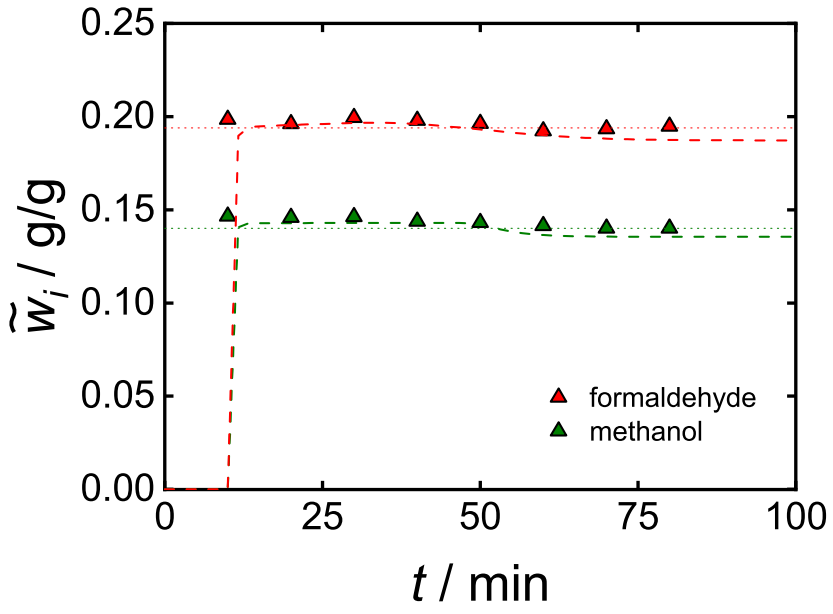

Figure 29: Experimental and modelled breakthrough curves of formaldehyde (red) and methanol (green) in the experiment C3. Markers: Experimental data. Dashed lines: Model. Dotted lines: Feed composition.

B Water Separation via Pervaporation

B.1 Characterisation of the SiO_2 Membrane

Figure 30 displays a scanning electron microscopy (SEM) image depicting the cross-section of a SiO_2 membrane. The SiO_2 active layer does not seem to be visible in the image. However, X-ray diffraction (XRD) analysis performed on various positions of the SiO_2 membrane confirmed the presence of aluminium (the support material) and silicon on the internal membrane surface. The water contact angle test revealed a very high level of hydrophilicity in the membrane. A water droplet completely spread across the surface, essentially forming a near-zero contact angle with the surface of the active layer.

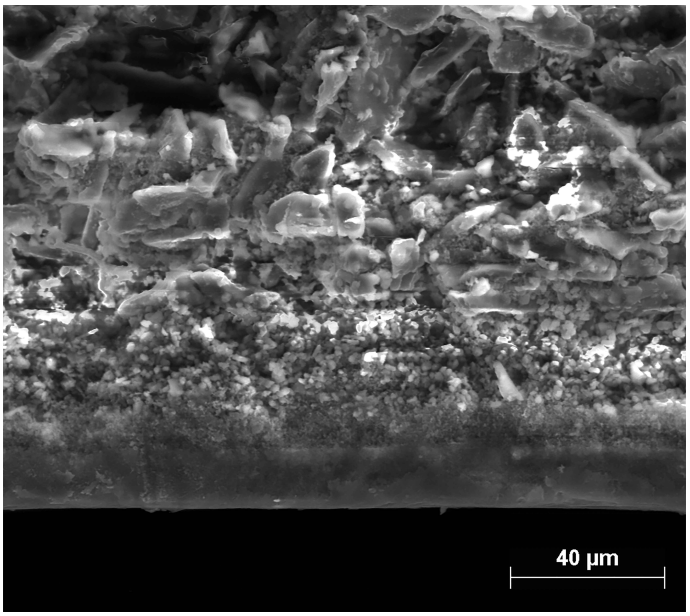

Figure 30: SEM image of the cross-section of a SiO_2 membrane.

B.2 Stream Tables of Experiments M1 - M14

Tables 27, 28 and 29 present the masses and composition of the initial feed, the first condensate and the second condensate for experiments M1 - M14, respectively. Note that in the case of the first and second condensate of experiment M2, only the overall mass fractions of water and formaldehyde were able to be analysed.

Table 27: Initial mass and composition of the feed for experiments M1 - M14.

experiment	overall mass fraction / g/g						mass / kg
	WA	FA	ME	OME_1	OME_2	$OME_{\geq 3}$	
M1	0.088	0.198	0.196	0.297	0.143	0.078	36.65
M2	0.099	0.200	0.178	0.298	0.145	0.080	41.69
M3	0.070	0.201	0.210	0.297	0.145	0.077	38.62
M4	0.036	0.221	0.202	0.307	0.157	0.077	44.84
M5	0.036	0.221	0.202	0.307	0.155	0.079	41.12
M6	0.051	0.182	0.093	0.398	0.243	0.043	40.70
M7	0.047	0.169	0.149	0.397	0.208	0.035	37.24
M8	0.053	0.193	0.156	0.386	0.202	0.020	43.07
M9	0.049	0.191	0.166	0.373	0.204	0.057	46.09
M10	0.048	0.189	0.153	0.389	0.205	0.028	41.44
M11	0.046	0.181	0.153	0.388	0.207	0.036	40.79
M12	0.450	0.121	0.106	0.201	0.117	0.019	44.02
M13	0.428	0.131	0.101	0.214	0.127	0.041	41.12
M14	0.369	0.146	0.099	0.245	0.141	0.049	40.70

Table 28: Mass and composition of the first condensate for experiments M1 - M14.

experiment	overall mass fraction / g/g						mass / kg
	WA	FA	ME	OME_1	OME_2	$OME_{\geq 3}$	
M1	0.869	0.053	0.059	0.003	0.008	0.009	2.05
M2	0.786	0.007	-	-	-	-	2.96
M3	0.775	0.080	0.109	0.012	0.012	0.012	1.84
M4	0.678	0.164	0.107	0.003	0.015	0.033	0.89
M5	0.692	0.134	0.117	0.005	0.014	0.037	0.95
M6	0.674	0.126	0.096	0.017	0.071	0.016	1.15
M7	0.711	0.107	0.118	0.005	0.045	0.014	0.53
M8	0.718	0.124	0.107	0.007	0.038	0.006	1.65
M9	0.683	0.117	0.124	0.012	0.057	0.007	1.79
M10	0.708	0.111	0.109	0.012	0.053	0.007	1.34
M11	0.637	0.124	0.109	0.049	0.069	0.012	1.14
M12	0.803	0.057	0.090	0.023	0.025	0.002	4.63
M13	0.859	0.050	0.070	0.008	0.013	0.000	5.38
M14	0.880	0.045	0.056	0.007	0.012	0.000	4.29

Table 29: Mass and composition of the second condensate for experiments M1 - M14.

experiment	overall mass fraction / g/g						mass / kg
	WA	FA	ME	OME_1	OME_2	$OME_{\geq 3}$	
M1	0.400	0.084	0.190	0.225	0.093	0.009	0.34
M2	0.395	0.107	-	-	-	-	0.59
M3	0.340	0.110	0.220	0.233	0.084	0.012	0.48
M4	0.194	0.112	0.184	0.336	0.146	0.030	0.79
M5	0.231	0.113	0.187	0.304	0.146	0.020	0.66
M6	0.123	0.123	0.058	0.498	0.191	0.007	0.84
M7	0.195	0.130	0.155	0.223	0.289	0.008	0.32
M8	0.127	0.126	0.103	0.476	0.164	0.004	1.15
M9	0.166	0.114	0.104	0.459	0.153	0.004	1.16
M10	0.158	0.111	0.096	0.473	0.158	0.004	0.89
M11	0.130	0.107	0.091	0.498	0.169	0.005	0.70
M12	0.424	0.076	0.133	0.292	0.076	0.000	1.03
M13	0.476	0.083	0.130	0.252	0.060	0.000	1.03
M14	0.478	0.104	0.109	0.238	0.071	0.000	0.62

B.3 Concentration Profiles of Experiments M1 - M14

Figures 31 to 41 illustrate the time-dependent evolution of the overall mass fraction of water with the time for experiments M2, M3, M4, M5, M6, M8, M9, M10, M11, M13, and M14, respectively (similar plots for experiments M1, M7, and M12 are given in Section 3.4.1.) The simulated time profiles were obtained by combining and integrating numerically Equations (39) to (41) in Section 3.3.2 with the initial conditions. Furthermore, Tables 30 to 43 present the numerical data on these plots for experiments M1 to M14.

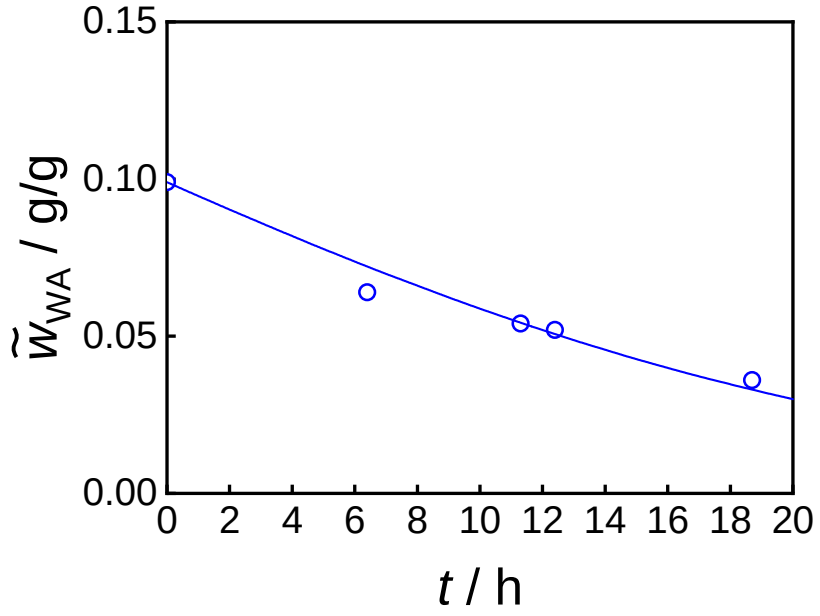

Figure 31: Evolution of the overall mass fraction of water in the feed for the experiment M2. Symbols: Experimental data. Lines: Model.

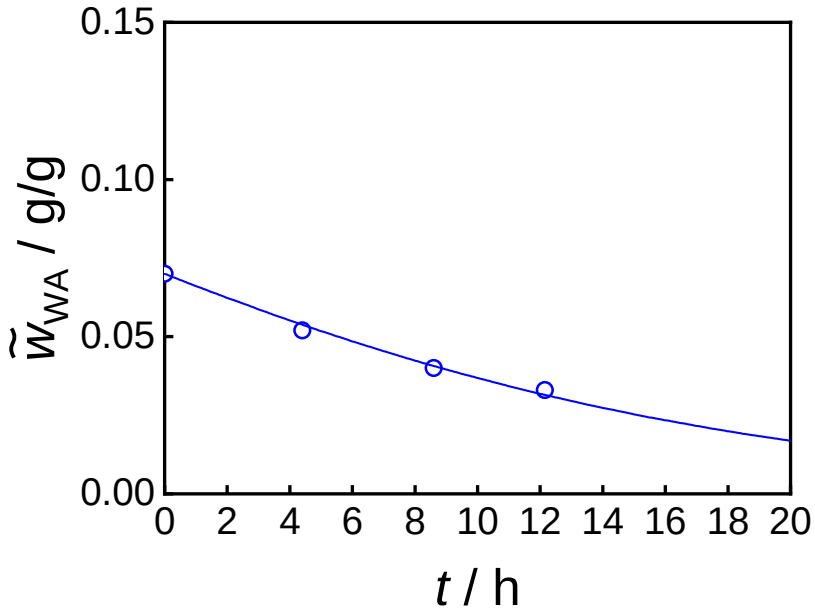

Figure 32: Evolution of the overall mass fraction of water in the feed for the experiment M3. Symbols: Experimental data. Lines: Model.

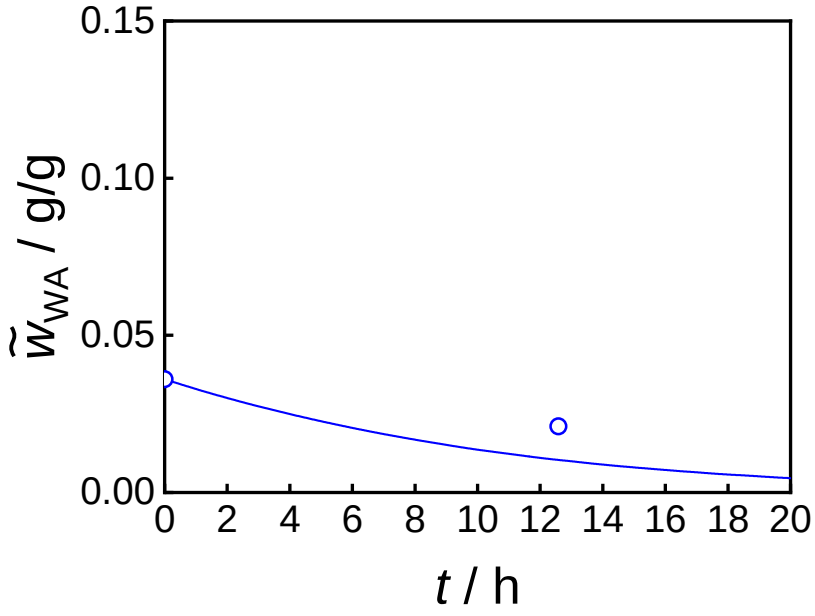

Figure 33: Evolution of the overall mass fraction of water in the feed for the experiment M4. Symbols: Experimental data. Lines: Model.

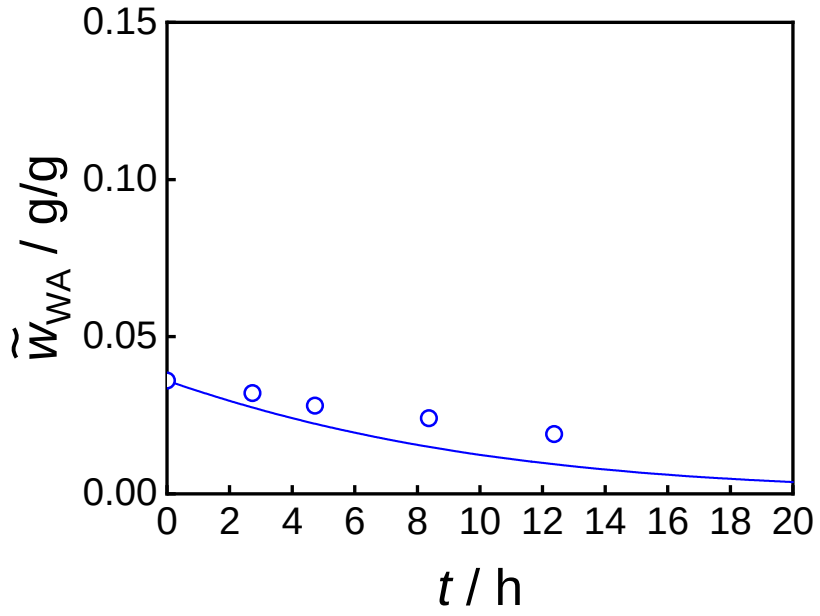

Figure 34: Evolution of the overall mass fraction of water in the feed for the experiment M5. Symbols: Experimental data. Lines: Model.

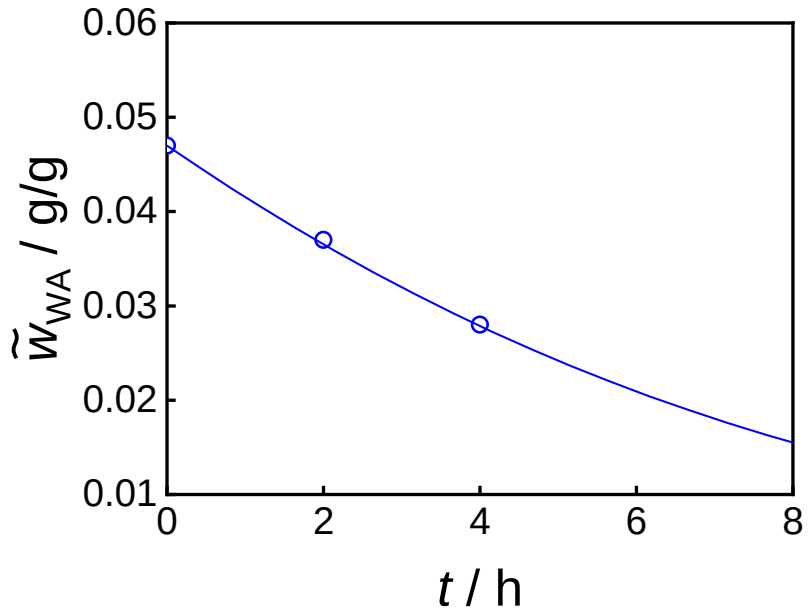

Figure 35: Evolution of the overall mass fraction of water in the feed for the experiment M6. Symbols: Experimental data. Lines: Model.

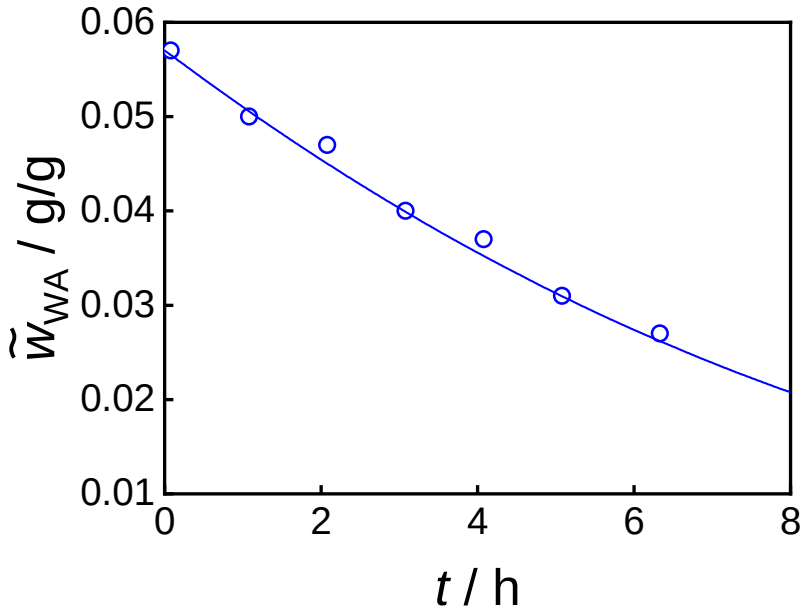

Figure 36: Evolution of the overall mass fraction of water in the feed for the experiment M8. Symbols: Experimental data. Lines: Model.

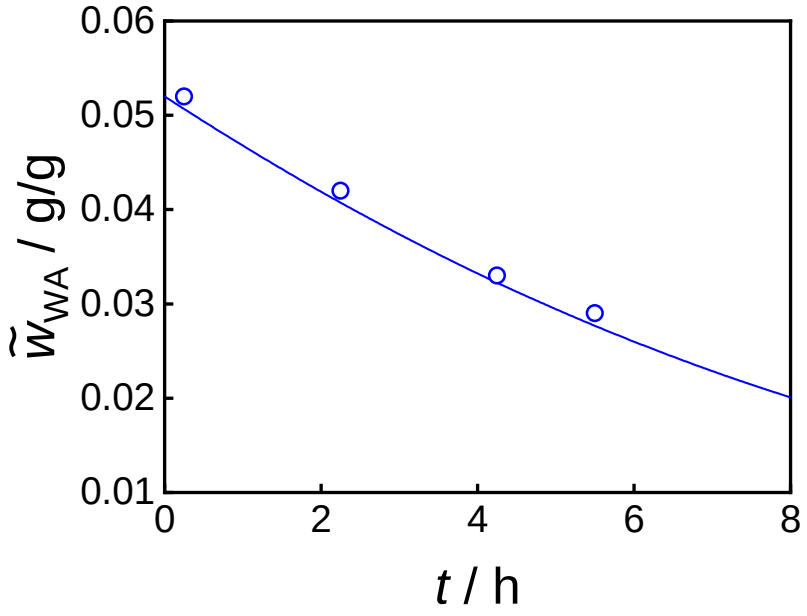

Figure 37: Evolution of the overall mass fraction of water in the feed for the experiment M9. Symbols: Experimental data. Lines: Model.

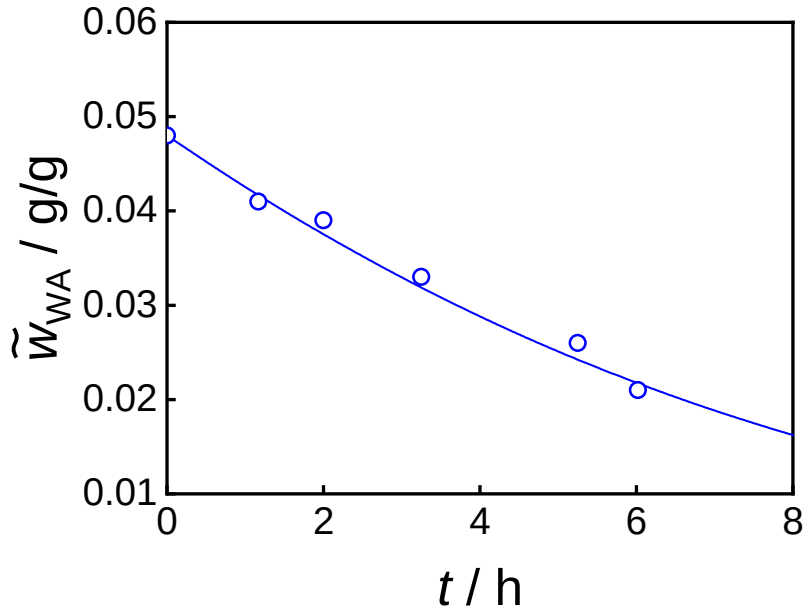

Figure 38: Evolution of the overall mass fraction of water in the feed for the experiment M10. Symbols: Experimental data. Lines: Model.

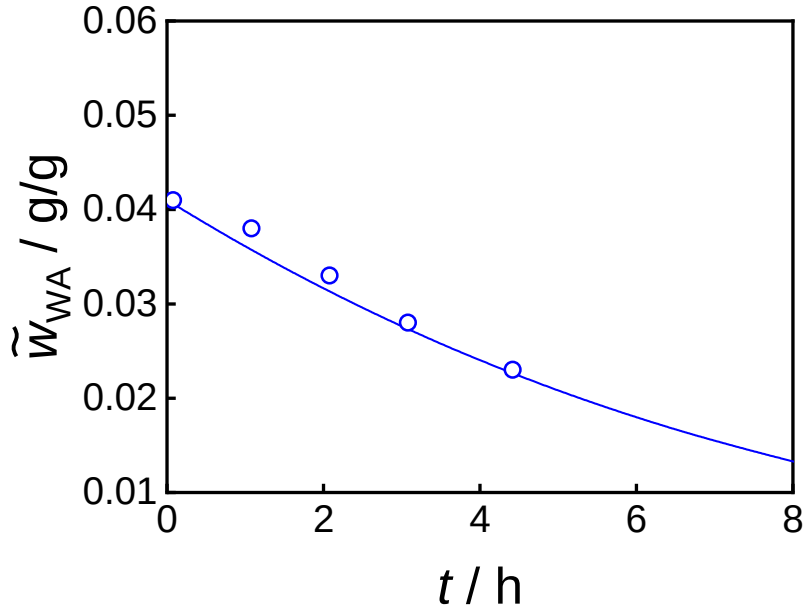

Figure 39: Evolution of the overall mass fraction of water in the feed for the experiment M11. Symbols: Experimental data. Lines: Model.

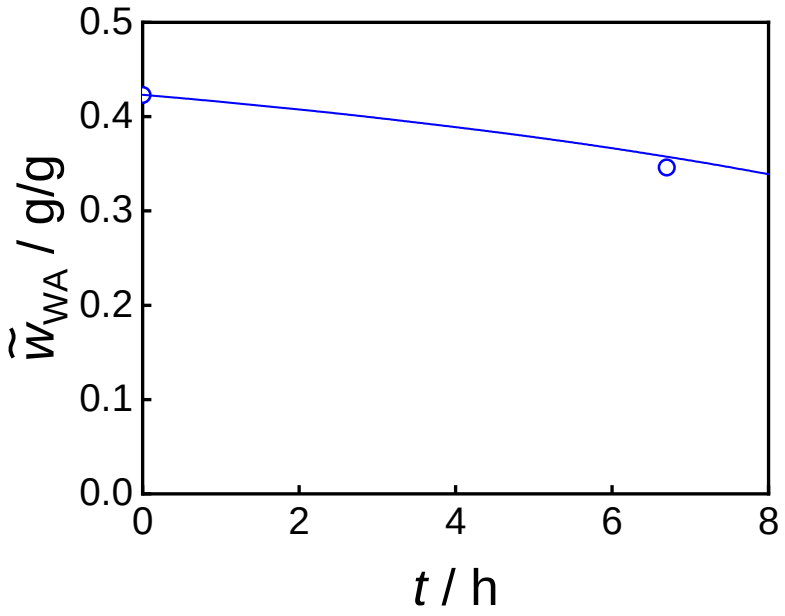

Figure 40: Evolution of the overall mass fraction of water in the feed for the experiment M13. Symbols: Experimental data. Lines: Model.

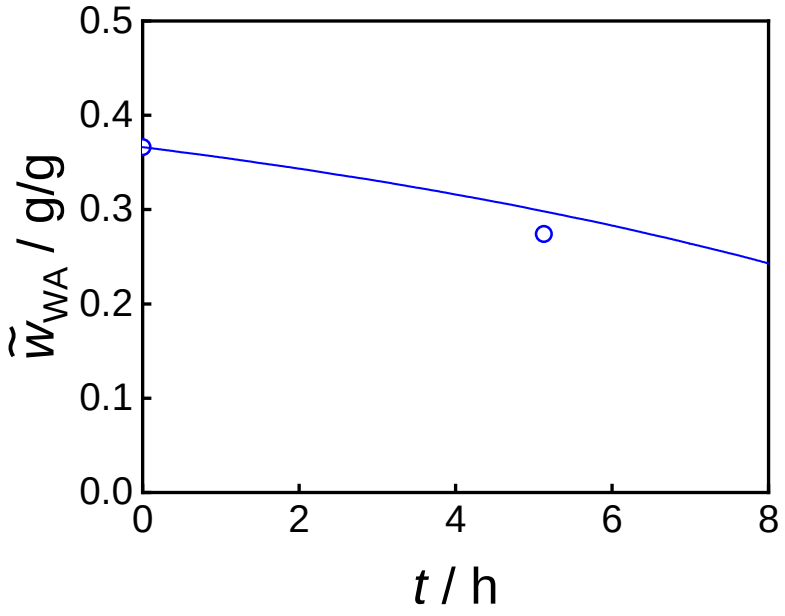

Figure 41: Evolution of the overall mass fraction of water in the feed for the experiment M14. Symbols: Experimental data. Lines: Model.

Table 30: Evolution of the experimental overall mass fractions of water for experiment M1.

t / h	$\tilde{w}_{\mathrm{WA}}$ / g/g
0	0.088
4.0	0.074
6.0	0.067
12.6	0.051
16.1	0.045
18.9	0.038

Table 31: Evolution of the experimental overall mass fractions of water for experiment M2.

t / h	$\tilde{w}_{\mathrm{WA}}$ / g/g
0	0.099
6.4	0.063
11.3	0.054
12.4	0.051
18.7	0.035

Table 32: Evolution of the experimental overall mass fractions of water for experiment M3.

t / h	$\tilde{w}_{\mathrm{WA}}$ / g/g
0	0.070
4.4	0.052
8.6	0.040
12.2	0.033

Table 33: Evolution of the experimental overall mass fractions of water for experiment M4.

t / h	$\tilde{w}_{\mathrm{WA}}$ / g/g
0	0.036
12.6	0.021

Table 34: Evolution of the experimental overall mass fractions of water for experiment M5.

t / h	$\tilde{w}_{\mathrm{WA}}$ / g/g
0	0.036
2.7	0.032
4.7	0.028
8.4	0.024
12.4	0.019

Table 35: Evolution of the experimental overall mass fractions of water for experiment M6.

t / h	$\tilde{w}_{\mathrm{WA}}$ / g/g
0	0.051
4.4	0.044

Table 36: Evolution of the experimental overall mass fractions of water for experiment M7.

t / h	$\tilde{w}_{\mathrm{WA}}$ / g/g
0	0.047
1.0	0.042
2.0	0.037
2.8	0.035

Table 37: Evolution of the experimental overall mass fractions of water for experiment M8.

t / h	$\tilde{w}_{\mathrm{WA}}$ / g/g
0	0.053
0.1	0.057
1.1	0.050
2.1	0.047
3.1	0.040
4.1	0.037
5.1	0.031
6.3	0.027

Table 38: Evolution of the experimental overall mass fractions of water for experiment M9.

t / h	$\tilde{w}_{\mathrm{WA}}$ / g/g
0	0.049
0.3	0.052
2.3	0.042
4.3	0.033
5.5	0.029

Table 39: Evolution of the experimental overall mass fractions of water for experiment M10.

t / h	$\tilde{w}_{\mathrm{WA}}$ / g/g
0	0.048
1.2	0.041
2.0	0.039
3.3	0.033
5.3	0.026
6.0	0.021

Table 40: Evolution of the experimental overall mass fractions of water for experiment M11.

t / h	$\tilde{w}_{\mathrm{WA}}$ / g/g
0	0.046
0.1	0.041
1.1	0.038
2.1	0.033
3.1	0.028
4.4	0.023

Table 41: Evolution of the experimental overall mass fractions of water for experiment M12.

t / h	$\tilde{w}_{\mathrm{WA}}$ / g/g
0	0.450
5.5	0.416

Table 42: Evolution of the experimental overall mass fractions of water for experiment M13.

t / h	$\tilde{w}_{\mathrm{WA}}$ / g/g
0	0.428
6.7	0.346

Table 43: Evolution of the experimental overall mass fractions of water for experiment M14.

t / h	$\tilde{w}_{\mathrm{WA}}$ / g/g
0	0.369
5.1	0.274

B.4 Rectification of the Combined Overall Permeate of Experiment M12

In this section, details about the rectification of the permeate of experiment M12 (according to Section 4.3) are given. The rectification column was simulated in Aspen Plus and specified as follows:

- Top pressure = 4 bara
- Pressure drop = 0 bara
- Reflux ratio = 3
- Mass bottoms-to-feed ratio = 0.37
- Number of theoretical stages = 20 (without including the condenser and the reboiler)

Table 44 presents the mass flow rates, temperature and full composition of the feed, distillate and bottom streams. The simulation shows that it is possible to obtain a bottom product containing > 0.999 g/g of water.

Table 44: Stream table of the distillation of the combined overall permeate of experiment M12. Reflux ratio: 3. Top pressure = 4 bar.

	Feed	Distillate	Bottom
Mass flow rate / kg/h	0.417	0.263	0.154
Temperature / °C	25	106.50	143.61
Overall mass fractions / g/g			
Formaldehyde	0.116	0.184	$1.2 \cdot 10^{-5}$
Methanol	0.116	0.184	$8.0 \cdot 10^{-10}$
Water	0.480	0.174	> 0.999
OME_1	0.187	0.297	$1.2 \cdot 10^{-21}$
OME_2	0.094	0.150	0.000
$OME_{\geq 3}$	0.006	0.010	0.000

C Overall Process

C.1 Reactor Profiles

In the following, tables and figures presenting the composition reactor profiles corresponding to Runs 4, 6, and are given.

Table 45: Reactor profile of experimental overall mass fractions in the liquid phase of Run 4.

pseudo residence time / min	overall mass fractions / g/g								
	FA	ME	WA	OME_1	OME_2	OME_3	OME_4	OME_5	OME_6
0	0.247	0.194	0.031	0.338	0.177	0.011	0.001	0.000	0.000
0.46	0.236	0.183	0.031	0.351	0.183	0.013	0.002	0.001	0.000
0.91	0.235	0.183	0.032	0.350	0.183	0.013	0.002	0.001	0.000
1.37	0.221	0.169	0.034	0.360	0.189	0.020	0.005	0.002	0.001
1.82	0.190	0.143	0.042	0.360	0.191	0.050	0.017	0.006	0.002
2.73	0.167	0.140	0.043	0.356	0.181	0.072	0.027	0.010	0.003

Table 46: Reactor profile of experimental overall mass fractions in the liquid phase of Run 6.

pseudo residence time / min	overall mass fractions / g/g								
	FA	ME	WA	OME_1	OME_2	OME_3	OME_4	OME_5	OME_6
0	0.225	0.178	0.028	0.361	0.192	0.014	0.000	0.000	0.000
0.44	0.224	0.177	0.031	0.351	0.185	0.023	0.005	0.002	0.001
0.89	0.224	0.176	0.030	0.351	0.186	0.025	0.005	0.002	0.001
1.33	0.226	0.177	0.031	0.341	0.189	0.026	0.006	0.002	0.001
1.77	0.189	0.144	0.039	0.362	0.194	0.049	0.016	0.006	0.002
2.66	0.166	0.136	0.042	0.356	0.185	0.073	0.028	0.010	0.004

Table 47: Reactor profile of experimental overall mass fractions in the liquid phase of Run 7.

pseudo residence time / min	overall mass fractions / g/g								
	FA	ME	WA	OME_1	OME_2	OME_3	OME_4	OME_5	OME_6
0	0.227	0.185	0.030	0.342	0.189	0.024	0.002	0.001	0.000
0.44	0.238	0.184	0.025	0.348	0.179	0.022	0.002	0.001	0.000
0.88	0.239	0.187	0.026	0.342	0.181	0.023	0.002	0.001	0.000
1.32	0.246	0.187	0.029	0.331	0.181	0.023	0.002	0.001	0.000
1.76	0.198	0.148	0.037	0.358	0.192	0.048	0.013	0.004	0.002
2.63	0.170	0.138	0.041	0.351	0.181	0.075	0.028	0.010	0.004

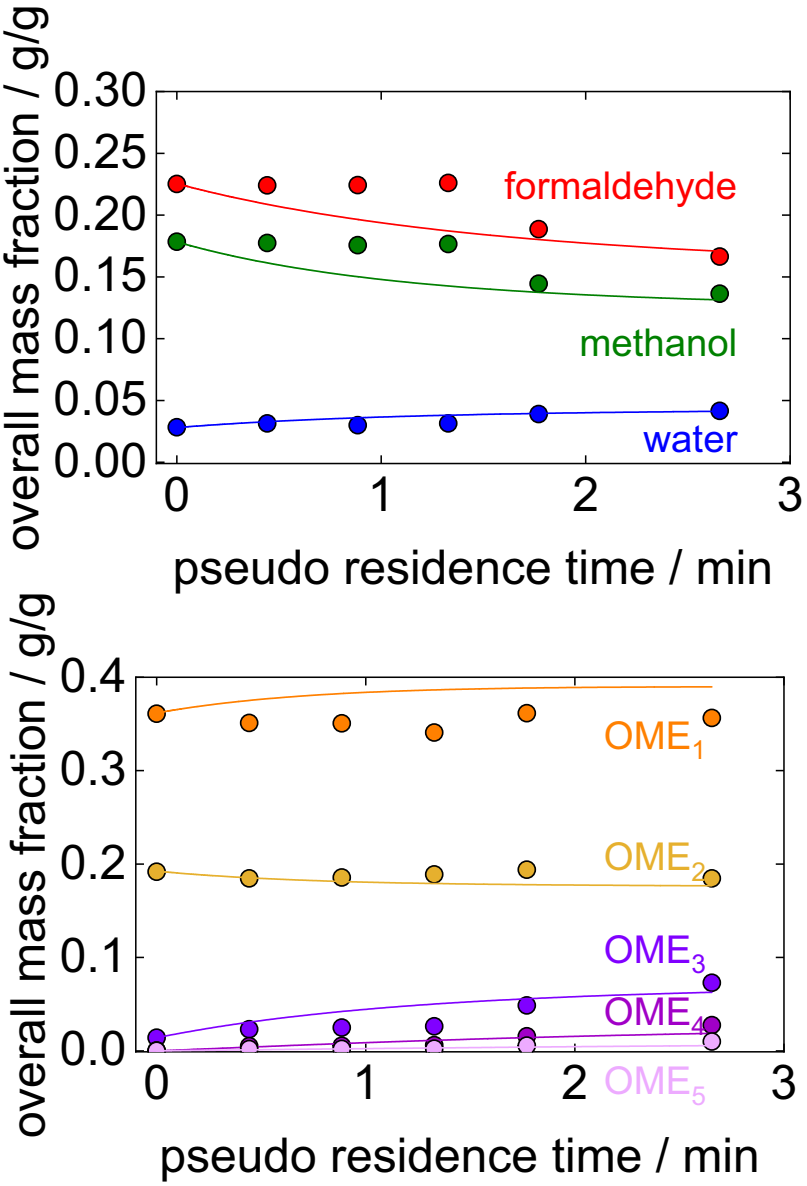

Figure 42: Reactor profiles of overall mass fractions corresponding to steady-state of Run 6. Filled circles: Experimental results. Solid lines: Reactor model.

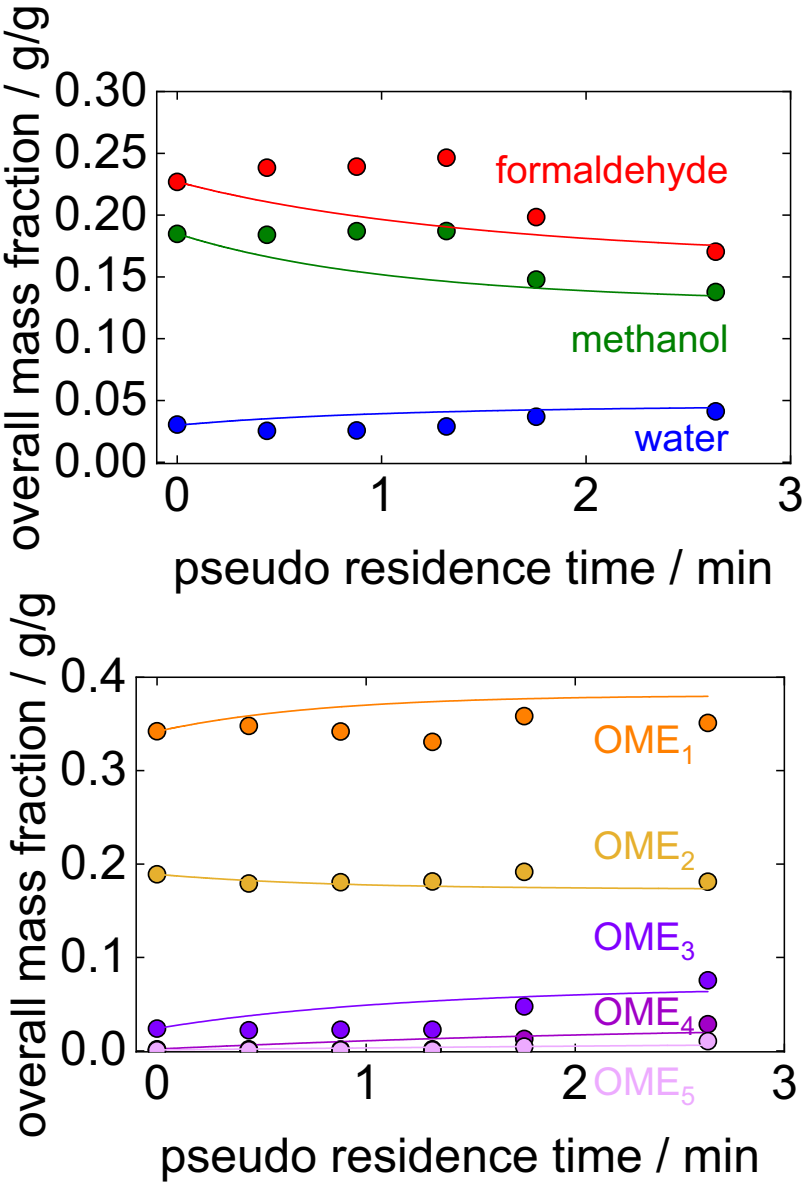

Figure 43: Reactor profiles of overall mass fractions corresponding to steady-state of Run 7. Filled circles: Experimental results. Solid lines: Reactor model.

C.2 Distillation Profiles

In the following, tables and figures presenting the temperature and composition distillation profiles corresponding to Runs 4, 5, 6, 7, 8, 9, and 10 are given.

Run 4

Table 48: Profile of experimental temperatures in the liquid phase of Run 4.

packing height / m	temperature / °C
0	183.39
0.36	175.29
1.10	138.68
1.84	103.91
2.62	93.72
3.36	95.73
4.10	94.03
4.99	92.79

Table 49: Profile of experimental overall mass fractions in the liquid phase of Run 4.

packing height / m	overall mass fractions / g/g								
	FA	ME	WA	OME_1	OME_2	OME_3	OME_4	OME_5	OME_6
0	0.001	0.000	0.000	0.000	0.000	0.534	0.287	0.124	0.054
0.39	0.017	0.002	0.001	0.005	0.003	0.850	0.103	0.016	0.003
1.13	0.210	0.084	0.002	0.004	0.003	0.599	0.078	0.016	0.004
1.87	0.474	0.204	0.006	0.011	0.006	0.232	0.046	0.016	0.005
2.61	0.394	0.231	0.032	0.081	0.132	0.119	0.010	0.001	0.000
3.35	0.390	0.223	0.039	0.083	0.163	0.102	0.000	0.000	0.000
4.09	0.388	0.211	0.045	0.115	0.147	0.094	0.000	0.000	0.000
5.10	0.178	0.155	0.041	0.385	0.198	0.032	0.000	0.007	0.000

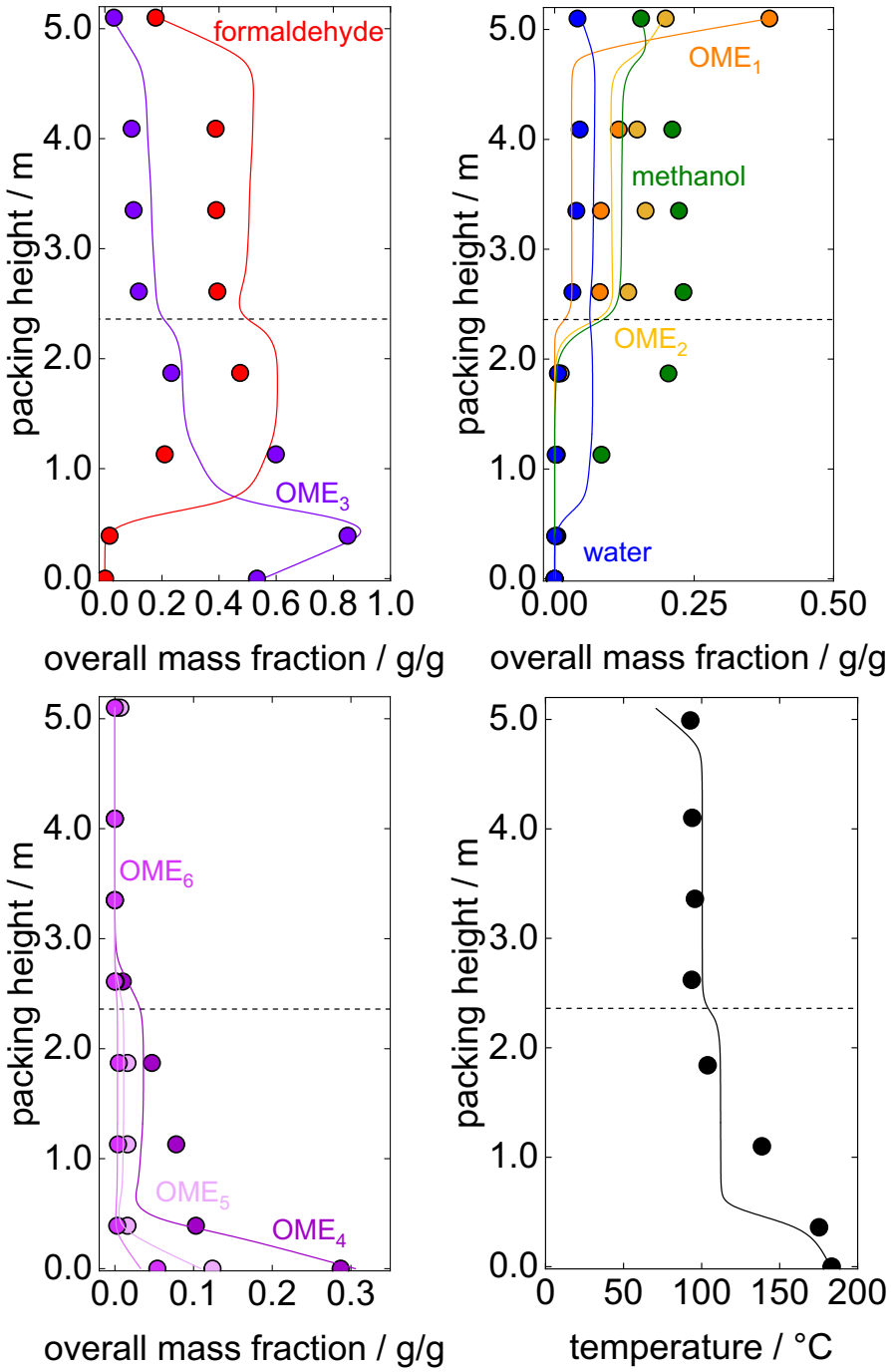

Figure 44: Distillation profiles of overall mass fractions in the liquid phase and temperature corresponding to Run 4. Filled circles: Experimental results. Solid lines: Simulation using equilibrium stage model, where the mass fraction of OME_3 at 0.43 m and reflux ratio were specified. Dashed line: Feed position. Crosses: predicted freezing temperatures. Dotted line: predicted freezing temperatures (interpolation).

Run 5

Table 50: Profile of experimental temperatures in the liquid phase of Run 5.

packing height / m	temperature / °C
0	186.90
0.36	174.82
1.10	150.98
1.84	102.11
2.62	92.49
3.36	98.71
4.10	97.12
4.99	93.66

Table 51: Profile of experimental overall mass fractions in the liquid phase of Run 5.

packing height / m	overall mass fractions / g/g								
	FA	ME	WA	OME_1	OME_2	OME_3	OME_4	OME_5	OME_6
0	0.001	0.000	0.000	0.000	0.001	0.522	0.295	0.127	0.054
0.39	0.008	0.002	0.001	0.012	0.006	0.797	0.148	0.022	0.004
1.13	0.012	0.002	0.001	0.005	0.003	0.912	0.054	0.009	0.002
1.87	0.474	n.m.	0.007	n.m.	n.m.	n.m.	n.m.	n.m.	n.m.
2.61	0.381	0.204	0.036	0.107	0.126	0.136	0.009	0.001	0.000
3.35	0.418	0.230	0.038	0.098	0.125	0.090	0.001	0.000	0.000
4.09	0.347	0.214	0.041	0.169	0.143	0.086	0.000	0.000	0.000
5.10	0.190	0.153	0.048	0.390	0.206	0.013	0.000	0.001	0.000

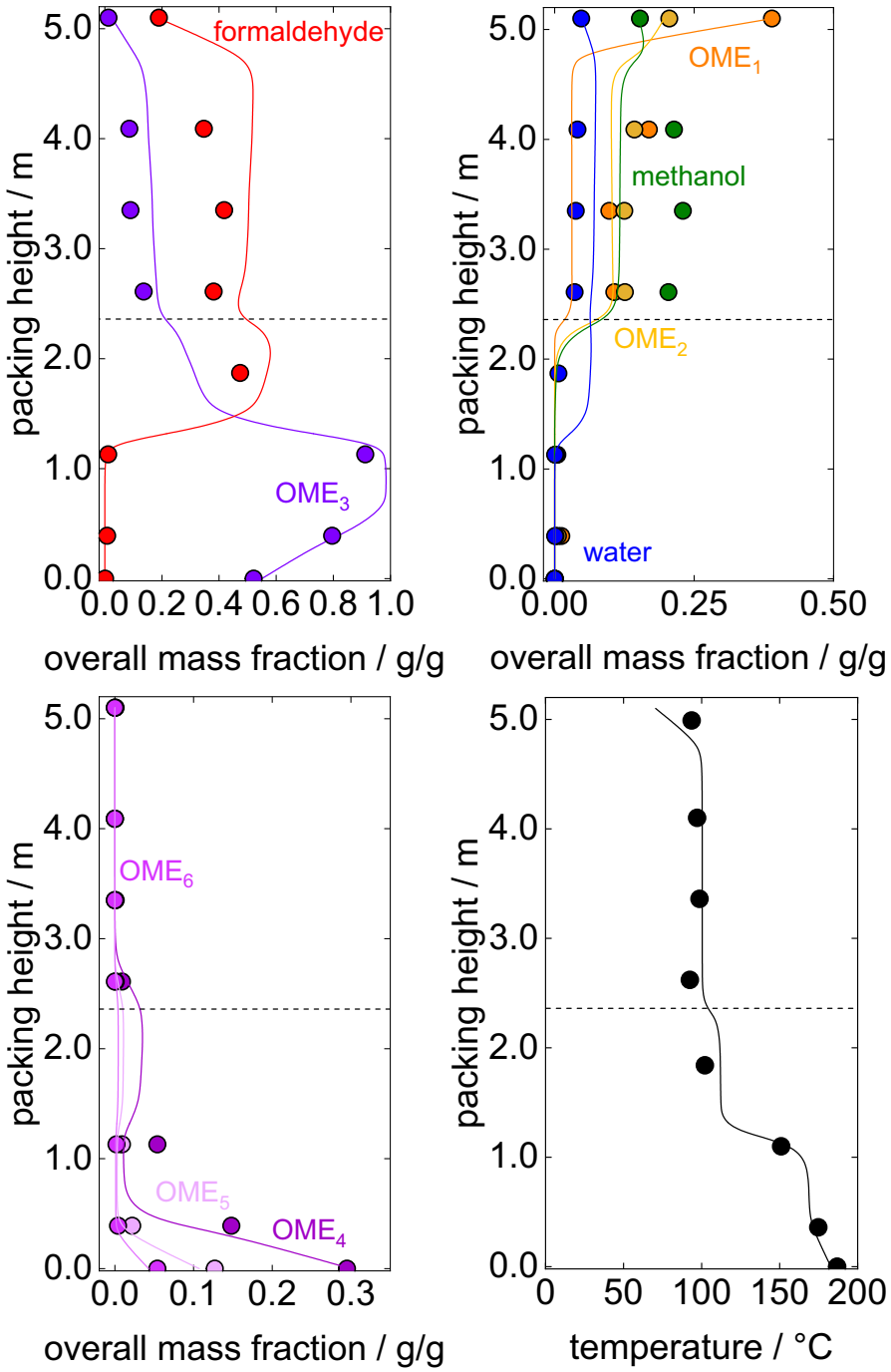

Figure 45: Distillation profiles of overall mass fractions in the liquid phase and temperature corresponding to Run 5. Filled circles: Experimental results. Solid lines: Simulation using equilibrium stage model, where the mass fraction of OME_3 at 0.43 m and reflux ratio were specified. Dashed line: Feed position. Crosses: Predicted freezing temperatures. Dotted line: Predicted freezing temperatures (interpolation).

Run 6

Table 52: Profile of experimental temperatures in the liquid phase of Run 6.

packing height / m	temperature / °C
0	188.81
0.36	176.40
1.10	168.30
1.84	156.82
2.62	85.51
3.36	96.67
4.10	94.14
4.99	92.45

Table 53: Profile of experimental overall mass fractions in the liquid phase of Run 6.

packing height / m	overall mass fractions / g/g								
	FA	ME	WA	OME_1	OME_2	OME_3	OME_4	OME_5	OME_6
0	0.000	0.000	0.000	0.000	0.000	0.491	0.322	0.136	0.050
0.39	0.004	0.002	0.002	0.010	0.005	0.798	0.153	0.022	0.003
1.13	0.006	0.002	0.002	0.007	0.005	0.883	0.081	0.013	0.002
1.87	0.024	n.m.	0.001	n.m.	n.m.	n.m.	n.m.	n.m.	n.m.
2.61	0.239	0.134	0.019	0.087	0.128	0.387	0.005	0.001	0.000
3.35	0.305	0.167	0.023	0.074	0.129	0.302	0.000	0.000	0.000
4.09	0.301	0.182	0.031	0.117	0.145	0.225	0.000	0.000	0.000
5.10	0.189	0.147	0.043	0.398	0.198	0.025	0.000	0.000	0.000

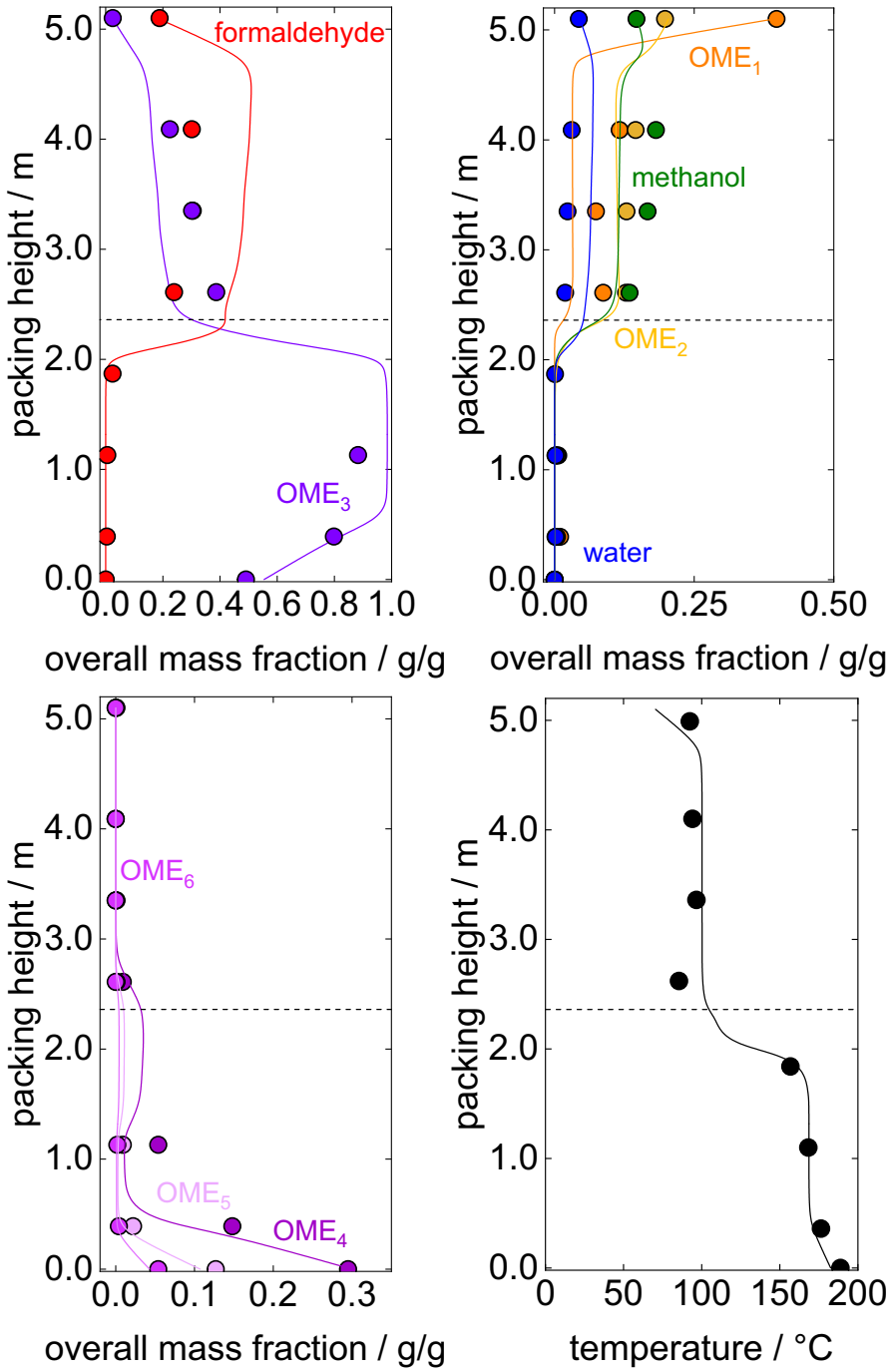

Figure 46: Distillation profiles of overall mass fractions in the liquid phase and temperature corresponding to Run 6. Filled circles: Experimental results. Solid lines: Simulation using equilibrium stage model, where the mass fraction of OME_3 at 0.43 m and reflux ratio were specified. Dashed line: Feed position. Crosses: Predicted freezing temperatures. Dotted line: Predicted freezing temperatures (interpolation).

Run 7

Table 54: Profile of experimental temperatures in the liquid phase of Run 7.

packing height / m	temperature / °C
0	185.75
0.36	174.16
1.10	164.88
1.84	113.07
2.62	83.56
3.36	98.63
4.10	97.02
4.99	93.96

Table 55: Profile of experimental overall mass fractions in the liquid phase of Run 7.

packing height / m	overall mass fractions / g/g								
	FA	ME	WA	OME_1	OME_2	OME_3	OME_4	OME_5	OME_6
0	0.001	0.000	0.000	0.000	0.001	0.522	0.293	0.128	0.055
0.39	0.006	0.002	0.001	0.006	0.004	0.820	0.136	0.021	0.004
1.13	0.012	0.003	0.001	0.003	0.002	0.924	0.045	0.008	0.002
1.87	0.412	0.181	0.006	0.011	0.011	0.334	0.031	0.010	0.004
2.61	0.437	0.235	0.033	0.082	0.114	0.093	0.005	0.001	0.000
3.35	0.470	0.243	0.021	0.051	0.104	0.111	0.000	0.000	0.000
4.09	0.430	0.231	0.039	0.080	0.115	0.105	0.000	0.000	0.000
5.10	0.192	0.162	0.050	0.370	0.214	0.009	0.000	0.002	0.000

Run 8

Table 56: Profile of experimental temperatures in the liquid phase of Run 8.

packing height / m	temperature / °C
0	189.91
0.36	176.25
1.10	161.38
1.84	106.56
2.62	84.41
3.36	93.03
4.10	91.46
4.99	91.43

Table 57: Profile of experimental overall mass fractions in the liquid phase of Run 8.

packing height / m	overall mass fractions / g/g								
	FA	ME	WA	OME_1	OME_2	OME_3	OME_4	OME_5	OME_6
0	0.000	0.000	0.000	0.001	0.001	0.479	0.328	0.138	0.054
0.39	0.010	0.004	0.001	0.003	0.003	0.888	0.077	0.012	0.002
1.13	0.021	0.006	0.002	0.005	0.005	0.952	0.007	0.002	0.000
1.87	0.046	0.015	0.003	0.012	0.010	0.906	0.008	0.002	0.001
2.61	0.355	0.159	0.047	0.228	0.136	0.071	0.003	0.000	0.000
3.35	0.457	0.183	0.042	0.121	0.119	0.077	0.001	0.000	0.000
4.09	0.413	0.179	0.048	0.151	0.130	0.077	0.001	0.000	0.000
5.10	0.174	0.133	0.063	0.431	0.181	0.018	0.000	0.000	0.000

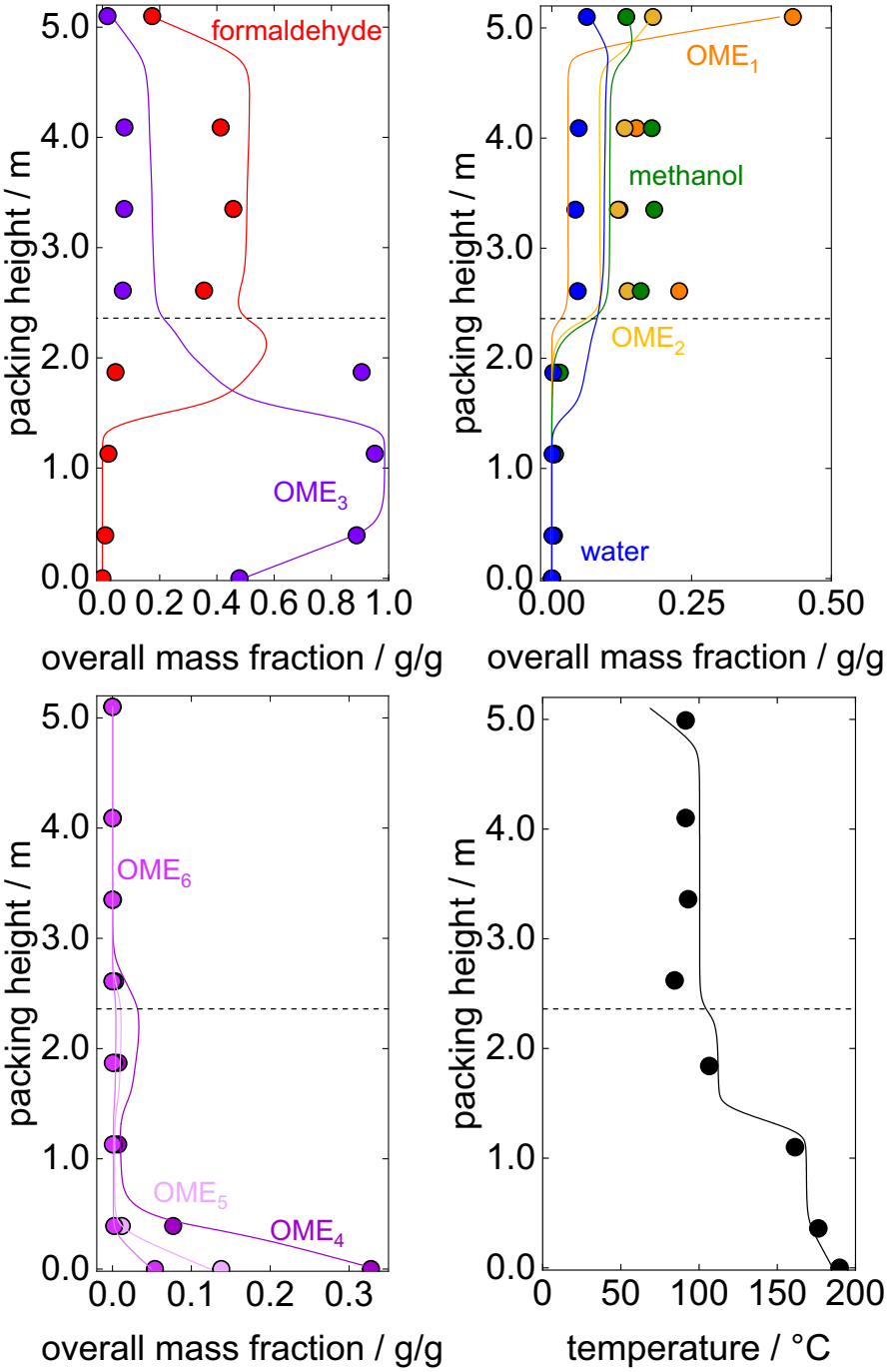

Figure 47: Distillation profiles of overall mass fractions in the liquid phase and temperature corresponding to Run 8. Filled circles: Experimental results. Solid lines: Simulation using equilibrium stage model, where the mass fraction of OME_3 at 0.43 m and reflux ratio were specified. Dashed line: Feed position. Crosses: Predicted freezing temperatures. Dotted line: Predicted freezing temperatures (interpolation).

Run 9

Table 58: Profile of experimental temperatures in the liquid phase of Run 9.

packing height / m	temperature / °C
0	180.46
0.36	171.68
1.10	145.26
1.84	109.46
2.62	86.68
3.36	94.53
4.10	93.29
4.99	90.31

Table 59: Profile of experimental overall mass fractions in the liquid phase of Run 9.

packing height / m	overall mass fractions / g/g								
	FA	ME	WA	OME_1	OME_2	OME_3	OME_4	OME_5	OME_6
0	0.000	0.000	0.000	0.000	0.000	0.515	0.299	0.131	0.055
0.39	0.000	0.000	0.000	0.000	0.000	0.784	0.152	0.049	0.015
1.13	0.040	0.003	0.001	0.003	0.000	0.934	0.013	0.005	0.000
1.87	0.516	0.164	0.005	0.000	0.017	0.270	0.021	0.007	0.000
2.61	0.515	0.140	0.005	0.003	0.037	0.273	0.022	0.005	0.000
3.35	0.461	0.197	0.042	0.050	0.147	0.100	0.004	0.000	0.000
4.09	0.420	0.204	0.052	0.060	0.184	0.078	0.000	0.003	0.000
5.10	0.161	0.135	0.061	0.394	0.242	0.006	0.000	0.000	0.000

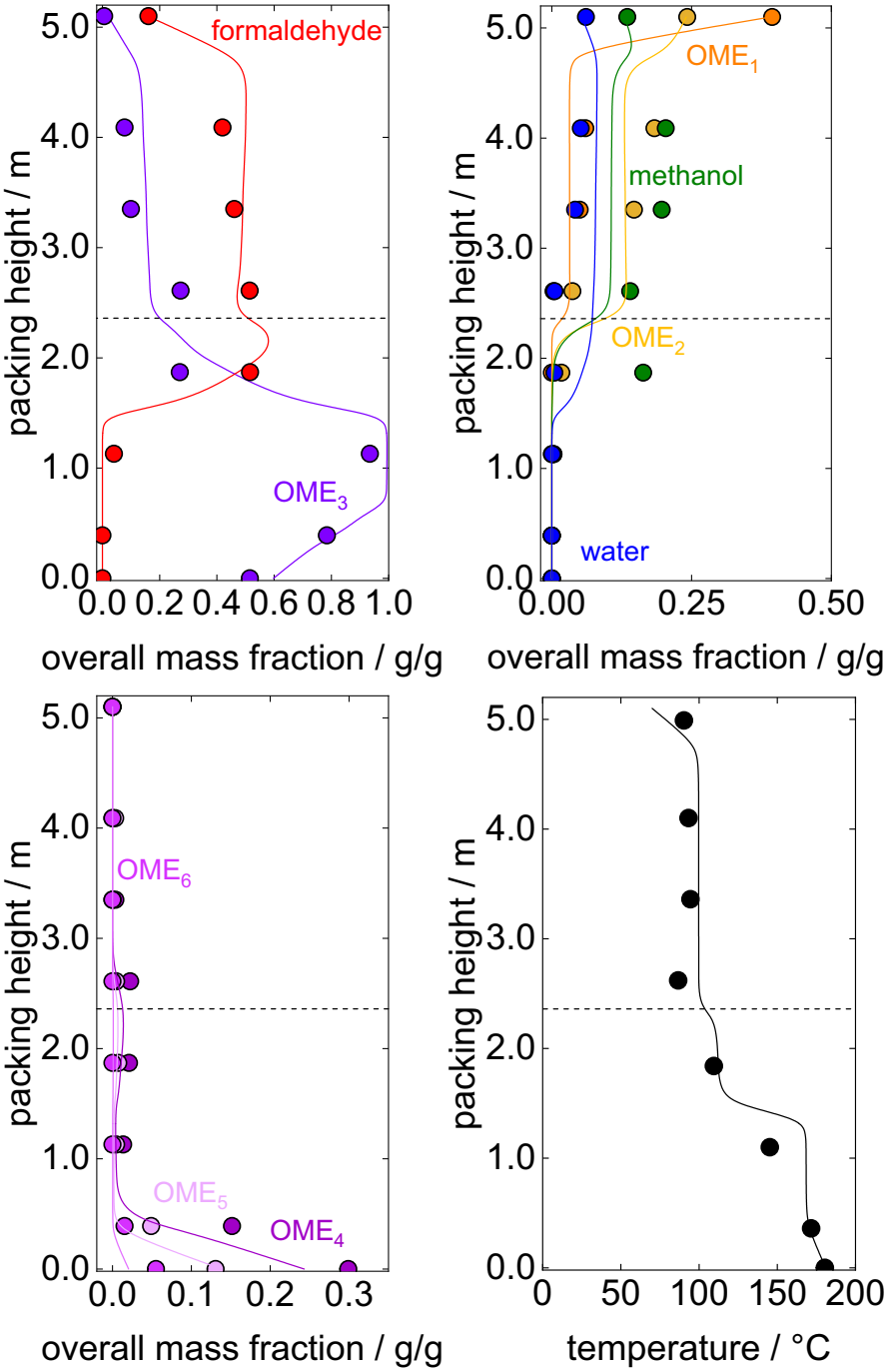

Figure 48: Distillation profiles of overall mass fractions in the liquid phase and temperature corresponding to Run 9. Filled circles: Experimental results. Solid lines: Simulation using equilibrium stage model, where the mass fraction of OME_3 at 0.43 m and reflux ratio were specified. Dashed line: Feed position. Crosses: Predicted freezing temperatures. Dotted line: Predicted freezing temperatures (interpolation).

Run 10

Table 60: Profile of experimental temperatures in the liquid phase of Run 10.

packing height / m	temperature / °C
0	178.30
0.36	167.02
1.10	111.55
1.84	95.06
2.62	84.64
3.36	98.10
4.10	95.56
4.99	88.22

Table 61: Profile of experimental overall mass fractions in the liquid phase of Run 10.

packing height / m	overall mass fractions / g/g								
	FA	ME	WA	OME_1	OME_2	OME_3	OME_4	OME_5	OME_6
0	0.010	0.006	0.002	0.009	0.005	0.467	0.300	0.142	0.058
0.39	0.077	0.025	0.003	0.009	0.005	0.727	0.128	0.022	0.004
1.13	0.492	0.225	0.009	0.001	0.003	0.207	0.041	0.015	0.005
1.87	0.557	0.273	0.008	0.000	0.003	0.111	0.030	0.012	0.005
2.61	n.m	n.m	n.m	n.m	n.m	n.m	n.m	n.m	n.m
3.35	0.519	0.275	0.035	0.060	0.075	0.026	0.000	0.001	0.000
4.09	0.509	0.297	0.043	0.052	0.077	0.011	0.000	0.000	0.000
5.10	0.164	0.179	0.056	0.420	0.155	0.009	0.000	0.001	0.000

C.3 Stream Tables for Runs 2 to 5

Tables 62, 63, 64, and 65 present the overall mass fractions and mass flow rates of Streams 1 to 7 for Runs 2, 3, 4, and 5, respectively.

Table 62: Stream table of Run 2.

		stream number						
		1	2	3	4	5	6	7
overall mass fractions /g/g	FA	0.521	0.210	0.153	0.000	0.172	0.178	0.116
	ME	0.423	0.187	0.133	0.004	0.153	0.151	0.132
	WA	0.053	0.028	0.042	0.000	0.047	0.036	0.515
	OME_1	0.000	0.356	0.389	0.000	0.395	0.397	0.088
	OME_2	0.000	0.188	0.176	0.001	0.206	0.213	0.138
	OME_3	0.000	0.025	0.070	0.461	0.024	0.025	0.010
	OME_4	0.000	0.003	0.025	0.320	0.000	0.000	0.001
	OME_5	0.000	0.001	0.009	0.152	0.005	0.000	0.001
	OME_6	0.000	0.001	0.003	0.065	0.000	0.000	0.000
Mass flow rate / kg/h		0.75	6.78	6.78	0.59	5.90	5.44	0.38

Table 63: Stream table of Run 3.

		stream number						
		1	2	3	4	5	6	7
overall mass fractions /g/g	FA	0.521	0.219	0.177	0.025	0.197	0.197	0.125
	ME	0.423	0.198	0.139	0.003	0.157	0.158	0.105
	WA	0.053	0.035	0.047	0.006	0.053	0.025	0.476
	OME_1	0.000	0.342	0.387	0.001	0.383	0.401	0.199
	OME_2	0.000	0.183	0.173	0.004	0.200	0.209	0.090
	OME_3	0.000	0.022	0.056	0.576	0.008	0.009	0.004
	OME_4	0.000	0.001	0.015	0.234	0.000	0.000	0.000
	OME_5	0.000	0.000	0.004	0.102	0.000	0.000	0.000
	OME_6	0.000	0.000	0.001	0.051	0.000	0.000	0.000
Mass flow rate / kg/h		0.75	6.78	6.78	0.59	5.90	5.44	0.38

Table 64: Stream table of Run 4.

		stream number						
		1	2	3	4	5	6	7
overall mass fractions /g/g	FA	0.521	0.230	0.172	0.001	0.194	0.194	0.116
	ME	0.423	0.198	0.143	0.000	0.167	0.168	0.116
	WA	0.053	0.029	0.044	0.001	0.049	0.025	0.480
	OME_1	0.000	0.347	0.350	0.000	0.371	0.386	0.188
	OME_2	0.000	0.182	0.177	0.000	0.203	0.209	0.095
	OME_3	0.000	0.011	0.072	0.556	0.014	0.017	0.006
	OME_4	0.000	0.001	0.028	0.287	0.000	0.000	0.000
	OME_5	0.000	0.002	0.001	0.120	0.002	0.000	0.000
	OME_6	0.000	0.000	0.003	0.044	0.000	0.000	0.000
Mass flow rate / kg/h		0.75	6.78	6.78	0.59	5.90	5.44	0.38

Table 65: Stream table of Run 5.

		stream number						
		1	2	3	4	5	6	7
overall mass fractions /g/g	FA	0.521	0.226	0.169	0.001	0.191	0.192	0.111
	ME	0.423	0.204	0.139	0.000	0.153	0.156	0.104
	WA	0.053	0.027	0.045	0.000	0.048	0.024	0.488
	OME_1	0.000	0.342	0.353	0.002	0.392	0.400	0.196
	OME_2	0.000	0.185	0.178	0.001	0.203	0.213	0.095
	OME_3	0.000	0.015	0.073	0.565	0.013	0.014	0.006
	OME_4	0.000	0.000	0.028	0.280	0.000	0.000	0.000
	OME_5	0.000	0.000	0.010	0.115	0.001	0.000	0.000
	OME_6	0.000	0.000	0.004	0.046	0.000	0.000	0.000
Mass flow rate / kg/h		0.76	6.86	6.86	0.68	6.09	5.56	0.32

C.4 Water Separation via Adsorption: Simulated Stream Tables

Tables 66, 67, and 68 present the mass balances for the simulated operating points 1, 2, and 4 employing adsorption for water separation , cf. Section 4.4.5.

Table 66: Stream table of the operating point 1 in the water-tolerant OME_{3-5} process by Schmitz et al. [24] including an adsorptive step. Time-on-stream of the adsorption column = 97 min.

		stream number						
		1	2	3	4	5	6	7
overall mass fractions /g/g	FA	0.560	0.137	0.089	0.000	0.096	0.078	0.385
	ME	0.340	0.120	0.090	0.000	0.097	0.090	0.221
	WA	0.100	0.012	0.021	0.000	0.022	$4.7 \cdot 10^{-5}$	0.394
	OME_1	0.000	0.524	0.525	0.000	0.564	0.598	0.000
	OME_2	0.000	0.187	0.187	0.000	0.201	0.213	0.000
	$OME_{\geq 3}$	0.000	0.018	0.088	1.000	0.020	0.021	0.000
Mass flow rate / kg/h		0.132	1.075	1.075	0.075	1.000	0.943	0.057

Table 67: Stream table of the operating point 2 in the water-tolerant OME_{3-5} process by Schmitz et al. [24] including an adsorptive step. Time-on-stream of the adsorption column = 147 min.

		stream number						
		1	2	3	4	5	6	7
overall mass fractions /g/g	FA	0.560	0.158	0.103	0.000	0.112	0.112	0.117
	ME	0.340	0.131	0.098	0.000	0.106	0.108	0.055
	WA	0.100	0.015	0.025	0.000	0.027	0.006	0.828
	OME_1	0.000	0.489	0.489	0.000	0.530	0.544	0.000
	OME_2	0.000	0.187	0.187	0.000	0.203	0.208	0.000
	$OME_{\geq 3}$	0.000	0.020	0.098	1.000	0.021	0.022	0.000
Mass flow rate / kg/h		0.110	1.085	1.085	0.085	1.000	0.974	0.026

Table 68: Stream table of the operating point 4 in the water-tolerant OME_{3-5} process by Schmitz et al. [24] including an adsorptive step. Time-on-stream of the adsorption column = 247 min.

		stream number						
		1	2	3	4	5	6	7
overall mass fractions /g/g	FA	0.560	0.213	0.173	0.000	0.183	0.186	0.047
	ME	0.340	0.179	0.154	0.000	0.164	0.166	0.014
	WA	0.100	0.073	0.080	0.000	0.085	0.071	0.940
	OME_1	0.000	0.377	0.377	0.000	0.400	0.407	0.000
	OME_2	0.000	0.143	0.143	0.000	0.152	0.154	0.000
	$OME_{\geq 3}$	0.000	0.015	0.074	1.000	0.016	0.016	0.000
Mass flow rate / kg/h		0.079	1.062	1.062	0.062	1.000	0.983	0.016

Student theses

The following student theses were prepared under the supervision of the author of the present doctoral thesis in the frame of his research:

- U. Stegemeyer: Kontinuierlicher Betrieb einer Destillationskolonne zur Herstellung von Poly(oxymethylen)dimethylethern aus Methanol und wässrigem Formaldehyd. Bachelor thesis, Laboratory of Chemical Process Engineering (CTV), Technical University of Munich (2021).
- C. Mertins: Betrieb einer kontinuierlichen Demonstrationsanlage zur Herstellung von Poly(oxymethylen)dimethylethern aus Methanol und wässrigem Formaldehyd. Bachelor thesis, Laboratory of Chemical Process Engineering (CTV), Technical University of Munich (2022).
- N. Zistler: Modellierung einer kontinuierlichen Adsorptionskolonne zur Wasserabtrennung in der OME Herstellung. Bachelor thesis, Laboratory of Chemical Process Engineering (CTV), Technical University of Munich (2022).